Multiphase Deformation Analysis of Elasto-viscoplastic Unsaturated Soil and Modeling of Bentonite

December 2007

Huaiping Feng

Abstract

The deformation behavior of unsaturated soil has been the subject of numerous experimental and theoretical investigations. However, this phenomenon is not fully understood. Problems, such as the adoption of the proper stress variables, reduction of suction inducing collapse, suction effect on soil stiffness, rate dependency and air trapped within the soil under rainfall infiltration still need additional studies. In the present studies, an elasto-viscoplastic model for unsaturated soil is used based on two stress variables: 1) the skeleton stress is adopted as the stress variable; 2) suction is incorporated into the constitutive model to describe the collapse behavior. In addition, to investigate the multiphase behavior of unsaturated soil, a three-phase coupled model has been proposed based on the Theory of Porous Media (TPM) and finite deformation theory. Van Genuchten type of equation is employed as a constitutive equation between the saturation and the suction.

Three-dimensional multiphase simulations are carried out to reproduce the behavior of unsaturated soil during monotonic loading triaxial tests under drained and undrained conditions for water and air. Compared with experimental results and the simulated results, it is seen that the proposed formulation is very suitable to describe the mechanical behaviors of unsaturated soil.

Cyclic behavior of unsaturated soil has attracted much attention during the past few years. An elasto-viscoplastic cyclic model for saturated soil is extended for modeling of unsaturated soil. Based on finite deformation theory, three-dimensional multiphase analyses for unsaturated soil under cyclic loading are presented. The simulations are verified with cyclic triaxial tests on unsaturated silty clay under undrained for water and air conditions. It shows that the proposed multiphase formulation can be used to simulate the behaviors of unsaturated soil under cyclic loading.

The high expansiveness of bentonite is another significant problem in unsaturated soil mechanics. In this research, an elasto-viscoplastic model for unsaturated expansive soil has been developed. An evolutional equation is adopted for describing the absorption of water into interlayer of clay platelets. In addition, the internal compaction effect caused by swelling of clay unit is expressed with the expansion of overconsolidation boundary surface and static yield surface. Based on the model, one-dimensional finite element analysis is conducted to study the development of swelling pressure. Compared with experimental results and simulated results, it is found that the proposed model can reproduce the effects of dry density and initial water content on swelling behavior. Using the proposed swelling model, two-dimensional swelling behaviors of the waste barrier are simulated.

Acknowledgement

The research for this dissertation was carried out over a period of three years at the Laboratory of Geomechanics, Department of Civil and Earth Resources Engineering, Graduate School of Engineering, Kyoto University, Japan. I wish to express my profound gratitude to the members of the Dissertation Committee, namely, Professor Fusao Oka, Professor Toshifumi Matsuoka, and Associate Professor Sayuri Kimoto, for their discussions, invaluable comments, and constructive suggestions in reviewing this work.

First and foremost, I would like to express my sincere apprecition to my supervisor Professor Fusao Oka, for his invaluable help and encouragement in all aspects of this research work. Without his earnest inspiration, continuous support, distinct guidance and supervision, this research would not have been possible. The numerous comments, critisisms, and suggestions he made, based on his deep insight and vast experience in the field of geotechnical engineering, are gratefully acknowledged. He must have been very patient during the time-consuming process of checking and correcting my thesis. His care and thoughfulness has extended even to my family during the time they are in Japan. Studying under Professor Oka's supervision as a postgraduated student has been a privilege in my development as an engineer as well as a person.

I also wish to express my sincere gratitude to the Associate professor Sayuri Kimoto. Many hours of fruitful discussion on constitutive modeling and the soil mechanics with her deserve special recognition. I wish to express my heartfelt thanks to Ms Kimoto for her continuous and ever-present supports and encouragements.

I would like to extend my thanks to Dr. Yosuke Higo, Assistant Professor in Laboratory of Geomechanics at the Graduated School of Engineering, for his valuble suggestions and constructive discussions on the numerical analysis.

I also like to express my thanks to Dr. Satoshi Imamura and Dr. Kenichi Horikoshi of Taisei Corporation for their discussions and constructive suggestions.

I would next like to express my thanks to Ms Chikako Itou, Secretary of Oka Laboratory, for the generosity she exhibited whenever I sought for any assistance. I would like to thank all of graduated colleagues in Oka Laboratory including Dr. Young-Seok Kim, Dr. Boonlert Siribumrungwong, Dr. Md Rezul Karim, Dr. Asiri Karunawardena, for helping in my work and personal life in numerious ways. I would also like to thank all of the friends who are current members of the Oka Laboratory, who help me in one way or another, including doctoral course students Nguyen Quoc Huy, Hiroki Uno, Edwin Garcia, Mojtaba Mirjalili, Ryosuke Kato and master course students, Tinet Anne-Julie Marie, Mai Sawada, Shinya Yamazaki, Tomohiko Fushita, Hirofumi Ohta, Junya Fukutani, Ana Paula Heitor, and Taichi Yabuki, Taisuke Sanagawa, Yuichi Morinaka, who all deserve to be mentioned.

I would like to sincerely appreciate my master course supervisor, Dr. Zurun Yue, Professor, at Shijiazhuan Railway Institute, China, for his constant consideration and support in various ways. Also, I am grateful to colleagues in Shijiazhuan Railway Institute, China, for their assistances.

I would like to express my thanks to Japanese Ministry of Education, Culture, Sports, Science and Technology for three and half years financial support through “Monbusho Scholarship”.

I would like to express heartfelt thanks to my friends in Kyoto University: Fulin Wang, Jun Yao, Ming Zhao, Wei Xu, Weixin Huang, Zhouen Zhang, Zhiqiang Bian, Fenfen Zhu, Yang Zhang, etc. for their friendship and assistances.

My deepest gratitude goes to my parents, for their continuous support and sacrifices on my behalf. Finally, with sincere love, I wish to thank my wife Jianmei Chang for her endless patience, concern and encouragement. Nevertheless, I want to express my appreciation for my wonderful son Yuyang Feng who always keep me smiling.

Table of Contents

1 INTRODUCTION 1

1.1 Background and Objectives 1
1.2 Scope and Organization 4

2 ELASTO-VISCOPLASTIC MODEL FOR UNSATURATED SOIL AND A MULTIPHASE FINITE ELEMENT FORMULATION 5

2.1 Introduction 5
2.2 Elasto-Viscoplastic Constitutive Model Considering Suction Effect for Unsaturated Soil 7
  2.2.1 General Setting 8
  2.2.2 Partial Stress and the Skeleton Stress 9
  2.2.3 Elastic Strain Rate 10
  2.2.4 Overconsolidation Boundary Surface 10
  2.2.5 Static Yield Function 11
  2.2.6 Viscoplastic Potential Function 12
  2.2.7 Viscoplastic Flow Rule 14
2.3 Multiphase Finite Element Formulation for the Analysis of Unsaturated Soil 15
  2.3.1 Hydraulic Property of Unsaturated Soil 15
  2.3.2 Conservation of Momentum 17
  2.3.3 Tangent Stiffness Method 24
  2.3.4 Conservation of Mass 26
  2.3.5 Discretized Governing Equations for the Multiphase Finite Element Analysis 35

3 THREE-DIMENSIONAL MULTIPHASE SIMULATION OF THE TRIAXIAL BEHAVIOR OF UNSATURATED SOIL 37

3.1 Introduction....37
3.2 Triaxial Compression Tests on Unsaturated Soil....38
  3.2.1 Material Properties....38
  3.2.2 Equipment and Testing Program....38
3.3 Numerical Simulations....40
  3.3.1 Geometry and Boundary conditions....40
  3.3.2 Determination of the Material Parameters....41
3.4 Simulation Results....44
  3.4.1 Simulation of the Drained Tests....44
  3.4.2 Simulation of the Undrained Tests....50
3.5 Summary....58

4 SIMULATION OF THE CYCLIC UNDRAINED BEHAVIOR OF UNSATURATED SOIL USING A CYCLIC ELASTO-VISCOPLASTIC MODEL....61

4.1 Introduction....61
4.2 Cyclic Elasto-Viscoplastic Constitutive Model for Unsaturated Soil....62
  4.2.1 Assumptions....62
  4.2.2 Static Yield Function....63
  4.2.3 Viscoplastic Potential Function....63
  4.2.4 Hardening Rule....64
  4.2.6 Viscoplastic Flow Rule....65
4.3 Numerical Analyses....65
  4.3.1 Simulated Results at P^C=0 kPa....67
  4.3.2 Simulated Results at P^C=50 kPa....72
  4.3.3 Effects of Suction on the Cyclic Behavior....80
4.4 Summary....80

5 ELASTO-VISCOPLASTIC CONSTITUTIVE MODEL FOR SWELLING UNSATURATED BENTONITE....81

5.1 Introduction....81
5.2 Elasto-viscoplastic Constitutive Model for Unsaturated Swelling Soil....83
  5.2.1 Model Assumptions....84
  5.2.2 Swelling Equation for Interparticles....84

5.2.3 Hardening Rule Including Swelling Effect......................................85
5.3 Simulation of Swelling Pressure Tests...87
5.3.1 Swelling Pressure with Wetting Process..88
5.3.2 Application to Kunigel GX Bentonite 95
5.4 Summary...97

6 NUMERICAL SIMULATION OF SWELLING PRESSURE OF DISPOSAL BARRIERS...99

6.1 Introduction...99
6.2 Numerical Simulations 100
6.2.1 Swelling Behavior of Bentonite..100
6.2.2 A Waste Barrier Example..103
6.2.3 Swelling of Bentonite Layer with Fine Element Size.....................108
6.2.4 Application to a Large Scale Problem 112
6.3 Summary...117

7 CONCLUSIONS AND FUTURE WORK...119

7.1 Summary and Conclusions...119
7.2 Recommendation for Future work..121

REFERENCES 123

List of Figures

Figure 2.1 The strength degradation due to the reduction of suction
Figure 2.2 Shrinkage of the OC boundary surface, static yield function, and potential function in the NC region
Figure 2.3 Shrinkage of the OC boundary surface, static yield function, and potential function in the OC region
Figure 2.4 Boundary conditions for the whole fluid-solid mixture
Figure 2.5 Boundary conditions for the liquid phase
Figure 2.6 Boundary conditions for the gas phase

Figure 3.1 Schematic drawing of the triaxial cell used to test the unsaturated soil
Figure 3.2 Isoparametric elements used in the three-dimensional finite element method
Figure 3.3 Finite element mesh and boundary conditions
Figure 3.4 The soil water characteristic curve
Figure 3.5 Stress paths with different levels of initial suction: (a) simulated results and (b) experimental results
Figure 3.6 Deviator stress-axial strain relations: (a) simulated results and (b) experimental results
Figure 3.7 Volumetric strain-axial strain relations: (a) simulated results and (b) experimental results
Figure 3.8 Pore water pressure vs. axial strain
Figure 3.9 Distribution of pore water pressure (P^C =50 kPa)
Figure 3.10 Suction vs. axial strain
Figure 3.11 Degree of saturation vs. axial strain
Figure 3.12 Distribution of the mean skeleton stress (kPa) (P^C =50 kPa, Drained)
Figure 3.13 Distribution of suction (kPa) (P^C =50 kPa, Drained)
Figure 3.14 Deviator stress-strain relations under different level of strain rates: (a) simulated results and (b) experimental results
Figure 3.15 Deviator stress-strain relations under different level of confining pressures: (a) simulated results and (b) experimental results

Figure 3.16 Stress paths with different levels of initial suction: (a) simulated results and (b) experimental results
Figure 3.17 Deviator stress-axial strain relations with different levels of initial suction: (a) simulated results and (b) experimental results
Figure 3.18 Volumetric strain-axial strain relations with different levels of initial suction: (a) simulated results and (b) experimental results
Figure 3.19 Suction vs. axial strain with different levels of initial suction: (a) simulated results and (b) experimental results
Figure 3.20 Pore water pressure vs. axial strain with different levels of initial suction: (a) simulated results and (b) experimental results
Figure 3.21 Pore air pressure vs. axial strain with different levels of initial suction.
Figure 3.22 Stress paths for different levels of confining pressure (P^c = 50 kPa): (a) simulated results and (b) experimental results
Figure 3.23 Distribution of $\sqrt{S_{ij}S_{ij}}$ and the mean skeleton stress $\sigma_m^{'}$ under P^C=50 and 0 kPa
Figure 3.24 Simulations for different strain rates (P^C=50 kPa)
Figure 3.25 Simulations for different strain rates (P^C=50 kPa)
Figure 3.26 Stress paths for different levels of confining pressure (P^c = 50 kPa): (a) simulated results and (b) experimental results
Figure 3.27 Simulations for different levels of confining pressure (P^c = 50 kPa): (a) simulated results and (b) experimental results
Figure 3.28 Volumetric strain-axial strain relations: (a) simulated results and (b) experimental results

Figure 4.1 Deviator stress-axial strain relations: (a) simulated results and (b) experimental results
Figure 4.2 Stress paths: (a) simulated results and (b) experimental results
Figure 4.3 Pore water pressure vs. time: (a) simulated results and (b) experimental results
Figure 4.4 Volumetric strain vs. axial strain: (a) simulated results and (b) experimental results
Figure 4.5 Deviator stress-axial strain relations: (a) simulated results and (b) experimental results
Figure 4.6 Stress path: (a) simulated results and (b) experimental results
Figure 4.7 Volumetric strain-axial strain relations: (a) simulated results and (b) experimental results

Figure 4.8 Pore water pressure vs. time: (a) simulated results and (b) experimental results
Figure 4.9 Deviator stress-axial strain relations: (a) simulated results and (b) experimental results
Figure 4.10 Stress path: (a) simulated results and (b) experimental results
Figure 4.11 Pore water pressure vs. time: (a) simulated results and (b) experimental results
Figure 4.12 Volumetric strain-axial strain relations: (a) simulated results and (b) experimental results
Figure 4.13 Deviator stress-axial strain relations: (a) simulated results and (b) experimental results
Figure 4.14 Stress path: (a) simulated results and (b) experimental results
Figure 4.15 Pore water pressure vs. time: (a) simulated results and (b) experimental results
Figure 4.16 Suction vs. time: (a) simulated results and (b) experimental results
Figure 4.17 Degree of saturation vs. time: (a) simulated results and (b) experimental results
Figure 4.18 Volumetric strain-axial strain relations: (a) simulated results and (b) experimental results
Figure 4.19 Deviator stress-axial strain relations: (a) simulated results and (b) experimental results
Figure 4.20 Stress path: (a) simulated results and (b) experimental results
Figure 4.21 Pore water pressure vs. time: (a) simulated results and (b) experimental results
Figure 4.22 Suction vs. time: (a) simulated results and (b) experimental results
Figure 4.23 Degree of saturation vs. time: (a) simulated results and (b) experimental results
Figure 4.24 Volumetric strain-axial strain relations: (a) simulated results and (b) experimental results
Figure 4.25 Deviator stress-axial strain relations: (a) simulated results and (b) experimental results
Figure 4.26 Stress path: (a) simulated results and (b) experimental results
Figure 4.27 Pore water pressure vs. time: (a) simulated results and (b) experimental results
Figure 4.28 Suction vs. time: (a) simulated results and (b) experimental results

Figure 4.29 Degree of saturation vs. time: (a) simulated results and (b) experimental results
Figure 4.30 Volumetric vs. time: (a) simulated results and (b) experimental results

Figure 5.1 Swelling structure of montmorillonite
Figure 5.2 Swelling equations with different parameters for *A* and *B*
Figure 5.3 SEM image of wetting process of bentonite (Komine and Ogata 2004)
Figure 5.4 Process of swelling with deformation restricted
Figure 5.5 Isoparametric elements for the soil skeleton and the pore pressure
Figure 5.6 Finite element mesh and boundary conditions
Figure 5.7 Degree of saturation for each element with wetting
Figure 5.8 Suction for each element with wetting
Figure 5.9 Effect of permeability on the swelling pressure
Figure 5.10 Effect of the onset saturation for the swelling on swelling pressure
Figure 5.11 Effect of the parameter γ on the swelling pressure
Figure 5.12 Changes in hardening parameter σ'_{mb} with different γ values
Figure 5.13 Effect of parameter A on the swelling pressure
Figure 5.14 Comparison of compacted bentonite with different initial water contents
Figure 5.15 Experimental results (Ono et al., 2006)
Figure 5.16 Simulated results for swelling pressure

Figure 6.1 Finite element mesh and boundary conditions
Figure 6.2 Distribution of mean skeleton stress with wetting (kPa)
Figure 6.3 Distribution of pore water pressure with wetting (kPa)
Figure 6.4 Finite element mesh and boundary conditions
Figure 6.6 Distribution of the suction with wetting (kPa)
Figure 6.7 Distribution of mean skeleton stress with wetting (kPa)
Figure 6.8 Displacements vector at 29.8 days
Figure 6.9 Displacement along the buffer layer (m)
Figure 6.10 Finite mesh and boundary conditions
Figure 6.11 Distribution of the degree of saturation (%)
Figure 6.12 Distribution of the mean skeleton stress (kPa)
Figure 6.13 Accumulated displacement vector (m)
Figure 6.14 Distribution of degree of saturation (%)
Figure 6.15 Distribution of the mean skeleton stress (kPa)
Figure 6.16 Time increment employed in analysis

Figure 6.17 Finite element mesh and the boundary conditions for the problem (Horikoshi et al. 2007)
Figure 6.18 Distribution of pore water pressure with wetting (kPa)
Figure 6.19 Distribution of the mean skeleton stress (kPa)
Figure 6.20 Distribution of mean skeleton stress at corner (kPa)
Figure 6.21 Distribution of the second invariant of deviatoric stress tensor (kPa)
Figure 6.22 Accumulated displacement vector (around the buffer)

List of Tables

Table 3.1 Material parameters and initial conditions
Table 3.2 Simulated cases

Table 4.1 Simulated cases
Table 4.2 Material parameters

Table 5.1 Initial conditions of the simulations
Table 5.2 Material parameters
Table 5.3 Properties of the Kunigel GX
Table 5.4 Experimental cases (Ono, 2006)
Table 5.5 Parameters for the simulation

Table 6.1 Material parameters and initial conditions for bentonite
Table 6.2 The parameters for rock and container
Table 6.3 Parameters for the elastic materials
Table 6.4 The material parameters for elastic materials

Chapter 1

INTRODUCTION

1.1 Background and Objectives

About 33% of the earth's surface is thought to consist of arid and semi-arid areas (Dregne, 1976). More than two phases are commonly present in most natural deposits as well as in most man-made soil structures in these areas. Soils that are unsaturated forms the largest category of materials which do not adhere behaviorally to classical saturated soil mechanics (Fredlund and Rahardjo 1993). Recently, the number of researchers actively involved in a variety of studies related to unsaturated soils has vastly increased. Along with these studies has been a significant amount of research which deals with constitutive models and numerical formulations for flow-deformation coupled models.

In order to carry out a theoretical analysis on the unsaturated soil, it is necessary to choose appropriate stress variables for the unsaturated soil. It is recognized that Bishop's effective stress (1960) can not be applied to explain issues related to collapsible soil, such as saturation-induced collapse. Thus, many researchers (Fredlund & Morgenstern, 1977; Alonso et al. 1990) have chosen net stress $\sigma - P^G$ and suction $P^G - P^W$ as the stress state variables. The skeleton stress, which has the same form as Bishop's effective stress, has recently been used in place of the effective stress from the viewpoint of mixture theory (Bolzon et al. 1996; Jommi, 2000; Ehlers 2004). However, the adoption of skeleton stress, which is called as "average skeleton stress" by Jommi (2000), is questioned by several researchers. Jennings and Burland (1962), for example, showed that the mechanical behavior of unsaturated soil can not be related to a single effective stress. In present model, the mechanical behavior of unsaturated soil is reproduced by making two basic assumptions, namely, 1) that the skeleton stress is adopted as a stress variable and 2) that suction is incorporated into the elasto-viscoplastic model to describe the collapse behavior.

While many constitutive models have been proposed (e.g., Alonso et al. 1990; Wheeler and Sivakumar, 1995; Wheeler & Karube, 1996; Cui and Dleage, 1996; Thomas and He, 1998; Sheng et al. 2003), most of them fall within the framework of a rate-independent models such as elasto-plastic models. However, it is important to consider the time-dependent property of the unsaturated soil in many civil projects, e.g. to analyze the effect of the increase rate of river water level on the mechanical behavior of embankments which include clay materials. In present analysis, an elasto-visctoplastic model for unsaturated soil is proposed; it is an extension of the elasto-viscoplastic model for saturated soil (Kimoto and Oka 2005).

In recent years, several researchers have dealt with numerical formulations for unsaturated soil. Most of these formulations (Sheng, Sloan, Gens and Smith 2003; Wong, Fredlund, and Krahn 1998) are coupled water flow-deformation models in which the pore air pressure is assumed to be constant. As is well known, unsaturated soil is commonly defined as having three phases, namely, solids, water, and 3) air. It is also known that air can become trapped in some parts of embankments due to heavy rains or overflow (Yamamura 1971). It is necessary, therefore, to construct a multiphase analysis, which can describe the flow of the gas phase. Multiphase formulations for unsaturated soil have been reported by several researchers based on the theory of mixture (Schrefler 1996; Loret and Khalili 2000; Ehlers 2003). For example, Ehlers and Graf (2003) and Ehlers et al. (2004) provided the momentum equation for both the gas phase and the fluid phase, and then carried out a multiphase simulation. The SWCC (Soil Water Characteristic Curve) and the saturation-dependent permeability are considered in their analysis. However, the stress variables have not been well discussed. In the present research, a fully-coupled multiphase formulation for unsaturated soil is proposed, from the viewpoint of Theory of Porous Media (TPM), by adopting the skeleton stress which is the same as the average skeleton stress by Jommi (2000), and suction into constitutive model. Using the these equations, a series of three-dimensional simulations are conducted under undrained conditions for air and water, as well as under drained conditions for air and water. Undrained conditions for water and air can be called "constant water content and constant air content conditions"; drained conditions for water and air can be call "constant air and water pressure conditions". The simulation results are verified with the experimental results.

It is well known that the cyclic loading of unsaturated soils is a common phenomenon in geotechnical and geo-environmental engineering. A typical example is the landslides which are brought about by earthquakes. Researchers have recently been focusing on the behavior of foundations, composed of different materials, during earthquakes. This behavior includes the interaction between the sand layer and the clay layer, the total settlement of the two layers, and the effect of the clay layer on liquefaction. Despite the extensive researches for unsaturated clay, theoretical and experimental investigations on the cyclic behavior of unsaturated clay have been limited (Muraleetharan and Nedunri 1998 and Muraleetharan and Wei 2000). In present study, the cyclic elasto-viscoplastic model for saturated soil (Oka et al. 1992) is extended to model the cyclic behavior of unsaturated soil. Based on the multiphase formulations, a three-dimensional finite element analysis is carried out to investigate the cyclic behavior of unsaturated soil under undrained conditions for water and air.

Highly expansive soil such as bentonite, is currently considered to be a suitable barrier material for the isolation of waste, e.g., nuclear, industrial, mining wastes, from the surrounding environment due to its low permeability and self-rehabilitation owing to the swelling. Expansive clay is generally compacted and consequently, it is initially in an unsaturated state. Expansive soil undergoes huge volumetric changes when exposed to water. Under confined conditions, expansive soil will exhibit considerable swelling pressures, which may results in serious damage to buildings and other structures. Therefore, it is necessary to have an advanced understanding of the mechanical behavior of this type of material. Several numerical models have been proposed to simulate expansive soil (Alonso et al. 1991, 1999, and 2000) based on the elastoplastic theory. In the present study, a constitutive model for highly expansive soil is developed based on the elasto-viscoplastic model for unsaturated soil. Using this model, the behavior of a two-dimensional waste barrier with wetting is investigated.

As mentioned above, the main topic of this dissertation can be roughly divided into three parts. Firstly, a three-dimensional multiphase analysis method with an elasto-viscoplastic model for unsaturated soil will be presented. A series of simulations under various conditions will be carried out.

Secondly, a three-dimensional multiphase cyclic elasto-viscoplastic analysis of is carried out on unsaturated soil.

Finally, an elasto-viscoplastic model for bentonite will be proposed. The model is applied to swelling pressure tests. In addition, the swelling phenomenon of the bentonite buffer in waste barriers is simulated.

1.2 Scope and Organization

The dissertation consists of seven chapters. An outline of each chapter is given below.

In Chapter 2, a numerical model for unsaturated soil, based on the mixture theory and the elasto-viscoplastic constitutive model for unsaturated soil is constructed. The collapse behavior, which occurs with a decrease in suction, is expressed with the shrinkage of the overconsolidation boundary surface, static yield surface, and the viscoplastic potential surface. An air-water-soil coupled finite element method is developed in the present study using the governing equations for multiphase soil based on the finite deformation theory.

In Chapter 3, three-dimensional numerical analyses for unsaturated soil are conducted under undrained and drained conditions, and the applicability of the proposed method is studied. The performance of the model is examined with the triaxial compression test results. In addition, the effect of the initial suction, the strain rate, and the confining pressure are studied.

In Chapter 4, a cyclic elasto-viscoplastic constitutive model for unsaturated soil is introduced. Based on this model, three-dimensional simulations of the behavior of triaxial cyclic unsaturated soil are carried out using the multiphase finite element method. The dynamic behavior of unsaturated soil is investigated with various levels of initial suction and stress amplitude.

In Chapter 5, an elasto-viscoplastic swelling model for unsaturated bentonite is developed based on the elasto-viscoplastic model for unsaturated soil. An internal variable H, that reproduces the rise in the absorption of water into the clay interlayer, is introduced to describe the large volumetric expansive behavior of bentonite particles. The model is applied to swelling pressure tests which show that this model can reflect the effect of the initial water content and the dry density on the swelling pressure.

In Chapter 6, the elasto-viscoplastic swelling model is adopted to simulate two-dimensional waste barrier problem. The wetting process and the development of swelling pressure are reproduced.

In Chapter 7, the conclusions of the dissertation and the recommendations for the future work are given.

Chapter 2

ELASTO-VISCOPLASTIC MODEL FOR UNSATURATED SOIL AND A MULTIPHASE FINITE ELEMENT FORMULATION

2.1 Introduction

It has been recognized that the behavior of unsaturated soil plays an important role in geomechanics. Many geotechnical problems, i.e., natural slopes, artificial structures, expansive soil, soil containing methane hydrates, etc., are related to unsaturated soils. To analyze the unsaturated soil, it is necessary to choose appropriate stress variables for soils. It is known that the behavior of saturated soil can be predicted when a constitutive equation with Terzaghi's effective stress principle and the governing equations for a two-phase mixture are applied. However, Terzaghi's effective stress equation is totally valid for saturated soil only when the soil particles and the pore water are incompressible, and it is approximately valid for soil in which the ratios of the compressibility of the soil particles and water to that of the soil skeleton are very small (Oka 1988; 1996). Considering the fact that unsaturated soil is compressible even under undrained conditions, due to the existing of gas phase, many researchers have been discussing the effective stress for partially saturated soil (e.g., Lade and Boer 1997) from the viewpoint of the traditional effective stress. Bishop (1960), for example, proposed the following effective stress for unsaturated soil:

$$\sigma'_{ij} = \left(\sigma_{ij} - u_a\delta_{ij}\right) + \chi\left(u_a - u_w\right)\delta_{ij} \tag{2.1}$$

where, $\sigma_{ij}^{'}$ is the effective stress tensor or the Bishop stress tensor, σ_{ij} is the total stress tensor, u_a and u_w are the pore air pressure and the pore water pressure, respectively, δ_{ij} is Kronecker's delta, and χ is a constitutive material parameter that ranges between 1.0 for saturated soil and zero for dry soil depending on the degree of saturation. The explanation for this expression is based on the balance of force around the interparticle contact area. The term ($\sigma_{ij} - u_a$) is called net stress, and the product $\chi(u_a - u_w)$ represents the interparticle effective stress due to capillary cohesion.

However, Jennings and Burland (1962) pointed out that the Bishop's effective stress tensor cannot be applied to explain the issues related to collapsible soil, such as the collapse behavior, because suction ($u_a - u_w$) decreases during wetting. To reflect the collapse behavior of unsaturated soil, researchers (Bishop and Donald 1961; Coleman 1962; Burland 1965; Matyas and Radhakrishna 1968; Fredlund and Morgenstern 1977) have suggested isolating the relevant stress variables to study unsaturated soil. According to their studies, any pair of stress fields among the following three stress states, $(\sigma_{ij} - u_a\delta_{ij})$, $(\sigma_{ij} - u_w\delta_{ij})$, and $(u_a - u_w)\delta_{ij}$, can be applied as a suitable stress framework to describe the stress-strain-strength behavior of partially saturated soils. For example, two stress variables, $(\sigma_{ij} - u_a\delta_{ij})$ and suction $(u_a - u_w)\delta_{ij}$, have been adopted to describe the mechanical behavior of unsaturated soil by some researchers (Fredlund and Morgenstern 1977; Alonso et al. 1996; Wheeler and Sivakumar 1995; Gens 1995; Cui and Delage 1996). The adoption of net stress $(\sigma_{ij} - u_a\delta_{ij})$ is valid for unsaturated soil only when the air pressure is thought to be constant or equal to the atmospheric pressure. This is because the net stress is affected by changes in air pressure and is not an independent stress varible. However, drained conditions for water and air cannot always be attained in engineering problems. For example, the air pressure in river embankments increases during the seepage process and may vary during the soil compaction process. Meanwhile, using the net stress and the suction as stress variables, it is very difficult to apply many constitutive models which have been developed for saturated soils, to unsaturated soils (Kohgo et al. 1993).

In recent years, other generalized effective stress equations have also been used to explain the collapse phenomenon (Bolzon et al. 1996; Loret and Khalili 2000; Kohgo et al. 2001). Most of these models are defined by the generalized effective stress concept with the introduction of a new constitutive parameter for the effective stress. The skeleton stress has recently been used instead of the effective stress from a viewpoint of the mixture theory (Bolzon et al. 1996; Houlsby 1997; Jommi 2000; Ehlers 2003; Oka 2006). In the present model, the skeleton stress which is the same as the average skeleton stress by Jommi (2000) and suction are adopted as the basic stress variables. We use "Skeleton stress" instead of "the average skeleton stress" to avoid confusing with mean skeleton stress. Suction is incorporated into the constitutive model to describe the collapse behavior of unsaturated soil.

Many constitutive models have been proposed (e.g., Alonso et al. 1990; Wheeler and Sivakumar, 1995; Wheeler & Karube, 1996; Cui and Dleage, 1996; Thomas and He, 1998; Sheng et al. 2003). Most of the models, however, are within the framework of a rate-independent model, such as elasto-plastic models. A series of experiments on unsaturated silt was conducted by Kim (2004) and Nishimatsu (2003). From their results, the time-dependent property of unsaturated silt has been observed. It is also important to consider the time-dependent property of unsaturated soil in many civil engineering projects. For the above reason, it is necessary to construct an elasto-viscoplastic model for unsaturated soil. By adopting the skeleton stress from the viewpoint of mixture theory, and by introducing the suction effect into an elasto-viscoplastic constitutive model for saturated soil considering structure degradation (Kimoto and Oka 2005), an elasto-viscoplastic model for unsaturated soil has been constructed to analyze the unsaturated soil (Kim et al. 2005).

To reproduce the multiphase behavior of unsaturated soil, a partially saturated porous solid material is described within the well-founded Theory of Porous Media (TPM) (Schrefler 1996; Boer 1998; Ehlers 2004; Ehlers and Graf 2004; Loret and Khalili 2000; Kimoto and Oka 2007). To complete the coupled multiphase finite element formulation, the relationship between the degree of saturation and suction, namely, the soil water characteristic curve, is required (Houlsby 1997). In the present model, a van Genuchten type of equation is employed as a constitutive equation between the saturation and the suction. Based on these relations, an air-water-soil three-phase coupled model has been proposed (Oka et al. 2006; Feng et al. 2006).

2.2 Elasto-Viscoplastic Constitutive Model Considering Suction Effect for Unsaturated Soil

In the present study, an elasto-viscoplastic model based on the overstress-type of viscoplasticity theory with soil structure degradation for saturated soil (Kimoto et al. 2005; Kimoto and Oka 2007) has been extended to unsaturated soil using the skeleton stress and the suction effect in the constitutive model (Kimoto and Oka 2007). The collapse behavior of unsaturated soil is macroscopic evidence of the structural instability of the soil skeleton, and it is totally independent of the stress variables adopted in the constitutive modeling (Oka, 1988; Jommi, 2000). In the model, the collapse behavior is described by the shrinkage of the overconsolidation boundary surface, the static yield surface, and the viscoplastic surface due to the decrease in suction.

2.2.1 General Setting

The material to be modeled is composed of three phases, namely, solid (S), liquid (W), and gas (G), which are continuously distributed throughout space. Each constituent has a mass M^{α} and a volume V^{α}, and $\alpha = \mathrm{S}, \mathrm{W}, \mathrm{G}$. The partial quantities used in the method and their relations to intrinsic quantities are defined here. Total volume V is obtained from the sum of the partial volumes of the constituents, namely,

$$\sum_{\alpha} V^{\alpha} = V, \qquad \sum_{\beta} V^{\beta} = V^{\mathrm{v}} \quad (\alpha = \mathrm{S}, \mathrm{W}, \mathrm{G} \quad \beta = \mathrm{W}, \mathrm{G}) \tag{2.2}$$

where V^{v} is the volume of the void.

Volume fraction n^{α} is defined as the local ratio of the volume element with respect to the total volume, namely,

$$n^{\alpha} = \frac{V^{\alpha}}{V}, \qquad \sum_{\alpha} n^{\alpha} = 1 \quad (\alpha = \mathrm{S}, \mathrm{W}, \mathrm{G}) \tag{2.3}$$

The volume fraction of the void, n, is written as

$$n = \sum_{\beta} n^{\beta} = \frac{V^{\mathrm{v}}}{V} = \frac{V - V^{S}}{V} = 1 - n^{\mathrm{S}} \quad (\beta = \mathrm{W}, \mathrm{G}) \tag{2.4}$$

In addition, water saturation is required in the model,

$$s = \frac{V^{\mathrm{W}}}{V^{\mathrm{v}}} \tag{2.5}$$

Accordingly, the volume fraction can be given by

$$n^{\mathrm{W}} = sn \qquad n^{G} = (1 - s)n \tag{2.6}$$

Finally, the partial mass density ρ^{α} and material (realistic or effective) density ρ_{α} are defined as

$$\rho^{\alpha} = \frac{M^{\alpha}}{V} \text{ and } \rho_{\alpha} = \frac{M^{\alpha}}{V^{\alpha}} \qquad \alpha = \mathrm{S}, \mathrm{W}, \mathrm{G} \tag{2.7}$$

where M^{α} is the mass of each constituent. The density of the mixture can be expressed as

$$\rho = \sum_{\alpha} \rho^{\alpha} = \sum_{\alpha} \rho_{\alpha} n^{\alpha} \tag{2.8}$$

2.2.2 Partial Stress and the Skeleton Stress

In present constitutive model, skeleton stress $\sigma_{ij}^{'}$ is defined and then used as the basic stress variables in the constitutive relation for the skeleton. The skeleton stress tensor is equivalent to the Bishop stress tensor when degree of saturation s is taken as χ. Total stress tensor σ_{ij} is obtained from the sum of the partial stress values, σ_{ij}^{α}, as,

$$\sigma_{ij} = \sum_{\alpha} \sigma_{ij}^{\alpha} \tag{2.9}$$

in which σ_{ij}^{α} represents the stress acting on each phase. It is assumed as the Cauchy stress tensor as,

$$\sigma_{ij}^{\mathrm{S}} = \sigma_{ij}^{'} + n^{\mathrm{S}} P^{F} \delta_{ij} \tag{2.10}$$

$$\sigma_{ij}^{\mathrm{W}} = n^{\mathrm{W}} P^{\mathrm{W}} \delta_{ij} \tag{2.11}$$

$$\sigma_{ij}^{\mathrm{G}} = n^{\mathrm{G}} P^{\mathrm{G}} \delta_{ij} \tag{2.12}$$

where $\sigma_{ij}^{'}$ is the skeleton stress, and P^{W} and P^{G} are the pore water pressure, and the pore air pressure, respectively. The average pore pressure P^{F} surrounding the soil skeleton is obtained by the well-known Dalton's law via

$$P^{F} = sP^{\mathrm{W}} + (1-s)P^{\mathrm{G}} \tag{2.13}$$

in which s is the degree of saturation.

These partial stresses values make up the total stress tensor of the mixture, σ_{ij}, as

$$\sigma_{ij} = \sum_{\alpha} \sigma_{ij}^{\alpha} = \sigma_{ij}^{'} + n^{\mathrm{S}} P^{F} \delta_{ij} + n^{\mathrm{W}} P^{\mathrm{W}} \delta_{ij} + n^{\mathrm{G}} P^{\mathrm{G}} \delta_{ij} = \sigma_{ij}^{'} + P^{F} \delta_{ij} \tag{2.14}$$

Skeleton stress $\sigma_{ij}^{'}$ in the present study is defined as

$$\sigma_{ij}^{'} = \sigma_{ij} - P^{F} \delta_{ij} \tag{2.15}$$

From the viewpoint of the mixture theory, the adoption of the skeleton stress represents a natural application of the mixture theory to unsaturated soil. Therefore, it is possible to formulate a model for unsaturated soil starting from a model for saturated soil by substituting the skeleton stress for the effective stress.

2.2.3 Elastic Strain Rate

It is assumed that the strain rate tensor consists of elastic stretching tensor D_{ij}^{e} and viscoplastic stretching tensor D_{ij}^{vp} as

$$D_{ij} = D_{ij}^{e} + D_{ij}^{vp} \tag{2.16}$$

The elastic stretching tensor is given by the generalized Hooke type of law, namely,

$$D_{ij}^{e} = \frac{1}{2G}\dot{S}_{ij} + \frac{\kappa}{3(1+e)}\frac{\dot{\sigma}_m^{'}}{\sigma_m^{'}}\delta_{ij} \tag{2.17}$$

Where S_{ij} is the deviatoric stress tensor, $\sigma_m^{'}$ is the mean skeleton stress, G is the elastic shear modulus, e is the initial void ratio, κ is the swelling index, and the superimposed dot denotes the time differentiation.

2.2.4 Overconsolidation Boundary Surface

In the model, the overconsolidation boundary surface is defined to delineate the normally consolidated (NC) region, $f_b \geq 0$, and the overconsolidated (OC) region, $f_b < 0$, as follows:

$$f_b = \overline{\eta}_{(0)}^{*} + M_m^{*} \ln \frac{\sigma_m^{'}}{\sigma_{mb}^{'}} = 0 \tag{2.18}$$

$$\overline{\eta}_{(0)}^{*} = \left\{ \left(\eta_{ij}^{*} - \eta_{ij(0)}^{*}\right)\left(\eta_{ij}^{*} - \eta_{ij(0)}^{*}\right) \right\}^{\frac{1}{2}} \tag{2.19}$$

where where η_{ij}^{*} is the stress ratio tensor ($\eta_{ij}^{*} = S_{ij} / \sigma_m^{'}$), and (0) denotes the state at the end of the consolidation, in other words, the initial state before deformation occurs. M_m^{*} is the value of $\eta^{*} = \sqrt{\eta_{ij}^{*}\eta_{ij}^{*}}$ when the volumeric strain increment changes from compression to swelling, which is equal to the ratio M_f^{*} at the critical state.

σ'_{mb} is the strain-hardening parameter, which controls the size of the boundary surface. In the present model, the hardening parameter is assumed to be a function of viscoplastic strain ε_{ij}^{vp} and suction P^C. In order to describe the structure degradation of natural clay, strain-softening with viscoplastic strain is introduced into the hardening parameter in addition to the hardening with the viscoplastic volumetric strain. Meanwhile, to describe the suction effect on the unsaturated soil, suction is incorporated into the value of σ'_{mb} as

$$\sigma'_{mb} = \sigma'_{ma} \exp(\frac{1+e}{\lambda-\kappa}\varepsilon_{kk}^{vp})\left[1 + S_I \exp\left\{-S_d(\frac{P_i^c}{P^c}-1)\right\}\right] \tag{2.20}$$

where ε_{kk}^{vp} is the viscoplastic volumetric strain, λ and κ are the compression and the swelling index, respectively, and e_0 is the initial void ratio. σ'_{ma} is a strain-softening parameter used to describes the structure degradation effect, which is assumed to decrease with an increasing viscoplastic strain, namely

$$\sigma'_{ma} = \sigma'_{maf} + \left(\sigma'_{mai} - \sigma'_{maf}\right)\exp(-\beta z) \tag{2.21}$$

$$z = \int_0^t \dot{z}dt\,; \quad \dot{z} = \sqrt{\dot{\varepsilon}_{ij}^{vp}\dot{\varepsilon}_{ij}^{vp}} \tag{2.22}$$

in which, σ'_{mai} and σ'_{maf} are the initial and the final values for σ'_{ma}, respectively, and β is a material parameter that controls the rate of structural changes. Since viscoplastic strain is equal to 0 at the initial state, we can obtain the consolidation yield stress σ'_{mbi} is equal to σ'_{mai}.

The last term in Eq. (2.20) is adopted to reflect the suction effect on unsaturated soil. In which P^c is the present suction values, P_i^c is the reference suction, and S_I is a material parameter denoting the strength ratio to the saturated soil when the suction equals to reference suction P_i^c. And S_d is a material parameter which controls the rate of increase or decrease in σ'_{mb} with changes in suction. The change of hardening parameter with change of suction and the effect of parameter s_d are shown in Fig. 2.1

2.2.5 Static Yield Function

To describe the mechanical behavior of clay at its static equilibrium state, a Cam-clay type of static yield function is assumed to be

$$f_y = \overline{\eta}^*_{(0)} + \widetilde{M}^* \ln \frac{\sigma'_m}{\sigma'^{(s)}_{my}} = 0 \tag{2.23}$$

In the same way as the overconsolidation boundary surface, the suction effect is introduced for $\sigma'^{(s)}_{my}$.

$$\sigma'^{(s)}_{my} = \frac{\sigma'^{(s)}_{myi}}{\sigma'_{mai}} \sigma'_{ma} \exp\left(\frac{1+e}{\lambda - \kappa} \varepsilon^{vp}_{kk}\right) \left[1 + S_I \exp\left\{- S_d \left(\frac{P^c_i}{P^c} - 1\right)\right\}\right] \tag{2.24}$$

Parameter $\sigma'^{(s)}_{my}$, which controls the size of the static yield surface boundary, varies with the changes in suction as well as with viscoplastic volumetric strain and structure degradation.

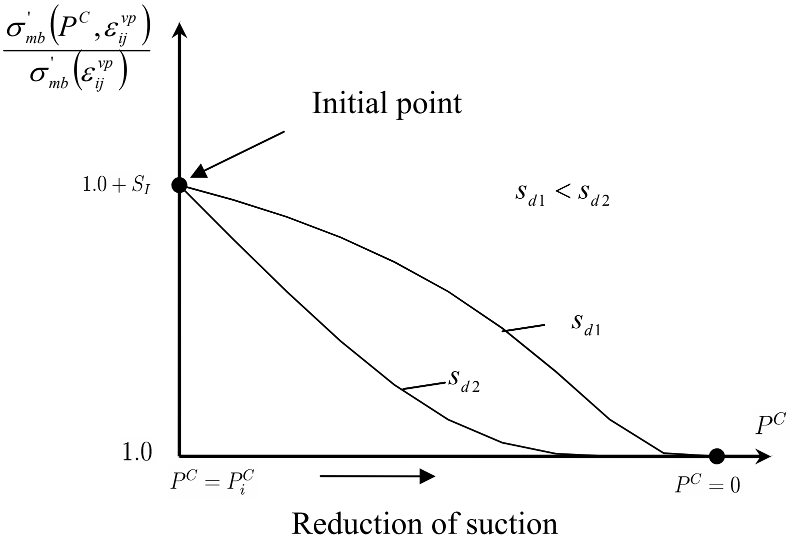

Figure 2.1 The strength degradation due to the reduction of suction

2.2.6 Viscoplastic Potential Function

The viscoplastic potential function is given by

$$f_p = \overline{\eta}^*_{(0)} + \widetilde{M}^* \ln \frac{\sigma'_m}{\sigma'_{mp}} = 0 \tag{2.25}$$

where $\widetilde{M}^*$ is assumed to be constant in the NC region and varies with the current stress in the OC region as

$$\tilde{M}^* = \begin{cases} M_m^* & : NC \quad region \\ -\dfrac{\sqrt{\eta_{ij}^*\eta_{ij}^*}}{\ln\left(\sigma_m^{'} / \sigma_{mc}^{'}\right)} & : OC \quad region \end{cases} \tag{2.26}$$

Where $\sigma_{mc}^{'}$ denotes the mean skeleton stress at the intersection of the overconsolidation boundary surface and the $\sigma_m^{'}$ axis as

$$\sigma_{mc}^{'} = \sigma_{mb}^{'} \exp \frac{\sqrt{\eta_{ij(0)}^*\eta_{ij(0)}^*}}{M_m^*} \tag{2.27}$$

In the case of isotropic consolidation, $\sigma_{mc}^{'}$ equals $\sigma_{mb}^{'}$. Due to the decrease of the suction, the shrinkage of the overconsolidation boundary surface, f_b, the static yield function, f_y, and the viscoplastic potential function, f_p, for $\eta_{ij(0)}^{'} = 0$, are illustrated in

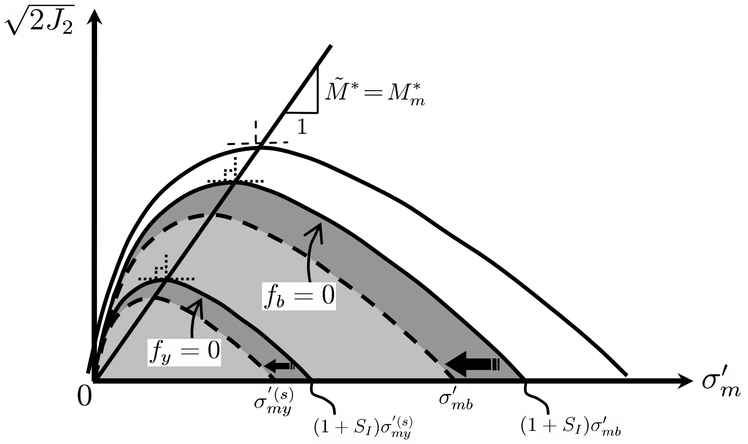
$\sqrt{2J_2}$
$\tilde{M}^* = M_m^*$
1
$f_b = 0$
$f_y = 0$
0
σ'_m
$\sigma'^{(s)}_{my}$
$(1+S_I)\sigma'^{(s)}_{my}$
σ'_{mb}
$(1+S_I)\sigma'_{mb}$

Figure 2.2 Shrinkage of the OC boundary surface, static yield function, and potential function in the NC region

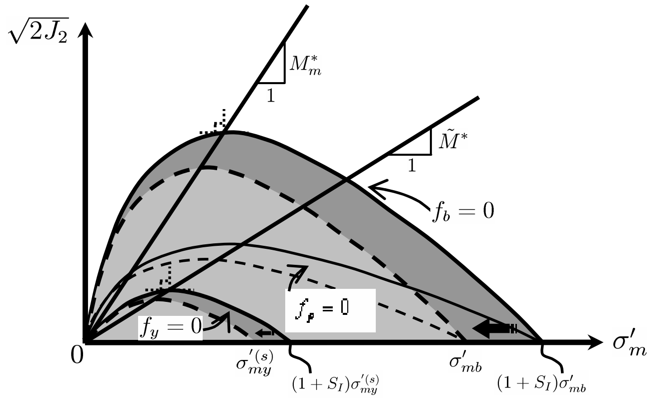
$\sqrt{2J_2}$
M_m^*
1
$\tilde{M}^*$
1
$f_b = 0$
$f_p = 0$
$f_y = 0$
0
σ'_m
$\sigma'^{(s)}_{my}$
$(1+S_I)\sigma'^{(s)}_{my}$
σ'_{mb}
$(1+S_I)\sigma'_{mb}$

Figure 2.3 Shrinkage of the OC boundary surface, static yield function, and potential function in the OC region

the schematically described in the $\sigma_m' \sim \sqrt{2J_2}$ space for the NC regions in Figs. 2.2 and 2.3, respectively. It can be seen that σ_{mb}' and $\sigma_{my}'^{(s)}$ decrease with decreasing suction owing to wetting. The increments in viscoplastic strain for the overstress type model depend on the difference between the current stress state and the static yield stress state, therefore, the shrinkage of f_y due to the wetting yields increases in the viscoplastic strain increments.

2.2.7 Viscoplastic Flow Rule

The viscoplastic stretching tensor is expressed by the following equation which is based on Perzyna's type of viscoplastic theory (Perzyna, 1963; Oka, 1982) as

$$D_{ij}^{vp} = \gamma \langle \Phi_1 (f_y) \rangle \frac{\partial f_p}{\partial \sigma_{ij}'} \tag{2.28}$$

in which $\langle \ \rangle$ are Macaulay's brackets; $\langle \Phi_1 (f_y) \rangle = \Phi_1 (f_y)$, if $f_y > 0$ and $\langle \Phi_1 (f_y) \rangle = 0$, if $f_y \le 0$. Φ_1 indicates strain rate sensitivity. Based on the experimental data from the strain rate constant triaxial tests, the material function is given as

$$\begin{aligned} \gamma \Phi_1 (f_y) &= C' \sigma_m' \exp\left\{ m' \left(\overline{\eta}_{(0)}^* + \tilde{M}^* \ln \frac{\sigma_m'}{\sigma_{my}'} \right) \right\} \\ &= C' \sigma_m' \exp\left\{ m' \left(\overline{\eta}_{(0)}^* + \tilde{M}^* \ln \frac{\sigma_{mai}'}{\sigma_{myi}'^{(s)}} \frac{\sigma_m'}{\sigma_{mb}'} \right) \right\} \\ &= C \sigma_m' \exp\left\{ m' \left(\overline{\eta}_{(0)}^* + \tilde{M}^* \ln \frac{\sigma_m'}{\sigma_{mb}'} \right) \right\} \end{aligned} \tag{2.29}$$

$$C = C' \exp\left(m' \tilde{M}^* \ln \frac{\sigma_{mai}'}{\sigma_{myi}'^{(s)}} \right) \tag{2.30}$$

Finally, using the fourth rank isotropic tensor, C_{ijkl}, the viscoplastic stretching tensor is given by the following equation:

$$D_{ij}^{vp} = \begin{cases} C_{ijkl} \sigma_m' \exp\left\{ m' \left(\overline{\eta}_{(0)}^* + \tilde{M}^* \ln \dfrac{\sigma_m'}{\sigma_{mb}'} \right) \right\} \dfrac{\partial f_p}{\partial \sigma_{kl}'} : & f_y > 0 \\ 0 \qquad\qquad : & f_y \le 0 \end{cases} \tag{2.31}$$

where viscoplastic parameter C_{ijkl} is given by

$$C_{ijkl} = a \delta_{ij} \delta_{kl} + b \left(\delta_{ik} \delta_{jl} + \delta_{il} \delta_{jk} \right) \tag{2.32}$$

The viscoplastic deviatoric strain rate and the viscoplastic volumetric strain rate are obtained as follows:

$$\dot{e}_{ij}^{vp} = C_1 \exp\left\{ m' \left(\overline{\eta}_{(0)}^{*} + \widetilde{M}^{*} \ln \frac{\sigma_m'}{\sigma_{mb}'} \right) \right\} \frac{\eta_{ij}^{*} - \eta_{ij(0)}^{*}}{\overline{\eta}^{*}} \tag{2.33}$$

$$\dot{\varepsilon}_{kk}^{vp} = C_2 \exp\left\{ m' \left(\overline{\eta}_{(0)}^{*} + \widetilde{M}^{*} \ln \frac{\sigma_m'}{\sigma_{mb}'} \right) \right\} \left\{ \widetilde{M}^{*} - \frac{\eta_{mn}^{*} \left(\eta_{mn}^{*} - \eta_{mn(0)}^{*} \right)}{\overline{\eta}^{*}} \right\} \tag{2.34}$$

Where C_1 and C_2 are the viscoplastic parameters for the deviatoric and the volumetric components, respectively,

$$C_1 = 2b, \quad C_2 = 3a + 2b \tag{2.35}$$

2.3 Multiphase Finite Element Formulation for the Analysis of Unsaturated Soil

Unsaturated soil is composed of three constituents, namely, solid particles, water, and air, which in the context of the mixture theory, are viewed as three independent overlapping continua in the context of the mixture theory. The behavior of the multiphase materials can be described within the framework of a macroscopic continuum mechanical approach through the use of the theory of porous media. The theory is considered to be a generalization of Biot's two-phase mixture theory for unsaturated soil. The three phases represent the constituents when viewed as a part of the mixture, also referred to as a porous medium.

Proceeding from the general geometrically non-linear formulation, the governing balance relations for multiphase materials can be obtained as many researchers have mentioned (Ehlers 2003; Loret and Khalili 2000). Mass conservation laws for the gas phase, as well as for the liquid phase, are considered in those analyses.

2.3.1 Hydraulic Property of Unsaturated Soil

2.3.1.1 Soil-water Characteristic Curve

The soil-water characteristic curve (SWCC) for soil is defined as the relationship between the degrees of saturation and suction for soil. The SWCC can be described as a measure of the water-holding capacity (i.e., the storage capacity) of the soil as the water content changes when it is subjected to various levels of suction. In the model, the van Genuchten type of equation (1980) is adopted as

$$s_{re} = \{1 + (\alpha P^C)^n\}^{-m} \tag{2.36}$$

where α , m and n are material parameters and the relation $m = 1 - 1/n$ is assumed. $P^C\left(= P^G - P^W\right)$ is the suction and s_{re} is the effective degree of saturation, namely,

$$s_{re} = \frac{(s - s_{\min})}{(s_{\max} - s_{\min})} \tag{2.37}$$

where $s_{\min}$ and $s_{\max}$ are the minimum and the maximum saturation values, respectively.

2.3.1.2 Flow law

In the present model, a Darcy type of equation is applied for the flow of water and air as

$$V_i^W = \frac{k^W}{\gamma^W}\{(P^W \delta_{ji})_{,j} + \rho_W \bar{F}_i\} \quad , \qquad V_i^G = \frac{k^G}{\gamma^G}\left(P^G \delta_{ji}\right)_{,j} \tag{2.38}$$

where k^W and k^G are the coefficients of the permeability for water and for air respectively. They are functions of any two of three possible volume-mass properties, namely, degree of saturation, void ratio, and water content (Lloret and Alonso 1980; Fredlund 1981). In present analysis, the permeability is assumed to be affected by the degree of saturation and void ratio. The effect of degree of saturation on permeability for water and air are assumed as (Lu and Likos 2004).

$$k^W = k_s^W s^a \left\{1 - \left(1 - s^{\frac{1}{m}}\right)^n\right\}, \qquad k^G = k_s^G (1 - s)^b \left\{1 - \left(s^{\frac{1}{m}}\right)^n\right\} \tag{2.39}$$

where a and b are the material parameters, and m and n are the parameters in the van Genuchten equation (1980). k_s^W is the coefficient of permeability for water under saturated conditions at a given void ratio, and k_s^G is the permeability of air under fully dry conditions. k_s^W and k_s^W depend on void ratio e in the following form:

$$k_s^W = k_{s0}^W \exp[(e - e_0)/C_k] \qquad k_s^G = k_{s0}^G \exp[(e - e_0)/C_k] \tag{2.40}$$

in which k_{s0}^{W} and k_{s0}^{W} are the initial value for k_s^{W} and k_s^{W} at $e = e_0$ respectively. C_k is the material constant governing the rate of changes in permeability subjected to changes in the void ratio.

2.3.2 Conservation of Momentum

Based on the Truesdell's "Metaphysical Principles" of mixture theories (Truesdell 1984), the momentum balance for each phase in given by,

$$n^{\alpha}\rho_{\alpha}\dot{v}_i^{\alpha} = \sigma_{ji,j}^{\alpha} + \rho_{\alpha}n^{\alpha}\overline{F}_i - \widetilde{P}_i^{\alpha} - \sum_{\gamma} D^{\alpha\gamma}(v_i^{\alpha} - v_i^{\gamma}) \qquad (\alpha = \mathrm{S,W,G}) \tag{2.41}$$

in which $\overline{F}_i$ is the gravity force and $D^{\alpha\gamma}$ ($D^{\alpha\gamma} = D^{\gamma\alpha}$) are parameters which describe the interaction between phase α and another phase γ, which is defined as,

$$D^{\mathrm{WS}} = \frac{(n^{W})^2\rho_{\mathrm{W}}g}{k^{\mathrm{W}}} \quad , \quad D^{\mathrm{GS}} = \frac{(n^{G})^2\rho_{\mathrm{G}}g}{k^{\mathrm{G}}} \tag{2.42}$$

in which, g is the acceleration of gravity, and k^{W} and k^{G} are the permeability coefficients for the liquid phase and the gas phase, respectively. The momentum balance equation for solid (S), water (W), and gas (G) phases is respectively obtained with the following equations:

$$\text{S:} \quad \sigma'_{ji,j} + \left(n^{\mathrm{S}}P^{F}\delta_{ji}\right)_{,j} + \rho_{\mathrm{S}}n^{\mathrm{S}}\,\overline{F}_i - D^{\mathrm{SW}}\left(v_i^{\mathrm{S}} - v_i^{\mathrm{W}}\right) - D^{\mathrm{SG}}\left(v_i^{\mathrm{S}} - v_i^{\mathrm{G}}\right) = n^{\mathrm{S}}\rho_{\mathrm{S}}\dot{v}_i^{\mathrm{S}} \tag{2.43}$$

$$\text{W:} \quad \left(n^{\mathrm{W}}P^{\mathrm{W}}\right)_{i,j} + \rho_{\mathrm{W}}n^{\mathrm{W}}\overline{F}_i - D^{\mathrm{WS}}\left(v_i^{\mathrm{W}} - v_i^{\mathrm{S}}\right) - D^{\mathrm{WG}}\left(v_i^{\mathrm{W}} - v_i^{\mathrm{G}}\right) = n^{\mathrm{W}}\rho_{\mathrm{W}}\dot{v}_i^{\mathrm{W}} \tag{2.44}$$

$$\text{G:} \quad \left(n^{\mathrm{G}}P^{\mathrm{G}}\right)_{i,j} + \rho_{\mathrm{G}}n^{\mathrm{G}}\overline{F}_i - D^{\mathrm{GS}}\left(v_i^{\mathrm{G}} - v_i^{\mathrm{S}}\right) - D^{\mathrm{GW}}\left(v_i^{\mathrm{G}} - v_i^{\mathrm{W}}\right) = n^{\mathrm{G}}\rho_{\mathrm{G}}\dot{v}_i^{\mathrm{G}} \tag{2.45}$$

When we assume that the deformation is quasi-static process ($\dot{v}_i^{\alpha} = 0$), and them the space derivative of volume fraction $n_{,i}^{\beta}$ is negligible, the sum of the momentum balance equations leads to

$$
\begin{aligned}
&\sigma'_{ji,j} + \left(n^{\mathrm{S}} P^F \delta_{ji}\right)_{,j} + \rho_{\mathrm{S}} n^{\mathrm{S}} \overline{F}_i + \left(n^{\mathrm{W}} P^W \delta_{ji}\right)_{,j} \\
&\quad + \rho_{\mathrm{W}} n^{\mathrm{W}} \overline{F}_i + \left(n^{\mathrm{G}} P^G \delta_{ji}\right)_{,j} + \rho_{\mathrm{G}}\, n^{\mathrm{G}}\, \overline{F}_i \\
&= \sigma'_{ji,j} + \left(P^F\ \delta_{ji}\right)_{,j} + \left(\rho_{\mathrm{S}} n^{\mathrm{S}} + \rho_{\mathrm{W}} n^{\mathrm{W}} + \rho_{\mathrm{G}} n^{\mathrm{G}}\right)\overline{F}_i \\
&= \sigma'_{ji,j} + \left(P^F \delta_{ji}\right)_{,j} + \rho\, \overline{F}_i = 0
\end{aligned}
\tag{2.46}
$$

Substituting Equation (2.8) into Equation (2.46) yields

$$\sigma_{ji,j} + \rho \overline{F}_i = 0 \tag{2.47}$$

The rate type of conservation for the momentum by the material derivative of the equilibrium equations in the current configuration is given by

$$\dot{S}_{ji,j} = 0 \tag{2.48}$$

in which changes in the material density are ignored. The above, the total nominal stress rate tensor, $\dot{S}_{ji}$, is defined as

$$\dot{S}_{ji} = \dot{T}_{ij} + L_{pp} T_{ij} - T_{in} L_{jn} \tag{2.49}$$

where T_{ij} is the Cauchy stress tensor, $\dot{T}_{ij}$ is the rate type of the Cauchy stress tensor, and L_{ij} is the velocity gradient tensor. The relation between the Cauchy stress tensor and the skeleton Cauchy stress tensor is given as

$$T_{ij} = T'_{ij} + P^F \delta_{ij} \tag{2.50}$$

The time rate of the Cauchy stress tensor is given as

$$\dot{T}_{ij} = \dot{T}'_{ij} + \dot{P}^F \delta_{ij} \tag{2.51}$$

From the above equations, we have

$$
\begin{aligned}
\dot{S}_{ji} &= \left(\dot{T}'_{ij} + \dot{P}^F \delta_{ij}\right) + L_{pp}\left(T'_{ij} + P^F \delta_{ij}\right) - \left(T'_{in} + P^F \delta_{in}\right) L_{jn} \\
&= \left(\dot{T}'_{ij} + L_{pp} T'_{ij} - T'_{in} L_{jn}\right) + \dot{P}^F \delta_{ij} + L_{pp} P^F \delta_{ij} - P^F \delta_{in} L_{jn} \\
&= \dot{S}'_{ij} + \dot{P}^F \delta_{ij} + L_{pp} P^F \delta_{ij} - P^F \delta_{in} L_{jn}
\end{aligned}
\tag{2.52}
$$

in which, the skeleton stress rate tensor, $\dot{S}'_{ij}$, is defined as

$$\dot{S}'_{ij} = \left(\dot{T}'_{ij} + L_{pp}T'_{ij} - T'_{in}L_{jn}\right) \tag{2.53}$$

The boundary conditions are given by

$$\dot{S}_{ij}n_j = \dot{\bar{S}}_i \quad \text{on} \quad \partial D_t \tag{2.54}$$

$$v_i = \bar{v}_i \quad \text{on} \quad \partial D_u \tag{2.55}$$

As shown in Fig. 2.4, ∂D_t and ∂D_u are the parts of the closed boundary ∂D, of which the stress rate and the displacement rate are prescribed as $\dot{\bar{S}}_i$ and $\bar{v}_i$, respectively. It is obvious that they satisfy the following relations:

$$\partial D_t \bigcup \partial D_u = \partial D \quad \text{and} \quad \partial D_t \bigcap \partial D_u = 0 \tag{2.56}$$

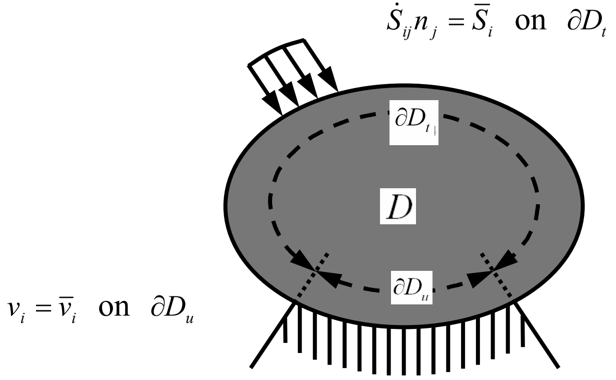
$\dot{S}_{ij}n_j = \dot{\bar{S}}_i$ on ∂D_t
∂D_t
D
∂D_u
$v_i = \bar{v}_i$ on ∂D_u

Figure 2.4 Boundary conditions for the whole fluid-solid mixture

Considering the closed domain D at current time, $t = t$, the weak form of the rate type of equilibrium equation (2.48) is given as follows:

$$\int_D \dot{S}_{ji,j}\delta v_i dV = 0 \tag{2.57}$$

in which δv_i is the virtual velocity.

From the relation

$$\left(\dot{S}_{ji}\delta v_i\right)_{,j} = \dot{S}_{ji,j}\delta v_i + \dot{S}_{ji}\delta v_{i,j} \tag{2.58}$$

Equation (2.57) can be rewritten as

$$\int_D \left(\dot{S}_{ji}\delta v_i\right)_{,j} dV - \int_D \dot{S}_{ji}\delta v_{i,j} dV = 0 \tag{2.59}$$

Applying the Gauss theorem and the compatibility conditions, i.e., $\delta v_{i,j} = \delta L_{ij}$, Equation (2.59) can be written as

$$\int_{\partial D} \left(\dot{S}_{ji}\delta v_i\right) n_j dS - \int_D \dot{S}_{ji}\delta L_{ij} dV = 0 \tag{2.60}$$

Incorporating Equation (2.52) into Equation (2.60) and transforming the first term by the following relation

$$\dot{S}_i = \dot{S}_{ji} n_j \tag{2.61}$$

yields

$$\int_D \dot{S}'_{ji}\delta L_{ij} dV + \int_D \dot{P}^F \delta_{ji}\delta L_{ij} dV + \int_D \left(L_{pp} P^F \delta_{ji} - P^F \delta_{jn} L_{in}\right) \delta L_{ij} dV = \int_{\partial D_t} \dot{\bar{S}}_i \delta v_i dS \tag{2.62}$$

Since the stretching tensor D_{ij} is defined as

$$D_{ij} = \frac{1}{2}(L_{ij} + L_{ji}) \tag{2.63}$$

The following relation is used:

$$\delta_{ji}\delta L_{ij} = \delta L_{ii} = \delta D_{ii} = tr\delta D \tag{2.64}$$

From the symmetry of the effective Cauchy stress tensor,

$$\dot{T}_{ji}\delta L_{ij} = \frac{1}{2}\dot{T}_{ji}(\delta L_{ij} + \delta L_{ji}) = \dot{T}_{ji}\delta D_{ij} \tag{2.65}$$

Substituting Equations (2.64) and (2.65) and the skeleton stress tensor rate, Equation (2.53) into Equation (2.62) gives

$$\begin{aligned} &\int_D \dot{T}'_{ji}\delta D_{ij} dV - \int_D T'_{jk} L_{ik}\delta L_{ij} dV + \int_D T'_{ji} trL\delta L_{ij} dV + \int_D \dot{P}^F tr\delta D dV \\ &\quad + \int_D \left(L_{pp} P^F \delta_{ji} - P^F \delta_{jn} L_{in}\right) \delta L_{ij} dV = \int_{\partial D_t} \dot{\bar{S}}_i \delta v_i dS \end{aligned} \tag{2.66}$$

In this formulation, the finite deformation theory and updated Lagrangian method is adopted. Thus, the Jaumann rate of effective Cauchy stress tensor $\hat{T}_{ij}^{'}$ is adopted for the constitutive model (Oka et al. 2002; Higo 2003; Higo et al. 2006; Kimoto 2007). The Jaumann rate of the effective Cauchy stress tensor is the objective tensor; it is defined as

$$\hat{T}_{ij}^{'} = \dot{T}_{ij}^{'} - W_{ik}T_{kj}^{'} + T_{ik}^{'}W_{kj} \tag{2.67}$$

where W_{ij} is the spin tensor, namely,

$$W_{ij} = \frac{1}{2}\left(L_{ij} - L_{ji}\right) \tag{2.68}$$

Stretching tensor D_{ij} is assumed to be a composition of elastic stretching tensor D_{ij}^{e} and viscoplastic stretching tensor D_{ij}^{vp} , that is,

$$D_{ij} = D_{ij}^{e} + D_{ij}^{vp} \tag{2.69}$$

The relation between elastic stretching tensor D_{ij}^{e} and the Jaumann rate of Cauchy stress tensor $\hat{T}_{ij}^{'}$ can be obtained as

$$\hat{T}_{ij}^{'} = C_{ijkl}^{e}D_{kl}^{e} \tag{2.70}$$

where C_{ijkl}^{e} is the elastic stiffness matrix.

Herein, the tangent modulus method (as mentioned in Section 2.3.3) is adopted in order to evaluate viscoplastic stretching tensor D_{ij}^{vp} (Oka et al. 1992; Higo 2003) as

$$\hat{T}_{ij}^{'} = C_{ijkl}^{\tan}D_{kl} - Q_{ij} \tag{2.71}$$

in which $C_{ijkl}^{\tan}$ is the tangential stiffness matrix, and Q_{ij} is the relaxation stress. Substituting Equation (2.71) into Equation (2.67) yields the following in matrix form:

$$\left\{\dot{T}^{'}\right\} = \left[C\right]\left\{D\right\} - \left\{Q\right\} + \left\{W^{*}\right\} \tag{2.72}$$

where $\{W^*\}=\{WT'\}-\{T'W\}$is the vector related to the spin tensor.

According to Equation (2.13), the time derivative of P^F can be expressed as

$$\begin{aligned} \dot{P}^F &= \frac{\partial}{\partial t}\left\{ sP^{\mathrm{W}} + (1-s)P^{\mathrm{G}}) \right\} \\ &= \left\{ \frac{\partial s}{\partial P^C}(P^{\mathrm{W}} - P^{\mathrm{G}}) + (1-s) \right\} \dot{P}^{\mathrm{G}} + \left\{ -\frac{\partial s}{\partial P^C}(P^{\mathrm{W}} - P^{\mathrm{G}}) + s \right\} \dot{P}^{\mathrm{w}} \\ &= \{A_s + (1-s)\} \dot{P}^{\mathrm{G}} + \{-A_s + s\} \dot{P}^{\mathrm{w}} \end{aligned} \tag{2.73}$$

where

$$A_s = \frac{\partial s}{\partial P^C}(P^{\mathrm{W}} - P^{\mathrm{G}}) \tag{2.74}$$

From the soil water characteristic curve defined in Equation (2.36),

$$\frac{\partial s}{\partial P^C} = -\alpha\, m\, n\ (s_{\max} - s_{\min})(\alpha P^C)^{n-1} \left\{ 1 + (\alpha P^C)^n \right\}^{-m-1} \tag{2.75}$$

For the discretization of the weak form of the equilibrium equation, the following relations are defined:

$$\{D\} = [B]\{v^*\},\ \ trD = \{B_v\}^T\{v^*\} \tag{2.76}$$

in which $[B]$ is the matrix which transforms the nodal velocity vector $\{v^*\}$ to the stretching tensor$\{D\}$. is the velocity vector in an element, and $\{B_v\}$ is the vector which transforms the nodal velocity into the trace of $\{D\}$.

$$\{P^\beta\} = [N_h]\{P^{\beta *}\},\quad \{\dot{P}^\beta\} = [N_h]\{\dot{P}^{\beta *}\} \tag{2.77}$$

in which $\{N_h\}$ represents the element shape function which transforms the nodal pore pressure $\{P^{\beta *}\}$ and the nodal pore pressure rate vector $\{\dot{P}^{\beta *}\}$ into the pore pressure vector $\{P^\beta\}$ and the rate vector $\{\dot{P}^\beta\}$.

$$\{P^\beta_{,i}\} = \{N_{h,i}\}\{P^{\beta *}\} = [B_h]\{P^{\beta *}\} \tag{2.78}$$

in which $\left[B_h\right]$ is the matrix which transforms the nodal pore pressure vector to the vector form of pore pressure gradient.

$$\{L\} = [\, B_M\,]\left\{\, v^*\right\} \tag{2.79}$$

where $[\ B_M\,]$ is the matrix which transforms the nodal velocity vector into the velocity gradient vector $\{L\}$. Meanwhile, the other two items in Equation (2.66) are expressed as

$$\left\{- T'_{ik}\, L_{jk}\right\} = \left[D'_s\right][\, B_M\,]\left\{v^*\right\} \tag{2.80}$$

$$\left\{\, L_{pp} P^F \delta_{ji} - P^F \delta_{jn} L_{in}\right\} = [U][\, B_M\,]\left\{v^*\right\} \tag{2.81}$$

By all the obtained matrix and vector relations obtained previously, Equation (2.66) can be expressed as

$$\begin{aligned}
&\int_D \left\{\delta v^*\right\}^T [\,B\,]^T [\,C\,][B]\left\{v^*\right\} dV - \int_D \left\{\delta v^*\right\}^T [\,B\,]^T \{\,Q\,\} dV + \int_D \left\{\delta v^*\right\}^T [\,B\,]^T \{\,W\} dV \\
&\quad + \int_D \left\{\delta v^*\right\}^T [\,B_M\,]^T \left[D'_s\right][\,B_M\,]\left\{v^*\right\} dV + \int_D \left\{\delta v^*\right\}^T [\,B_M\,]^T \left[T'\right]\{B_v\}^T \left\{v^*\right\} dV \\
&\quad + \int_D \left\{\delta v^*\right\}^T (-\,A_s + s)\{\,B_v\}\{\,N_h\}\left\{\dot{P}^{W*}\right\} dV \\
&\quad + \int_D \left\{\delta v^*\right\}^T \{\,A_s + (1+s)\,\}[\,B_v\,]\{\,N_h\}\left\{\dot{P}^{G*}\right\} dV \\
&\int_D \left\{\delta v^*\right\}^T [\,B_M\,]^T [\,U\,]\,[\,B_M\,]\left\{v^*\right\} dV = \int_{\partial D_t} \left\{\delta v^*\right\}^T \{\,N_h\}^T \left\{\dot{\bar{S}}\right\} dS
\end{aligned} \tag{2.82}$$

Based on the theory of virtual displacement, Equation (2.82) is divided by $\left\{\ \delta v^*\right\}^T$

$$[K]\left\{v^*\right\} + [K_L]\left\{v^*\right\} + (-A_s + s)\,[K_v]\left\{\dot{P}^{W*}\right\} + \{A_s + (1-s)\ \}[K_v]\left\{\dot{P}^{G*}\right\} = \{\,V\} + \{\,F\} \tag{2.83}$$

in which

$$[K] = \int_D [B]^T [C][B] dV \tag{2.84}$$

$$[K_L] = \int_D [B_M]^T \left[D'_s\right][B_M] dV + \int_D [B_M]^T \left[T'\right]\{B_v\}^T dV + \int_D [B_M]^T [U][B_M] dV \tag{2.85}$$

$$[K_v] = \int_D \{\,B_v\}\{N_h\} dV \tag{2.86}$$

$$\{\,V\} = \int_{\partial D_t} \{N_h\}^T \left\{\,\dot{\bar{S}}\right\} dS \tag{2.87}$$

$$[\,F\,] = \int_D [B]^T [\,Q\,] dV - \int_D [B]^T [\,W\,] dV \tag{2.88}$$

The relation between the nodal velocity vector $\left\{ v^{*} \right\}$ and the nodal displacement increment vector $\left\{ \Delta u^{*} \right\}$ can be obtained by using Euler's approximation as

$$\left\{ v^{*} \right\} = \frac{\left\{ \Delta u^{*} \right\}}{\Delta t} \tag{2.89}$$

Similarly, the pore water pressure and the pore air pressure can be obtained as

$$\left\{ \dot{P}^{\mathrm{W}} \right\} = \frac{\left\{ P^{\mathrm{W}*} \right\}_{t+\Delta t} - \left\{ P^{\mathrm{W}*} \right\}_{t}}{\Delta t}, \quad \left\{ \dot{P}^{\mathrm{G}} \right\} = \frac{\left\{ P^{\mathrm{G}*} \right\}_{t+\Delta t} - \left\{ P^{\mathrm{G}*} \right\}_{t}}{\Delta t} \tag{2.90}$$

Incorporating Equations (2.89) and (2.90) into Equation (2.83), the weak form of the equilibrium equations is obtained, that is,

$$\begin{aligned} &\left([K] + [K_L] \right) \left\{ \Delta u^{*} \right\} + (-A_s + s)[K_v] \left\{ P^{\mathrm{W}*} \right\}_{t+\Delta t} + \left\{ A_s + (1-s) \right\} [K_v] \left\{ P^{\mathrm{G}*} \right\}_{t+\Delta t} \\ &= \Delta t \left(\{V\} + \{F\} \right) + (-A_s + s)[K_v] \left\{ P^{\mathrm{W}*} \right\}_{t} + \left\{ A_s + (1-s) \right\} [K_v] \left\{ P^{\mathrm{G}*} \right\}_{t} \end{aligned} \tag{2.91}$$

2.3.3 Tangent Stiffness Method

In this section, we will derive the relation between the Jaumann rate of Cauchy's stress and the stretching tensor using the tangent stiffness method from Pierce et al. (1984). As shown in Equation (2.69), the total stretching tensor is being divided between the elastic stretching tensor D_{ij}^{e} and the viscoplastic stretching tensor D_{ij}^{vp}. The elastic stretching tensor is being defined in Equation (2.70). The viscoplastic stretching tensor is defined as

$$D_{ij}^{vp} = C_{ijkl} \left\langle \Phi(f_y) \right\rangle \frac{\partial f_p}{\partial T_{kl}^{'}} \tag{2.92}$$

Material function $\Phi(f_y)$ depends only on the Cauchy stress tensor $T_{ij}^{'}$ and the viscoplastic volumetric strain tensor v^{vp}. As such, the time derivative $\Phi(f_y)$ can be written as

$$\dot{\Phi}(f_y) = \frac{\partial \Phi}{\partial T_{ij}^{'}} \dot{T}_{ij}^{'} + \frac{\partial \Phi}{\partial v^{vp}} \dot{v}^{vp} \tag{2.93}$$

The rate of Cauchy stress can be derived from the Jaumann rate of Cauchy stress as

$$\hat{T}_{ij}^{'} = \dot{T}_{ij}^{'} - W_{ik} T_{kj}^{'} + T_{ik}^{'} W_{kj} \tag{2.94}$$

where W_{ij} is the spin tensor.

Using two scalars, A and B, and a symmetric tensor U_{ij}, we can write

$$
\begin{aligned}
\frac{\partial \Phi}{\partial T'_{ij}} \hat{T}'_{ij} &= \frac{\partial \Phi}{\partial T'_{ij}} \left(\dot{T}'_{ij} - W_{ik} T'_{kj} + T'_{ik} W_{kj} \right) \\
&= \frac{\partial \Phi}{\partial T'_{ij}} \dot{T}'_{ij} + \frac{\partial \Phi}{\partial T'_{ij}} \left(- W_{ik} T'_{kj} + T'_{ik} W_{kj} \right) \\
&= \frac{\partial \Phi}{\partial T'_{ij}} \dot{T}'_{ij} + \left(A U_{ij} + B \delta_{ij} \right) \left(- W_{ik} T'_{kj} + T'_{ik} W_{kj} \right)
\end{aligned} \tag{2.95}
$$

We then have

$$A U_{ij} \left(- W_{ik} \, T'_{kj} + T'_{ik} \, W_{kj} \right) = A \left(U_{ki} \, T'_{ij} - U_{ki} \, T'_{ji} \right) W_{kj} = 0 \tag{2.96}$$

$$B \, \delta_{ij} \left(- W_{ik} \, T'_{kj} + T'_{ik} \, W_{kj} \right) = B \left(- W_{ki} \, T'_{ik} + T'_{ik} \, W_{ki} \right) = 0 \tag{2.97}$$

Substituting Equations (2.96) and (2.97) into Equation (2.95), we obtain

$$\frac{\partial \Phi}{\partial T'_{ij}} \hat{T}'_{ij} = \frac{\partial \Phi}{\partial T'_{ij}} \dot{T}'_{ij} \tag{2.98}$$

Then, substituting Equation (2.98) into Equation (2.93), we have

$$\dot{\Phi}\left(f_y \right) = \frac{\partial \Phi}{\partial T'_{ij}} \hat{T}'_{ij} + \frac{\partial \Phi}{\partial v^{vp}} \dot{v}^{vp} \tag{2.99}$$

Using the tangent stiffness parameter θ yields

$$\Phi = \left(1 - \theta \right) \Phi_t + \theta \, \Phi_{t+\Delta t} \tag{2.100}$$

where

$$\Phi_{t+\Delta t} = \Phi_t + \Delta \Phi = \Phi_t + \Delta t \, \dot{\Phi}_t \tag{2.101}$$

Applying Equations. (2.99), (2.100), and (2.101), we obtain

$$\Phi = \left(1 - \theta \right) \Phi_t + \theta \left\{ \Phi_t + \frac{\partial \Phi}{\partial T'_{ij}} \hat{T}'_{ij} \, \Delta t + \frac{\partial \Phi}{\partial \varepsilon^{vp}_{kk}} \Delta v^{vp} \right\} \tag{2-102}$$

Using Equations (2.70) and (2.92), the Jaumann rate for Cauchy stress can be written as

$$
\begin{aligned}
\hat{T}'_{ij} &= C^e_{ijkl} \left(D_{kl} - D^{vp}_{kl} \right) \\
&= C^e_{ijkl} \left(D_{kl} - C_{klmn} \Phi \frac{\partial f_p}{\partial T'_{mn}} \right)
\end{aligned} \tag{2.103}
$$

We can derive Δv^{vp} from Equation (2.92) as follows

$$\Delta v^{vp} = v^{vp} \Delta t = \varepsilon^{vp}_{kk} \Delta t = C_{kkll} \Phi \frac{\partial f_p}{\partial T'_{ll}} \Delta t \tag{2.104}$$

Substituting Equations (2.103) and (2.104) into Equation (2.102) yields

$$
\begin{aligned}
\Phi &= (1-\theta)\Phi_t + \theta\left\{\Phi_t + \frac{\partial \Phi}{\partial T'_{ij}} C^e_{ijkl}\left(D_{kl} - C_{klmn}\Phi\frac{\partial f_p}{\partial T'_{mn}}\right)\Delta t + \frac{\partial \Phi}{\partial v^{vp}} C_{kkll}\Phi\frac{\partial f_p}{\partial T'_{ll}}\Delta t\right\} \\
&= \frac{1}{1+\xi'}\left\{\Phi_t + (\theta\Delta t)\frac{\partial \Phi}{\partial T'_{ij}} C^e_{ijkl} D_{kl}\right\}
\end{aligned}
\tag{2.105}
$$

$$
\xi' = (\theta\Delta t)\left\{\frac{\partial \Phi}{\partial T'_{ij}} C^e_{ijkl} C_{klmn}\frac{\partial f_p}{\partial T'_{mn}} - \frac{\partial \Phi}{\partial v^{vp}} C_{ppqq}\frac{\partial f_p}{\partial T'_{qq}}\right\}
\tag{2.106}
$$

Thus, substituting Equation (2.106) into Equation (2.92) leads to

$$
D^{vp}_{ij} = C_{ijkl}\frac{1}{1+\xi'}\left\{\Phi_t + (\theta\Delta t)\frac{\partial \Phi}{\partial T'_{pq}} C^e_{pqrs} D_{rs}\right\}\frac{\partial f_p}{\partial T'_{kl}}
\tag{2.107}
$$

From Equations (2.107) and (2.103), we obtain

$$
\begin{aligned}
\hat{T}'_{ij} &= C^e_{ijkl}\left(D_{kl} - C_{klmn}\frac{1}{1+\xi'}\left\{\Phi_t + (\theta\Delta t)\frac{\partial \Phi}{\partial T'_{pq}} C^e_{pqrs} D_{rs}\right\}\frac{\partial f_p}{\partial T'_{mn}}\right) \\
&= \left[C^e_{ijkl} - C^e_{ijrs} C_{rsmn}\frac{\partial f_p}{\partial T'_{mn}}\frac{1}{1+\xi'}(\theta\Delta t)\frac{\partial \Phi}{\partial T'_{pq}} C^e_{pqkl}\right] D_{kl} - C^e_{ijkl} C_{klmn}\frac{\partial f_p}{\partial T'_{mn}}\frac{1}{1+\xi'}\Phi_t
\end{aligned}
\tag{2.108}
$$

Tangential stiffness matrix $C^{\tan}_{ijkl}$ and relaxation stress Q_{ij} are defined as

$$
\begin{aligned}
C^{\tan}_{ijkl} &= C^e_{ijkl} - C^e_{ijrs} C_{rsmn}\frac{\partial f_p}{\partial T'_{mn}}\frac{1}{1+\xi'}(\theta\Delta t)\frac{\partial \Phi}{\partial T'_{pq}} C^e_{pqkl} \\
Q_{ij} &= C^e_{ijkl} C_{klmn}\frac{\partial f_p}{\partial T'_{mn}}\frac{1}{1+\xi'}\Phi_t
\end{aligned}
\tag{2.109}
$$

Then, substituting Equation (2.109) into Equation (2.108) yields

$$
\hat{T}'_{ij} = C^{\tan}_{ijkl} D_{kl} - C^e_{ijkl} C_{klmn}\frac{\partial f_p}{\partial T'_{mn}}\frac{1}{1+\xi'}\Phi_t
\tag{2.110}
$$

2.3.4 Conservation of Mass

2.3.4.1 Continuity equation for water and air

The conservation of mass is given in the following equation as

$$
\frac{\partial}{\partial t}(n^{\alpha}\rho_{\alpha}) + (n^{\alpha}\rho_{\alpha}v^{\alpha}_i)_{,i} = 0 \qquad \alpha = (\mathrm{S}, \mathrm{W}, \mathrm{G})
\tag{2.111}
$$

The conservation law for the solid, liquid, and gas phases are expressed as

S: $$\dot{n}^S \rho_S + n^S \dot{\rho}_S + (n^S)_{,i} \rho_S v_i^S + n^S (\rho_S)_{,i} v_i^S + n^S \rho_S v_{i,i}^S = 0 \tag{2.112}$$

W: $$\dot{n}^W \rho_W + n^W \dot{\rho}_W + (n^W)_{,i} \rho_W v_i^W + n^W (\rho_W)_{,i} v_i^W + n^W \rho_W v_{i,i}^W = 0 \tag{2.113}$$

G: $$\dot{n}^G \rho_G + n^G \dot{\rho}_G + (n^G)_{,i} \rho_G v_i^G + n^G (\rho_G)_{,i} v_i^G + n^G \rho_G v_{i,i}^G = 0 \tag{2.114}$$

Considering the fact that the space derivatives of volume fraction n^α and the material density ρ_α are negligible, and assuming that the soil skeleton and water are incompressible, namely, $\dot{\rho}_S$=0, $\dot{\rho}_{\mathrm{W}}$=0, the conservation law for each phases can be expressed with degree of saturation s and the volume fraction of void n, in other words,

S: $$-\dot{n}\rho_S + (1-n)\rho_S v_{i,i}^S = 0 \tag{2.115}$$

W: $$\dot{n}\, s\, \rho_W + n\, \dot{s}\, \rho_W + n\, s\, \rho_W\, v_{i,i}^W = 0 \tag{2.116}$$

G: $$(1-s)\,\dot{n}\,\rho_G - n\,\dot{s}\,\rho_G + n\,(1-s)\,\dot{\rho}_G + n\,(1-s)\,\rho_G\, v_{i,i}^G = 0 \tag{2.117}$$

Multiplying both sides of Equation (2.115) by $s\,\dfrac{\rho_W}{\rho_S}$ yields

$$-\dot{n}\, s\, \rho_W + (1-s)\, s\, \rho_W\, v_{i,i}^S = 0 \tag{2.118}$$

Adding both sides of Equation (2.116) and Equation (2.118) and then dividing by ρ_W, we get

$$n\dot{s} + s v_{i,i}^S + ns\left(v_i^W - v_i^S\right)_{,i} = 0 \tag{2.119}$$

Substituting Equation (2.63) and apparent velocity V_i^W in Equation (2.36) into Equation (2.119), the conservation law for water can finally be defined as

$$s\, D_{ii} + \dot{s}\, n = -V_{i,i}^W \tag{2.120}$$

Next, the conservation law for gas is obtained from Equations (2.115) and (2.117). By multiplying both sides of Equation (2.115) by $(1-s)\dfrac{\rho_G}{\rho_S}$ yields

$$-\dot{n}(1-s)\rho_G + (1-n)(1-s)\,\rho_G\, v^S_{i,i} = 0 \tag{2.121}$$

Adding both sides of Equation (2.118) and Equation (2.119) and then dividing by ρ_G, we get

$$-n\,\dot{s} + n(1-s)\frac{\dot{\rho}_G}{\rho_G} + (1-s)v^S_{i,i} + n\,(1-s)\,(v^G_i - v^S_i)_{,i} = 0 \tag{2.122}$$

Substituting Equation (2.63) and apparent velocity V^G_i in Equation (2.37) into Equation (2.122), the conservation law for gas can be finally be defined as

$$(1-s)D_{ii} - \dot{s}n + (1-s)\,n\,\frac{\dot{\rho}_G}{\rho_G} = -V^G_{i,i} \tag{2.123}$$

2.3.4.2 Weak form of the continuity equation for the liquid phase

The boundary conditions for the discretization for the continuity equation of liquid phase are given by

$$P^{\mathrm{W}} = \overline{P}^{\mathrm{W}} \qquad \text{on} \quad \partial D^W_P \tag{2.124}$$

$$V^{\mathrm{W}} = \overline{V}^{\mathrm{W}} \qquad \text{on} \quad \partial D^W_q \tag{2.125}$$

As Fig. 2.5 shows, $\overline{P}^{\mathrm{W}}$ is the water pressure applied on the pressure boundary ∂D^W_P, and $\overline{q}^{\mathrm{W}}$ is the velocity of the water through the boundary surface ∂D^W_q. It is obvious that ∂D^W_P and ∂D^W_q are the parts of the closed boundary ∂D, which satisfies the following relations:

$$\partial D^W_P \cup \partial D^W_q = \partial D \quad \text{and} \quad \partial D^W_P \cap \partial D^W_q = 0 \tag{2.126}$$

From Equation (2.120), the weak form of the continuity equation for water is given as

$$\int_D (V_{i,i}^{\mathrm{W}} + sD_{ii} + \dot{s}n)\,\delta u_{\mathrm{W}}\,dV = 0 \tag{2.127}$$

where δu_{W} is the test function for the pore water pressure.

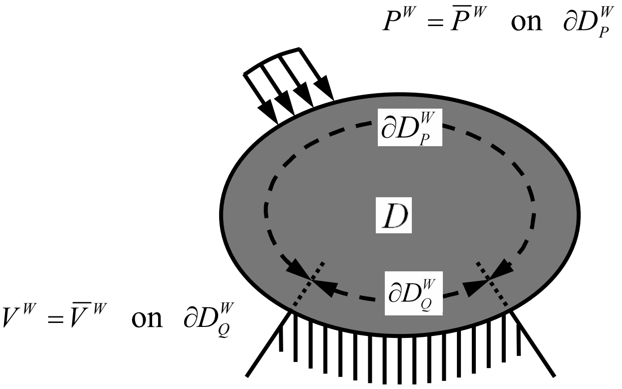

$P^W = \overline{P}^W$ on ∂D_P^W
∂D_P^W
D
∂D_Q^W
$V^W = \overline{V}^W$ on ∂D_Q^W

Figure 2.5 Boundary conditions for the liquid phase

Employing the relation

$$V_{i,i}^{\mathrm{W}}\delta u_{\mathrm{W}} = (V_i^{\mathrm{W}}\delta u_{\mathrm{W}})_{,i} - V_i^{\mathrm{W}}\delta u_{\mathrm{W},i} \tag{2.128}$$

and applying the Gauss theorem, Equation (2.127) can be rewritten as

$$-\int_D \delta u_{\mathrm{W},i}V_i^{\mathrm{W}}dV + \int_D \delta u_{\mathrm{W}}sD_{ii}dV + \int_D \delta u_{\mathrm{W}}n\dot{s}dV + \int_{\partial D_q^{\mathrm{W}}} \delta u_{\mathrm{W}}\overline{V}_i^{\mathrm{W}}n_i dS = 0 \tag{2.129}$$

Considering the fact that degree of saturation, s, is the single-variation function of suction, P^C, $\dot{s}$ can be given as

$$\dot{s} = \frac{\partial s}{\partial P^C}\frac{\partial P^C}{\partial t} = \frac{\partial s}{\partial P^C}(\dot{P}^{\mathrm{G}} - \dot{P}^{\mathrm{W}}) \tag{2.130}$$

Substituting Equations (2.38) and (2.130) into Equation (2.129) yields

$$\begin{aligned} -\int_D \delta u_{\mathrm{W},i}\frac{k^{\mathrm{W}}}{\gamma^{\mathrm{W}}}(P_{,i}^{\mathrm{W}} + \rho_W\overline{F})\,dV + \int_D \delta u_{\mathrm{W}}\,sD_{ii}\,dV + \int_D \delta u_{\mathrm{W}}\,n\frac{\partial s}{\partial P^C}(\dot{P}^{\mathrm{G}} - \dot{P}^{\mathrm{W}})\,dV \\ + \int_{\partial D_q^{\mathrm{W}}} \delta u_{\mathrm{W}}\,\overline{V}_i^{\mathrm{W}}\,n_i\,dS = 0 \end{aligned} \tag{2.131}$$

Incorporating Equations (2.76), (2.77), (2.78) into Equation (2.131), we obtain

$$\begin{aligned}
&-\int_D \left\{\delta u_{\mathrm{W}}^*\right\}^T [B_h]^T \frac{k^{\mathrm{W}}}{\gamma^{\mathrm{W}}} [B_h]\left\{P^{\mathrm{W}*}\right\} dV - \int_D \left\{\delta u_{\mathrm{W}}^*\right\}^T [B_h]^T \frac{k^{\mathrm{W}}}{\gamma^{\mathrm{W}}} \rho_W \left\{\overline{F}\right\} dV \\
&\quad + \int_D \left\{\delta u_{\mathrm{W}}^*\right\}^T \left\{N_h\right\}^T s \left\{B_v\right\}^T \left\{v^*\right\} dV + \int_D \left\{\delta u_{\mathrm{W}}^*\right\}^T \left\{N_h\right\}^T n \frac{\partial s}{\partial P^C} [N_h]\left(\left\{\dot{P}^{\mathrm{G}*}\right\} - \left\{\dot{P}^{\mathrm{W}*}\right\}\right) dV \\
&\quad + \int_{\partial D_q^{\mathrm{W}}} \left\{\delta u_{\mathrm{W}}^*\right\}^T \left\{N_h\right\}^T \left\{n\right\}^T \left\{\overline{V}^{\mathrm{W}}\right\} dS = 0
\end{aligned} \tag{2.132}$$

Taking the arbitration of the test function and dividing both sides of the previous equation by $\left\{ \delta u_{\mathrm{W}}^* \right\}$ gives

$$\begin{aligned}
&-\int_D [N_h]^T s \left\{B_v\right\}^T \left\{v^*\right\} dV + \frac{k^{\mathrm{W}}}{\gamma^{\mathrm{W}}} \int_D [B_h]^T [B_h]\left\{P^{\mathrm{W}*}\right\} dV \\
&\quad + \int_D \left\{N_h\right\}^T n \frac{\partial s}{\partial P^C} [N_h]\left\{\dot{P}^{\mathrm{W}*}\right\} dV - \int_D \left\{N_h\right\}^T n \frac{\partial s}{\partial P^C} \left\{N_h\right\}\left\{\dot{P}^{\mathrm{G}*}\right\} dV \\
&= \int_{\partial D_q^{\mathrm{W}}} \left\{N_h\right\}^T \left\{n\right\}^T \left\{\overline{V}^{\mathrm{W}}\right\} dS - \frac{k^{\mathrm{W}}}{\gamma^{\mathrm{W}}} \int_D [B_h]^T \rho^{\mathrm{W}} \left\{\overline{F}\right\} dV
\end{aligned} \tag{2.133}$$

The discretization of the continuity equation for the liquid phase is obtained as

$$\begin{aligned}
&- s[K_v]\left\{v^*\right\} + \frac{k^{\mathrm{W}}}{\gamma^{\mathrm{W}}} [K_h]\left\{P^{\mathrm{W}*}\right\} + n \frac{\partial s}{\partial P^C} [K_n]\left\{\dot{P}^{\mathrm{W}*}\right\} - n \frac{\partial s}{\partial P^C} [K_n]\left\{\dot{P}^{\mathrm{G}*}\right\} \\
&\quad = \left\{V^{\mathrm{W}}\right\} + \left\{F^{\mathrm{W}}\right\}
\end{aligned} \tag{2.134}$$

where

$$[K_v] = \int_D \left\{B_v\right\}\left\{N_h\right\} dV \tag{2.135}$$

$$[K_h] = \int_D \left\{B_h\right\}^T \left\{B_h\right\} dV \tag{2.136}$$

$$[K_n] = \int_D \left\{N_h\right\}^T \left\{N_h\right\} dV \tag{2.137}$$

$$\left\{V^{\mathrm{W}}\right\} = \int_{\partial D_q^{\mathrm{W}}} \left\{N_h\right\}^T \left\{n\right\}^T \left\{\overline{V}^{\mathrm{W}}\right\} dS \tag{2.138}$$

$$\left\{F^{\mathrm{W}}\right\}=-\frac{k^{W}}{\gamma^{W}}\int_{D}\left\{B_{h}\right\}^{T}\rho^{\mathrm{W}}\left\{\overline{F}\right\}dV \tag{2.139}$$

Substituting the Euler's approximation Equation (2.89) and Equation (2.90) into the Equation (2.134), the final discretization equation for the continuity equation for the liquid phase is obtained as

$$\begin{aligned}&-s\left[K_{v}\right]\left\{\Delta u^{*}\right\}+\Delta t\frac{k^{\mathrm{W}}}{\gamma^{\mathrm{W}}}\left[K_{h}\right]\left\{P^{\mathrm{W}*}\right\}_{t+\Delta t}+n\frac{\partial s}{\partial P^{C}}\left[K_{n}\right]\left\{P^{\mathrm{W}*}\right\}_{t+\Delta t}\\&-n\frac{\partial s}{\partial P^{C}}\left[K_{n}\right]\left\{P^{\mathrm{G}*}\right\}_{t+\Delta t}=\Delta t\left(\left\{V^{\mathrm{W}}\right\}+\left\{F^{\mathrm{W}}\right\}\right)\end{aligned} \tag{2.140}$$

2.3.4.3 Weak form of the continuity equation for the gas phase

The boundary conditions for the discretization of the continuity equation for the gas phase are given by

$$P^{\mathrm{G}}=\overline{P}^{\mathrm{G}} \quad \text{on} \quad \partial D_{P}^{G} \tag{2.141}$$

$$V^{\mathrm{G}}=\overline{V}^{\mathrm{G}} \quad \text{on} \quad \partial D_{q}^{G} \tag{2.142}$$

As Fig 2.6 shows, $\overline{P}^{\mathrm{G}}$ is the air pressure applied on the boundary ∂D_{P}^{G}, and $\overline{q}^{\mathrm{G}}$ is the velocity of the air through the boundary surface ∂D_{q}^{G}. It is obvious that $\partial D_{P}^{\mathrm{G}}$ and $\partial D_{q}^{\mathrm{G}}$ are the parts of the closed boundary ∂D, which satisfies the following relations:

$$\partial D_{P}^{G}\bigcup\partial D_{q}^{G}=\partial D \quad \text{and} \quad \partial D_{P}^{G}\bigcap\partial D_{q}^{G}=0 \tag{2.143}$$

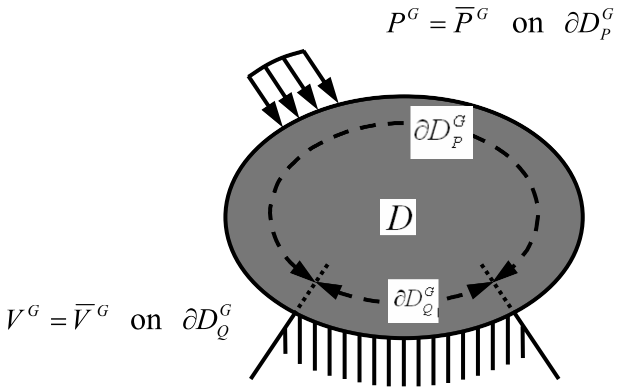
$P^{G}=\overline{P}^{G}$ on ∂D_{P}^{G}
∂D_{P}^{G}
D
∂D_{Q}^{G}
$V^{G}=\overline{V}^{G}$ on ∂D_{Q}^{G}

Figure 2.6 Boundary conditions for the gas phase

From Equation (2.123), the weak form of the continuity equation for the gas phase is given as

$$\int_D \left((1-s)D_{ii} - \dot{s}\, n + (1-s)n \frac{\dot{\rho}_G}{\rho_G} + V_{i,i}^G \right) \delta u_{\mathrm{G}}\, dV = 0 \tag{2.144}$$

where δu_{G} is the test function for the pore air pressure.

Employing the relation

$$V_{i,i}^G \delta u_{\mathrm{G}} = (V_i^G \delta u_{\mathrm{G}})_{,i} - V_i^G\, \delta u_{\mathrm{G},i} \tag{2.145}$$

Applying the Gauss theorem, Equation (2.144) can be rewritten as

$$\begin{aligned} &\int_D \delta u_{\mathrm{G}} (1-s)\, D_{ii} dV - \int_D \delta u_{\mathrm{G}}\, \dot{s}\, n\, dV + \int_D \delta u_{\mathrm{G}} (1-s)\, n \frac{\dot{\rho}_G}{\rho_G} dV \\ &+ \int_{\partial D_q^G} \delta u_{\mathrm{G}}\, \overline{V}_i^G n_i\, dS - \int_D \delta u_{\mathrm{G,i}}\, V_i\, dV = 0 \end{aligned} \tag{2.146}$$

Substituting Equation (2.130) into Equation (2.146) yields

$$\begin{aligned} &\int_D \delta u_{\mathrm{G}} (1-s) D_{ii}\, dV - \int_D \delta u_{\mathrm{G}}\, n\, \frac{\partial s}{\partial P^C} (\dot{P}^{\mathrm{G}} - \dot{P}^{\mathrm{W}})\, dV + \int_D \delta u_{\mathrm{G}}\, (1-s)\, n \frac{\dot{\rho}_G}{\rho_G}\, dV \\ &- \int_D \delta u_{\mathrm{G,i}}\, V_i\, dV + \int_{\partial D_q^G} \delta u_{\mathrm{G}}\, \overline{V}_i^G\, n_i\, dS = 0 \end{aligned} \tag{2.147}$$

To describe the changes in gas density, the equation for ideal gases is used as

$$\rho_G = \frac{M(-P^{\mathrm{G}})}{R\theta} = -\frac{MP^{\mathrm{G}}}{R\theta} \tag{2.148}$$

$$\dot{\rho}_G == -\frac{M}{R} \left(\frac{\dot{P}^{\mathrm{G}}}{\theta} - \frac{P^{\mathrm{G}} \dot{\theta}}{\theta^2} \right) \tag{2.149}$$

in which M is the molecular weight of gas, R is the gas constant, θ is the temperature, and tension is positive in the equations.

Dividing Equation (2.149) by Equation (2.148) yields

$$\frac{\dot{\rho}_G}{\rho_G} = \frac{\dot{P}^{\mathrm{G}}}{P^{\mathrm{G}}} - \frac{\dot{\theta}}{\theta} \tag{2.150}$$

In this analysis, the temperature is assumed to be constant, namely, $\dot{\theta} = 0$. Equation (2.150) becomes

$$\frac{\dot{\rho}_G}{\rho_G} = \frac{\dot{P}^{\mathrm{G}}}{P^{\mathrm{G}}} \tag{2.151}$$

Substituting Equation (2.157) and (2.151) into Equation (2.147) yields

$$\begin{aligned} & -\int_D \delta u_{G,i} \frac{k^G}{\rho_G g} (P^G_{,i})\, dV + \int_D \delta u_G (1-s) D_{ii}\, dV - \int_D \delta u_G \frac{\partial s}{\partial P^C} (\dot{P}^G - \dot{P}^W)\, dV \\ & \quad + \int_D \delta u_G (1-s)\, n\, \frac{\dot{P}^G}{P^G} dV + \int_{\partial D_q^G} \delta u_G\, \overline{V}_i^G\, n_i\, dS = 0 \end{aligned} \tag{2.152}$$

Incorporating Equations (2.76), (2.77), (2.78) into Equation (2.152), we have

$$\begin{aligned} & -\int_D \left\{\delta u_{\mathrm{G}}^*\right\}^T [B_h]^T \frac{k^G}{\rho_G g} [B_h] \left\{P^{\mathrm{G}*}\right\} dV + \int_D \left\{\delta u_{\mathrm{G}}^*\right\}^T \{N_h\}^T (1-s) \{B_v\}^T \left\{v^*\right\} dV \\ & -\int_D \left\{\delta u_{\mathrm{G}}^*\right\}^T \{N_h\}^T n\, \frac{\partial s}{\partial P^C} \{N_h\} (\dot{P}^G - \dot{P}^W)\, dV \\ & +\int_D \left\{\delta u_{\mathrm{G}}^*\right\}^T \{N_h\}^T (1-s)\, n \frac{\{N_h\}\left\{\dot{P}^{G*}\right\}}{\overline{P}_m^G} dV + \int_{\partial D_q^G} \left\{\delta u_{\mathrm{G}}^*\right\}^T \{N_h\}^T \{n\}^T \left\{\overline{V}^{\mathrm{G}}\right\} dS = 0 \end{aligned} \tag{2.153}$$

where $\overline{P}_m^G$ is the average pore air pressure in *D*. Taking the arbitration of the test function and dividing both sides of the previous equation by $\left\{\delta u_{\mathrm{W}}^*\right\}$ gives

$$\begin{aligned} & -\int_D [B_h]^T \frac{k^G}{\rho_G g} [B_h] \left\{P^{\mathrm{G}*}\right\} dV + \int_D \{N_h\}^T (1-s) \{B_v\}^T \left\{v^*\right\} dV \\ & -\int_D \{N_h\}^T n \frac{\partial s}{\partial P^C} \{N_h\} (\dot{P}^G - \dot{P}^W)\, dV + \int_D \{N_h\}^T (1-s) n \frac{\{N_h\}\left\{\dot{P}^{G*}\right\}}{\overline{P}_m^G} dV \\ & + \int_{\partial D_q^G} \{N_h\}^T \{n\}^T \left\{\overline{V}^{\mathrm{G}}\right\} dS = 0 \end{aligned} \tag{2.154}$$

The discretization of the continuity equation for the liquid phase is obtained as

$$
\begin{aligned}
&-(1-s)\left[K_v\right]^T\left\{v^*\right\}+\frac{k^{\mathrm{G}}}{\rho_G g}\left[K_h\right]\left\{P^{\mathrm{G}*}\right\}-n\frac{\partial s}{\partial P^C}\left[K_n\right]\left\{\dot{P}^{\mathrm{W}*}\right\}+n\frac{\partial s}{\partial P^C}\left[K_n\right]\left\{\dot{P}^{\mathrm{G}*}\right\}\\
&\quad-(1-s)\,n\left[K_c^P\right]\left\{P^{\mathrm{G}*}\right\}=\left\{V^{\mathrm{G}}\right\}+\left\{F^{\mathrm{G}}\right\}
\end{aligned}
\tag{2.155}
$$

where

$$\left[K_v\right]=\int_D\left\{B_v\right\}\left\{N_h\right\}dV \tag{2.156}$$

$$\left[K_h\right]=\int_D\left\{B_h\right\}^T\left\{B_h\right\}dV \tag{2.157}$$

$$\left[K_n\right]=\int_D\left\{N_h\right\}^T\left\{N_h\right\}dV \tag{2.158}$$

$$\left[K_c^p\right]=\int_D\frac{\left\{N_h\right\}\left\{\dot{P}^{G*}\right\}}{\overline{P}_m^G}\,dV \tag{2.159}$$

$$\left\{V^{\mathrm{G}}\right\}=\int_{\partial D_q^{\mathrm{G}}}\left\{N_h\right\}^T\left\{n\right\}^T\left\{\overline{V}^{\mathrm{G}}\right\}dS \tag{2.160}$$

$$\left\{F^G\right\}=0 \tag{2.161}$$

Substituting the Euler's approximation in Equation (2.89) and Equation (2.90) into the Equation (2.155), the final discretization equation for the continuity equation of the gas phase is obtained as

$$
\begin{aligned}
&-(1-s)\left[K_v\right]^T\left\{\Delta u^*\right\}+\Delta t\frac{k^{\mathrm{G}}}{\rho^{\mathrm{G}}g}\left[K_h\right]\left\{P^{\mathrm{G}*}\right\}_{t+\Delta t}-n\frac{\partial s}{\partial P^C}\left[K_n\right]\left\{\dot{P}^{\mathrm{W}*}\right\}_{t+\Delta t}\\
&\quad+n\frac{\partial s}{\partial P^C}\left[K_n\right]\left\{P^{\mathrm{G}*}\right\}_{t+\Delta t}-(1-s)\,n\left[K_c^P\right]\left\{P^{\mathrm{G}*}\right\}_{t+\Delta t}\\
&\quad=\Delta t\left(\left\{V^{\mathrm{G}}\right\}+\left\{F^{\mathrm{G}}\right\}\right)-n\frac{\partial s}{\partial P^C}\left[K_n\right]\left\{\dot{P}^{\mathrm{W}*}\right\}_t+n\frac{\partial s}{\partial P^C}\left[K_n\right]\left\{P^{\mathrm{G}*}\right\}_t\\
&\quad-(1-s)n\left[K_c^P\right]\left\{P^{\mathrm{G}*}\right\}_t
\end{aligned}
\tag{2.162}
$$

2.3.5 Discretized Governing Equations for the Multiphase Finite Element Analysis

Combining the discretization of the equilibrium equation (2.91) and the continuity equations for the liquid phase (2.140) and the gas phase (2.162) gives the governing equation for the multiphase finite element formulation as

$$\left(\Delta t\left[K_1\right]+\left[K_2\right]\right)\left\{\mathrm{X}\right\}_{t+\Delta t}=\Delta t\left(\left\{\mathrm{F}\right\}+\left\{\mathrm{V}\right\}\right)+\left[K_2\right]\left\{\overline{\mathrm{X}}\right\}_t \tag{2.163}$$

in which $\left\{\mathrm{X}\right\}_{t+\Delta t}$ and $\left\{\mathrm{X}\right\}_t$ are unknown values at time $t+\Delta t$, and at the last step, respectively, which are defined as

$$\left\{\mathrm{X}\right\}_{t+\Delta t}=\begin{Bmatrix}\left\{\Delta u^*\right\}\\ \left\{P^{W*}\right\}_{t+\Delta t}\\ \left\{P^{G*}\right\}_{t+\Delta t}\end{Bmatrix}\ ,\ \left\{\mathrm{X}\right\}_t=\begin{Bmatrix}\left\{0\right\}\\ \left\{P^{W*}\right\}_t\\ \left\{P^{G*}\right\}_t\end{Bmatrix} \tag{2.164}$$

where $\left[K_1\right]$ and $\left[K_2\right]$ in Equation (2.163) are given as

$$\left[K_1\right]=\begin{bmatrix}0 & 0 & 0\\ 0 & \Delta t\dfrac{k^W}{\rho_W g}\left[K_h\right] & 0\\ 0 & 0 & \Delta t\dfrac{k^G}{\rho_G g}\left[K_h\right]\end{bmatrix} \tag{2.165}$$

$$\left[K_2\right]=\begin{bmatrix}\left[K\right]+\left[K_L\right] & \left(-A_s+s\right)\left[K_v\right] & \left\{A_s+\left(1-s\right)\right\}\left[K_v\right]\\ -s\left[K_v\right]^T & n\dfrac{\partial s}{\partial P^C}\left[K_n\right] & -n\dfrac{\partial s}{\partial P^C}\left[K_n\right]\\ -\left(1-s\right)\left[K_v\right]^T & -n\dfrac{\partial s}{\partial P^C}\left[K_n\right] & n\dfrac{\partial s}{\partial P^C}\left[K_n\right]-n\left(1-s\right)\left[K_c^P\right]\end{bmatrix} \tag{2.166}$$

$\left\{\mathrm{F}\right\}$ and $\left\{\mathrm{V}\right\}$ in Equation (2.163) are given as

$$\left\{\mathrm{F}\right\}=\begin{Bmatrix}\left\{F\right\}\\ \left\{F^W\right\}\\ \left\{F^G\right\}\end{Bmatrix},\quad \left\{\mathrm{V}\right\}=\begin{Bmatrix}\left\{V\right\}\\ \left\{V^W\right\}\\ \left\{V^G\right\}\end{Bmatrix} \tag{2.167}$$

Chapter 3

THREE-DIMENSIONAL MULTIPHASE SIMULATION OF THE TRIAXIAL BEHAVIOR OF UNSATURATED SOIL

3.1 Introduction

Many laboratory tests and simulations have been conducted under conditions of constant air pressure conditions. However, drained conditions for water and air cannot always be attained in engineering problems. For example, the air pressure in river embankments increases during the seepage process and may vary during the soil compaction process. Yamamura (1971) indicated that air can become trapped in parts of embankments due to heavy rains or overflow. Since the air pressure changes under these partially drained conditions, it is necessary to conduct tests under undrained conditions for water and air (constant water content and air content) in order to accurately verify the numerical model for unsaturated soil under general boundary conditions. For this reason, triaxial tests on unsaturated silty under undrained and drained conditions for water and air have been conducted (Suzuki, 2006). In the tests, both the pore water pressure and the pore air pressure have been accurately measured.

Using the elasto-viscoplastic constitutive model for unsaturated soil and the multiphase formulations mentioned in Chapter 2, three-dimensional multiphase finite element simulations are carried out to simulate the triaxial behavior of unsaturated cylindrical specimens. The numerical simulations are divided into two parts. In the first part, simulations are conducted under drained conditions for water and air. The effect of suction, the strain rate, and the confining pressure are investigated. In the second part, triaxial tests under undrained conditions for water and air (constant water and constant air content) are simulated. The changes in pore air pressure, volumetric strain, and suction, etc. are reproduced.

3.2 Triaxial Compression Tests on Unsaturated Soil

The experimental results showing the changes of pore air pressure under undrained condition for water and air are occasionally reported. Most of the works conducted under controlled suction conditions were examined either under K_0 conditions with oedometers (Jennings & Burland, 1962; Fredlund & Morgenstern, 1976) or under isotropic stress conditions (Matyas & Radhakrishna, 1968). Some triaxial tests have also been performed by Fredlund (1982), Cui & Delage (1996), Wulfsohn, Adams & Fredlund (1998), and Blatz &Graham (2003). Most of these experiments, however, were conducted under constant pore air conditions. Very few types of compressive behavior, such as stress-strain curves and changes in pore air pressure and pore water pressure, and volumetric strain, under different levels of suction and confining pressures, have been reported.

A conventional triaxial apparatus for saturated soil was modified by Kim (2004) and Suzuki (2006) to test the compression behavior of unsaturated soil. Changes in the volume of the specimen during triaxial tests were evaluated by measuring the lateral displacements of the two sides of the specimen. It was possible to measure the pre water pressure and the pore air pressure accurately and to control them independently. Matric suction, mean skeleton stress and deviatoric stress can be monitored in a series of drained and undrained conditions for water and air tests.

3.2.1 Material Properties

The material used in the experiment was DL clay. The DL clay was classified as ML by the JUSCS (Japanese Unified Soil Classification System). The soil is thought to be non-plastic since the liquid limit is less than 50%. The clay and silt contents is 10% and 90%, respectively. The density of soil solid is ρ_s=2.65g/cm^3. The cylindrical specimens were prepared using compaction method. The compaction energy was controlled so that the initial void ratio would be around 1.1. All the specimen used in this experimental study are 50mm in diameter and 100mm in height.

3.2.2 Equipment and Testing Program

Figure 3.1 shows a schematic drawing of the triaxial cell used for testing. In order to separate the route for the measurements and to control of the pore-air pressure, a polyflon filter and a ceramic disc were used in the tests. The polyflon filter is placed on the top of the specimen to cut off the passing of water. The air pressure that passed through the polyflon filter was measured by a pressure gauge. The air pressure gauge was installed in the cap of the cell, which made the measurements more accurate. Pore water pressure is measured or controlled through a saturated fine ceramic disk integrated with a base pedestal connected to the measuring system. The matric suction in the specimen must not exceed the air entry value of the ceramic disk (200 kPa), or air will enter the water compartment which will become filled with air bubbles and no longer maintain continuity between the pore pressure and the water in the measuring system. Changes in volume during the triaxial tests were evaluated by measuring the lateral displacements of the two sides of the specimen with four proximity transducers. Aluminum foil was used as a target for the proximity transducers. The main advantage of this method is that changes in volume can be obtained without any contact with the specimen.

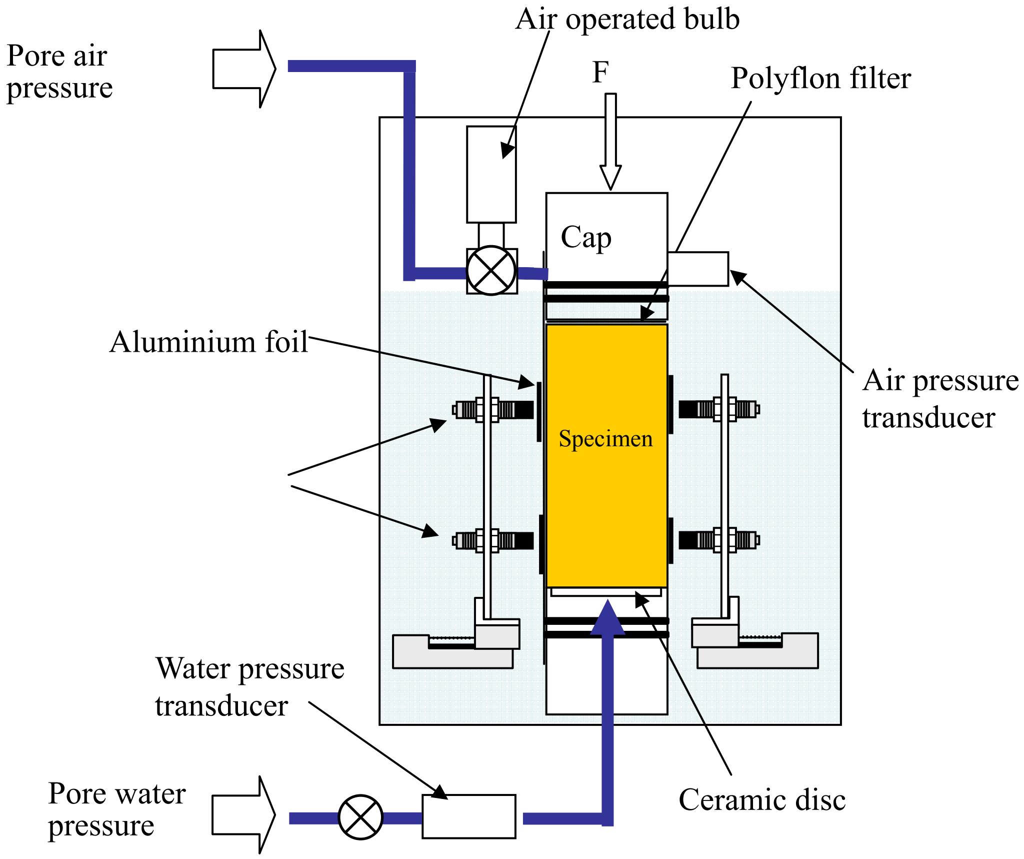
Air operated bulb
Pore air pressure
F
Polyflon filter
Cap
Aluminium foil
Air pressure transducer
Specimen
Water pressure transducer
Pore water pressure
Ceramic disc

Figure 3.1 Schematic drawing of the triaxial cell used to test the unsaturated soil

Since the pore air pressure and the pore water pressure can be controlled under different drainage conditions during shearing, various tests have been performed by Suzuki (2006). Tests under drained conditions for water and air were performed with allowing the air and water flowing in or out. Tests under undrained conditions for water and air were carried out in case that no air and water can flow in or out during shearing. In the experiments, the effects of initial suction, the strain rate, and the confining pressure were investigated.

3.3 Numerical Simulations

Using a three-dimensional air-water-soil coupled finite element code, the triaxial behaviors of unsaturated soil are simulated. A comprehensive numerical investigation has been carried out for the triaxial compressive behaviuor of unsaturated silty.

3.3.1 Geometry and Boundary conditions

The element types used in the three-dimensional analysis are shown in Figure 3.2. A twenty-node isoparametric element with a reduced Gaussian (2×2×2) integration was applied for the soil skeleton and an eight-node isoparametric element with a full (2×2×2) integration was applied for the pore water pressure and the pore air pressure.

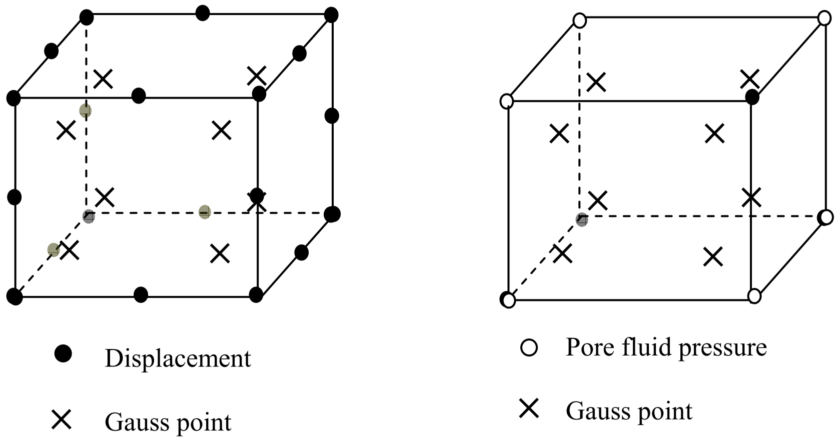

Figure 3.2 Isoparametric elements used in the three-dimensional finite element method

Figure. 3.3 shows the finite element mesh and the boundary conditions for the analysis, which is 1/4 of the specimen. A constant axial (z-direction) displacement with a given rate (0.5%/min, 0.05%/min) was applied to the nodes on the top surface. In the analysis under undrained conditions for water and aie (constant water and constant air content), all boundaries were assumed to be impermeable. In the analysis under drained conditions for water and air (constant water pressure and air pressure), air was exhausted only from the top surface, while water drainage was permitted only from the bottom boundary.

Furthermore, the horizontal deformation was constrained at both top and bottom boundaries. As the figure shows, the center of the sample was meshed as a surface.

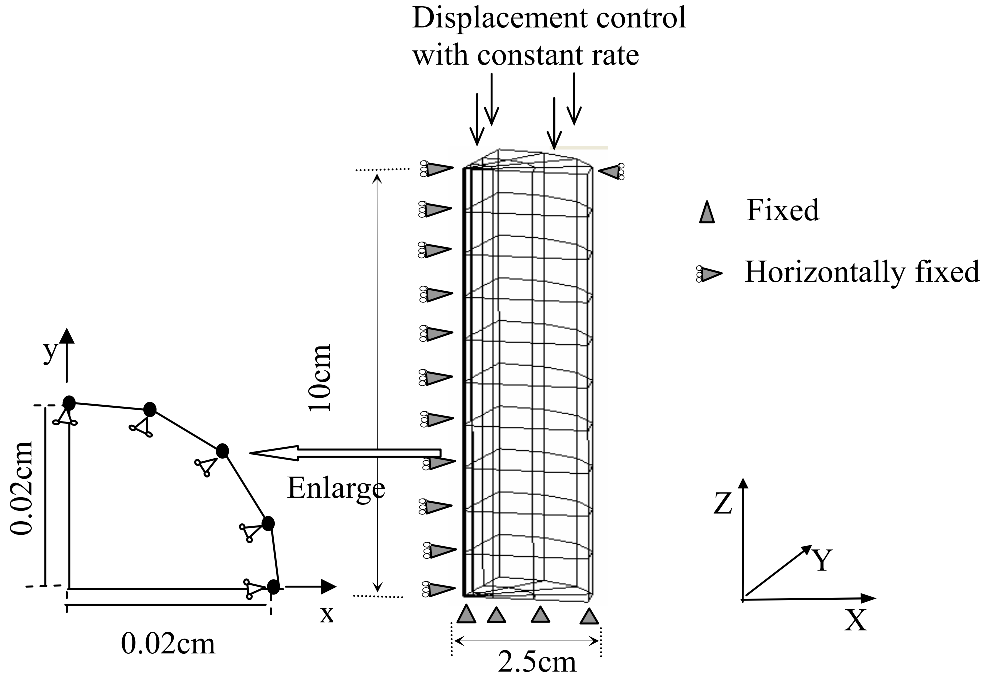

Figure 3.3 Finite element mesh and boundary conditions

3.3.2 Determination of the Material Parameters

All together, there are twenty two material parameters are required by in present analysis. Fourteen parameters are adopted to describe the elasto-viscoplastic constitutive model. They are compression index λ, swelling index κ, initial void ratio e_0, elastic shear modulus G_0, initial yield stress σ'_{mbi}, stress ratio at maximum compression M^*_m, viscoplasitc parameter m, viscoplastic parameter C_1 and C_2, structure parameter $\sigma'_{\max}$ and β, reference suction P_i^C, and suction effect parameter S_I and s_d.

Compression index λ and swelling index κ are given by the slope of the isotropic consolidation and swelling tests, respectively. The triaxial isotropic consolidation tests were carried out with suction equals to 50 kPa. The increase/ decrease rate of cell pressure is 27 kPa /hour. We determine λ to be 0.114 and κ to be 0.0102 from the following equation,

$$\lambda = -\frac{\Delta e_1}{\Delta(\ln \sigma'_{m1})}, \quad \kappa = -\frac{\Delta e_2}{\Delta(\ln \sigma'_{m2})} \tag{3.1}$$

where σ'_{m1} and σ'_{m2} are mean skeleton stress under consolidation tests and swelling tests, respectively.

Elastic shear modulus G_0 is determined by the initial slope of the undrained triaxial compression tests, namely,

$$G_0 = \frac{1}{3}\frac{\Delta q}{\Delta \varepsilon_{11}} \tag{3.2}$$

where Δq is the increment in deviator stress and $\Delta \varepsilon_{11}$ is the increment in deviator stress. In this study, $\Delta \varepsilon_{11}$ was determined to be 0.01%.

Initial yield stress σ'_{mbi} is assumed to be the precosolidation stress. In present study, the specimens are normally consolidated, therefore, σ'_{mbi} is determined from the initial mean skeleton stress, σ'_{me}. The stress ratio at maximum compression M^*_m is defined by the value of $\eta^* = \sqrt{\eta^*_{ij}\eta^*_{ij}}$ when the volumeric strain increment changes from compression to swelling. Herein, M^*_m is determined from

$$M^*_m = \sqrt{\frac{2}{3}} M_m \tag{3.3}$$

where M_m is the slope of the critical state obtained from the tiaxial tests. Here we obtain M_m value of 1.23, therefore M^*_m is given as 1.00.

Viscoplastic parameters m' can be determined from the undrained triaxial tests for saturated silt with different strain rates. From Eq. (2.33), Viscoplastic deviatoric strain rate $\dot{e}^{vp}_{11}$ in triaxial stress state is obtained as

$$\dot{e}^{vp}_{11} = \sqrt{\frac{2}{3}} C_1 \exp\left\{ m' \left(\sqrt{\frac{2}{3}} \frac{q}{\sigma'_m} + \tilde{M}^* \ln \frac{\sigma'_m}{\sigma'_{mb}} \right) \right\} \tag{3.4}$$

Considering the undrained conditions, and assuming the elastic strain rate is negligible under, we obtain $\dot{e}^{vp}_{11} = \dot{\varepsilon}_{11}$. When undrained triaxial tests with different strain rates $\dot{\varepsilon}^{(1)}_{11}$ and $\dot{\varepsilon}^{(2)}_{11}$ are performed, the following equations are obtained at the point where the mean effective stress takes the same value, $\sigma'^{(0)}_m$, in the stress path.

$$\frac{\dot{\varepsilon}^{(1)}_{11}}{\dot{\varepsilon}^{(2)}_{11}} = \exp\left\{ m' \sqrt{\frac{2}{3}} \left\{ \left(\frac{q}{\sigma'_m}\right)^{(1)} - \left(\frac{q}{\sigma'_m}\right)^{(2)} \right\} \right\} \tag{3.5}$$

$$m' = \sqrt{\frac{2}{3}} \frac{\ln \dot{\varepsilon}_{11}^{(1)} - \ln \dot{\varepsilon}_{11}^{(2)}}{(\frac{q}{\sigma_m'})^{(1)} - (\frac{q}{\sigma_m'})^{(2)}} \tag{3.6}$$

The viscoplastic parameter C_1 and C_2 are determined from the deviatoric stress- axial strain curve and the volumetric strain- axial strain curve by parametric study.

Structure parameter σ_{maf}' and can be obtained by the deviator stress at the residual stress state, while β, which dominates the decreasing rate of deviator stress, is determined by the curve fitting. Due to the specimens are reconstituted for these tests, σ_{maf}' is set to be equal to initial mean skeleton stress, and β is set to be zero.

Suction effect parameters S_I, S_d are determined by curve fitting method.

Eight parameters are adopted to describe the hydraulic property of unsaturated soil. They are parameter for SWCC: α, n, $s_{\max}$, and $s_{\min}$, permeability of water at saturated condition k^W, permeability of gas at fully dry condition k^G, shape parameter a and b for permeability and saturation relation. The determination of parameter for SWCC are based the measured saturation and suction relation at initial states of specimens, as shown in Fig. 3.4. The permeability of water and air and shape parameter can be ditermined from the steady-state method.

The main material parameters and the initial conditions used in the analysis are listed in Table 3.1

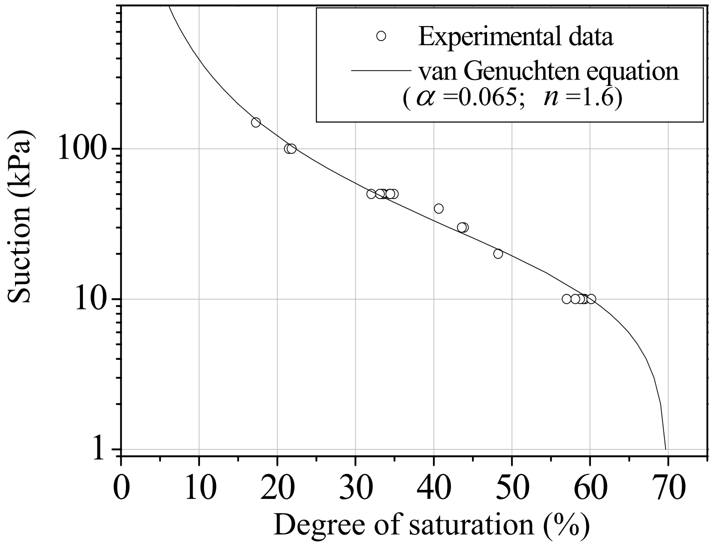

Figure 3.4 The soil water characteristic curve

Table 3.1 Material parameters and initial conditions

Initial void ratio e_0	1.07
Elastic shear modulus G_0 (GPa)	45.1
Consolidation yield stress σ'_{mbi} (kPa)	200
Swelling index κ	0.0102
Compression index λ	0.114
Viscoplastic parameter m'	52
Viscoplastic parameter C_1(1/s)	1.0×10^{-11}
Viscoplastic parameter C_2(1/s)	1.5×10^{-11}
Stress ratio at critical state M^*_m	1.23
Structural parameter σ'_{maf} (kPa)	200
Structural parameter β	0.0
Reference suction P_i^C (kPa)	100
Suction parameter S_I	0.5
Suction parameter S_d	0.25
Parameter α (1/kPa)	0.065
Parameter n	1.6
Permeability of water at s=1 k^W (m/s)	1.0×10^{-6}
Permeability of gas at s=0 k^G (m/s)	1.0×10^{-5}
Shape parameter a	3.0
Shape parameter b	2.3
Saturation (Max) s_{max}	0.7
Saturation (Min) s_{min}	0

3.4 Simulation Results

3.4.1 Simulation of the Drained Tests

Here, drained conditions for water and air means that specimens are sheared under conditions that water pressure at the bottom boundary and the air pressure at the top boundary remain constant. Since the change of suction during compression for the drained tests are very small, therefore, the suction effect on the soil skeleton can be clearly illustrated.

In the present model, suction has been incorprated into the model to reflect the collapse behavior, which is expressed as the shrinkage of the overconsolidation boundary surface and the static yield surface. In this section, to investigate suction effects on compressive behavior of unsaturated soil, predictions with different initial suction, that is, 0, 30, 50, 100 kPa, were compared against the experimental results. In addition, the effects of the confining pressure and the strain rate on tiaixial compression behaviors are also investigated. Typical behaviors of unsaturated soil under drained conditions, such as the stress path, the shear strength and the changes in volumetric strain is presented. The patterns of the analysis are listed in Table 3.2. The other initial values and material parameters are listed in Table 3.1.

Table 3.2 Simulated cases

	Initial suction (kPa)	Strain rate (%/min)	Confining pressure (kPa)
Initial suction effect	0, 30, 50, 100	0.5	200
Strain rate effect	50	0.5, 0.05	200
Confining pressure effect	50	0.5	100

3.4.1.1 Effect of initial suction on triaxial drained behavior

Firstly, simulations under different levels of initial suction were carried out. In the computations, the axial strain rate was assumed to be 0.5%/min, the increment for each step was 0.48, and the increment for the average strain per step was determined to be $\Delta\varepsilon_{zz} = 0.004\%$.

Figures 3.5 and 3.6 provides the skeleton stress paths and the stress-strain curves with different levels of initial suctions by simulations. From the stress-strain curves, it can be clearly observed that the larger the initial suction values, the higher the value of skeleton strength. This agrees with the experimental results under the same conditions. From these results, it is found that by introducing the suction effect into the constitutive model, present constitutive model can successfully reflect the suction effect on the strength of unsaturated soil.

The changes in volumetric strain with compression under different levels of initial suction are shown in Figure 3.7. Both the simulated and the experimental results show that higher initial suction case leads to small volumetric strain. It can be found that the stiffness of the soil skeletion become larger in case the high initial suction were adopted.

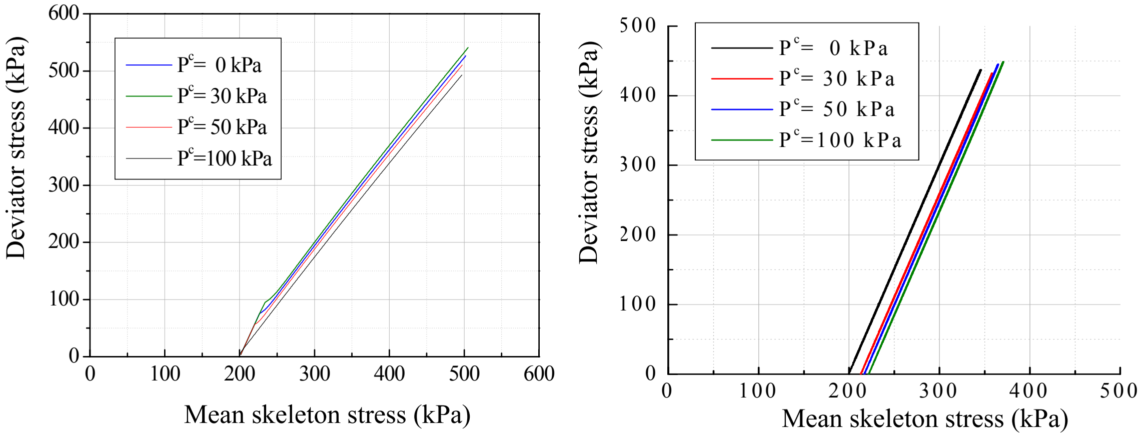

(a) (b)

Figure 3.5 Stress paths with different levels of initial suction: (a) simulated results and (b) experimental results

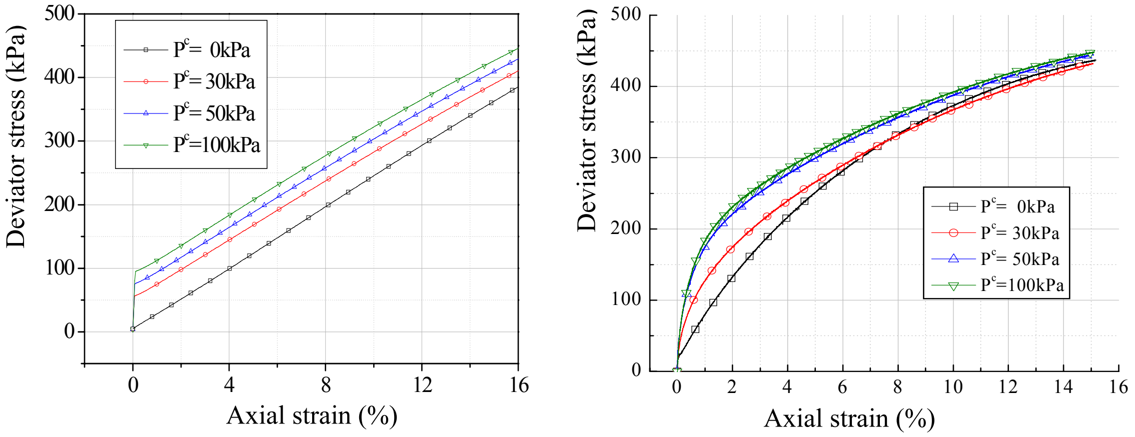

(a) (b)

Figure 3.6 Deviator stress-axial strain relations: (a) simulated results and (b) experimental results

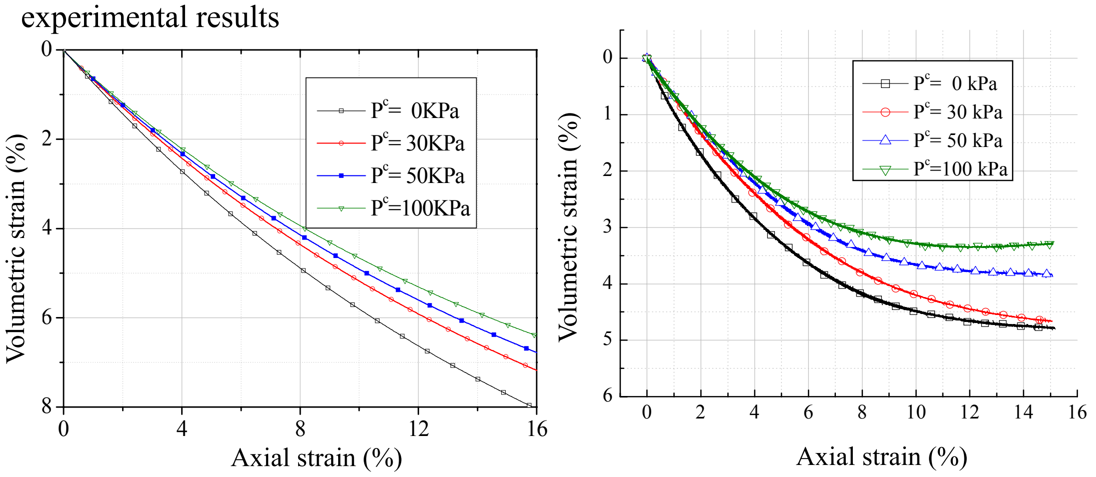

(a) (b)

Figure 3.7 Volumetric strain-axial strain relations: (a) simulated results and (b) experimental results

Figure 3.8 presents the changes in average value of pore water pressure with triaxial compression. The simulation results show that the average value of pore water pressure for the whole sample slowly increases with compression although the the bottom boundary is assumed to be drainage boundary. As the distribution of pore water pressure (Figure 3.9) shows, the excess pore water pressure arose around the top part of the sample with compression due to the lower permeability. In this simulation, the permeability of water is mainly affected by the saturation (Eq. 2.39). This is why the resease in average pore water pressure for the case of a lower degree of saturation (P^c=100kPa) is higher than for the case of a higher degree of saturation case (P^c=30, 50kPa), as shown in Figure 3.8.

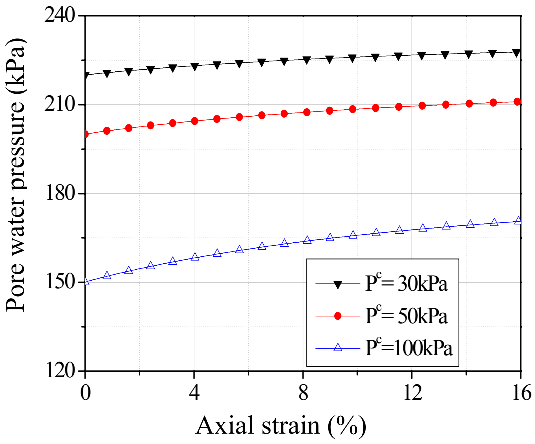

Figure 3.8 Pore water pressure vs. axial strain

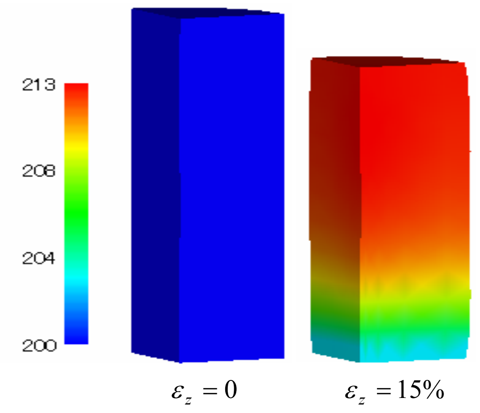

Figure 3.9 Distribution of pore water pressure (P^c=50 kPa)

Figures 3.10 and 3.11 provide simulated results for the changes in suction and the degree of saturation during the compression for different levels of initial suction. The results for all cases show that there is almost no change in pore air pressure with compression under drained conditions, while there is a rise on excess pore water pressure. As a result, the average value for suction in all cases decreases with compression. This decrease in suctions also leads to an increase in the degree of saturation increase with compression in all cases, because this model is based on the van Genuchten type of equation (Equatuon 2.36), and the degree of saturation is assumed as a single function of suction.

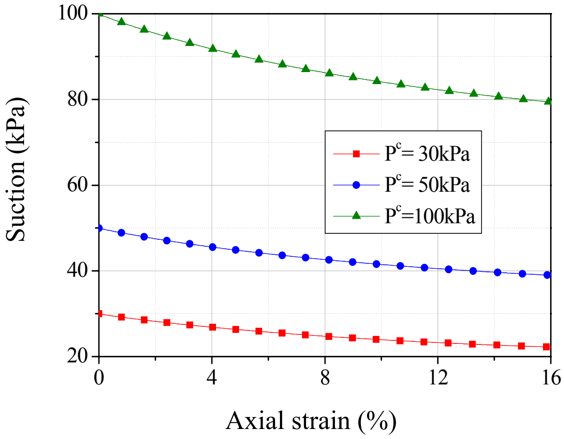

Figure 3.10 Suction vs. axial strain

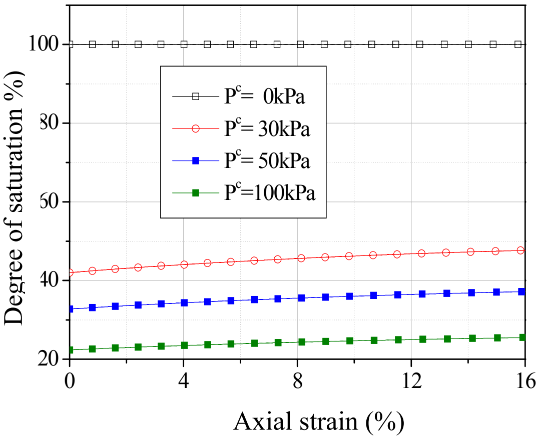

Figure 3.11 Degree of saturation vs. axial strain

Fig. 3.12 shows the distribution of the mean skeleton stress at axial strain levels of 4%, 8%, 12%, and 16% for P^C=50 kPa. A higher level means that the skeleton stress is generated at the center of the top and the bottom of the specimen due to no horizontal displacements on the two surfaces.

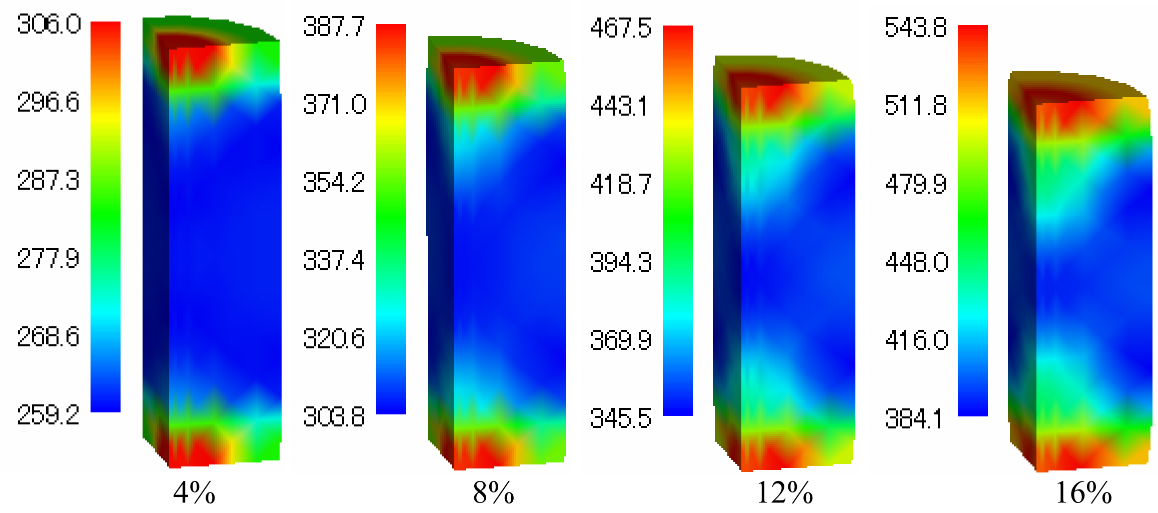
306.0
296.6
287.3
277.9
268.6
259.2
387.7
371.0
354.2
337.4
320.6
303.8
467.5
443.1
418.7
394.3
369.9
345.5
543.8
511.8
479.9
448.0
416.0
384.1
4%
8%
12%
16%

Figure 3.12 Distribution of the mean skeleton stress (kPa) (P^C=50 kPa, Drained)

Figure 3.13 shows the distribution of suction during the compression for case initial suction is 50 kPa. Since the excess pore water pressure is generated at the top part of the specimen, the suction decreases from the top part with compression.

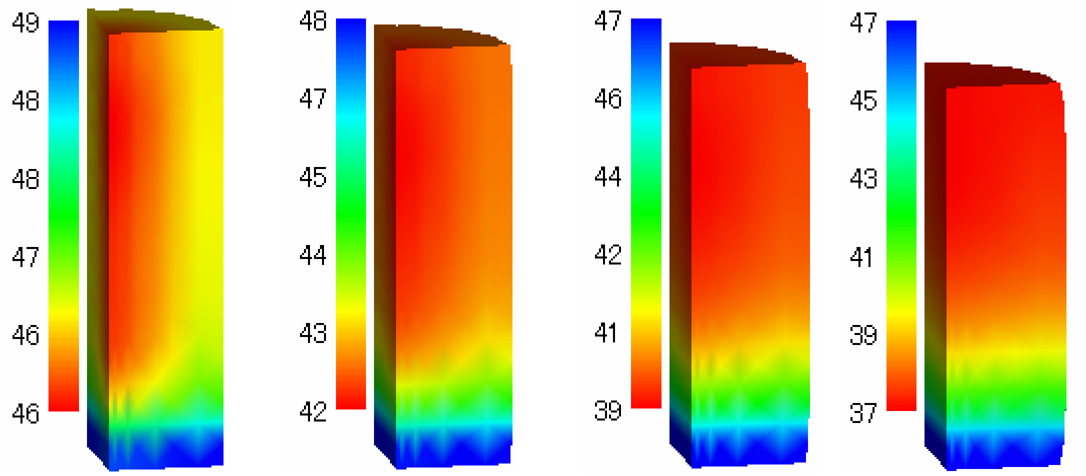

4% 8% 12% 16%

Figure 3.13 Distribution of suction (kPa) (P^C=50 kPa, Drained)

3.4.1.2 Effect of strain rate on triaxial drained behavior

The effects of the strain rate on the behavior of unsaturated soil under under conditions for water and air are investigated. As shown in Table 3.2, the simulations with 0.5%/min and 0.05%/min are compared. Figure 3.14 presents the deviator stress-strain curve under two different strain rates. The predicted results show that the higher strain rates lead to higher levels of deviator stress; this means that the rate-dependent property of unsaturated soil can be reflected with this viscoplastic model.

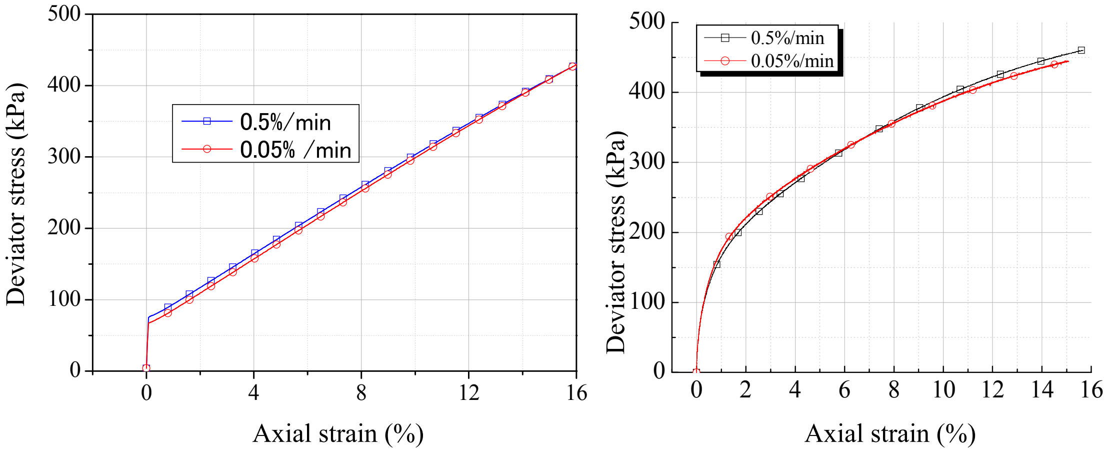

(a) (b)

Figure 3.14 Deviator stress-strain relations under different strain rates: (a) simulated results and (b) experimental results

3.4.1.3 Effect of confining pressure on drained behavior

As shown in Table 3.2, the effects of confining pressure on the behavior of unsaturated soil under drained conditions are investigated. Figure 3.15 presents the deviator stress-axial strain curve under two different levels of confining pressures (100kPa and 200kPa). Agreeing with the experimental results, the simulated results shows that the higher levels of confining pressure leads to higher levels of deviator stress at any given axial strain.

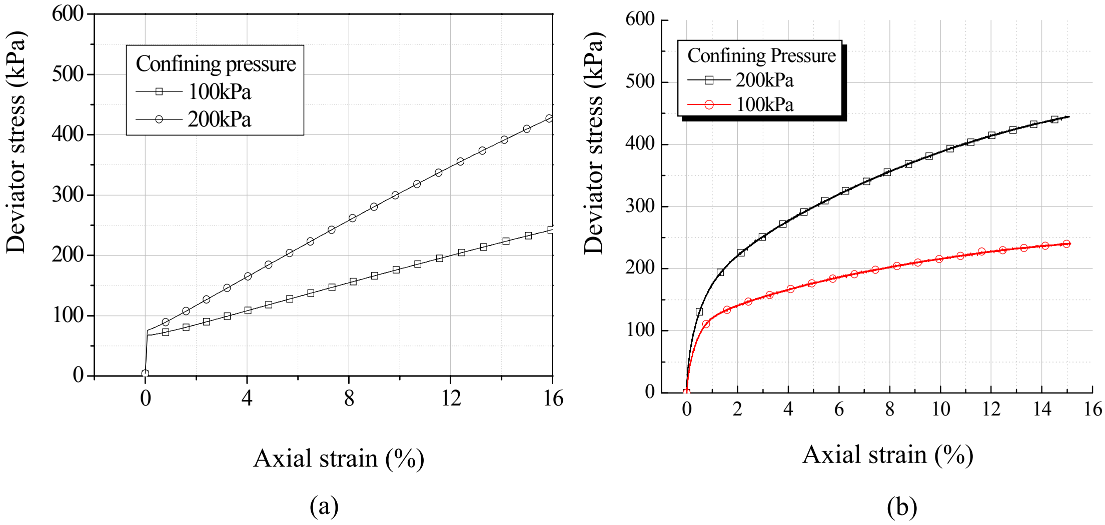

(a)

(b)

Figure 3.15 Deviator stress-strain relations under different levels of confining pressures: (a) simulated results and (b) experimental results

3.4.2 Simulation of the Undrained Tests

Under undrained conditions for both air and water, all of the boundaries are impermeable. As shown in Table 3.2,. numerical simulations are carried out to investigate the effects of initial suctions, strain rates, and confining pressures on the mechanical behaviors of unsaturated soil. Some typical type of behavior of unsaturated soil with compression under undrained conditions for water and air are presented; they include changes in volumetric strain, shear strength, and pore air pressure.

3.4.2.1 Effects of initial suction on triaxial undrained behavior

Predictions of the variations in initial suction were compared against the experimental results. Figure 3.16 illustrates the stress paths of samples at different levels of initial suction. Comparing them with the experimental results, a good agreement can be observed. Introducing the suction effect into the model enables the modle to reflect the fact that the strength of unsaturated soil increases with an increase in the initial suction. In addition, unlike under saturated conditions, the mean skeleton stress also increases with compression due to the existence of gas phase, even under undrained conditions.

Deviator stress-axial strain curves under different levels of initial suctions are given in Figure 3.17. It is seen that the deviator stress is higher in the case of a higher initial suction.

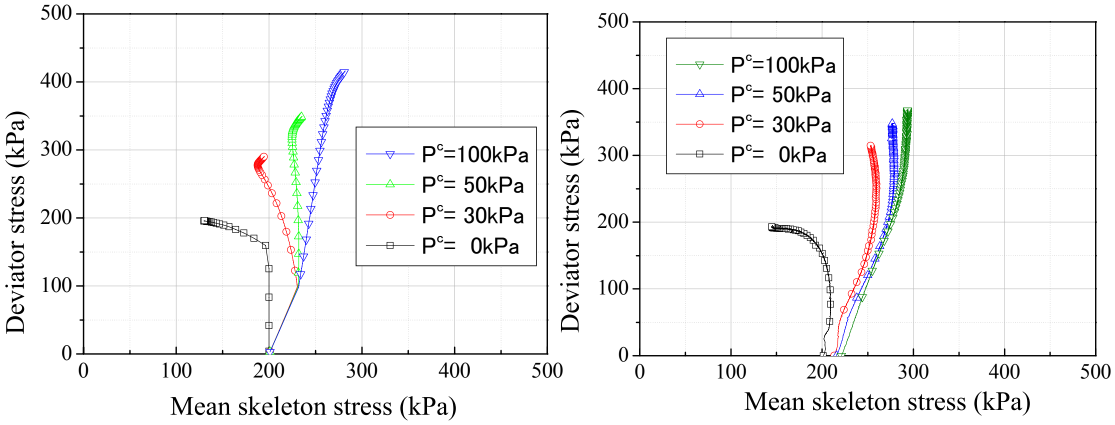

(a)

(b)

Figure 3.16 Stress paths with different levels of initial suction: (a) simulated results and (b) experimental results

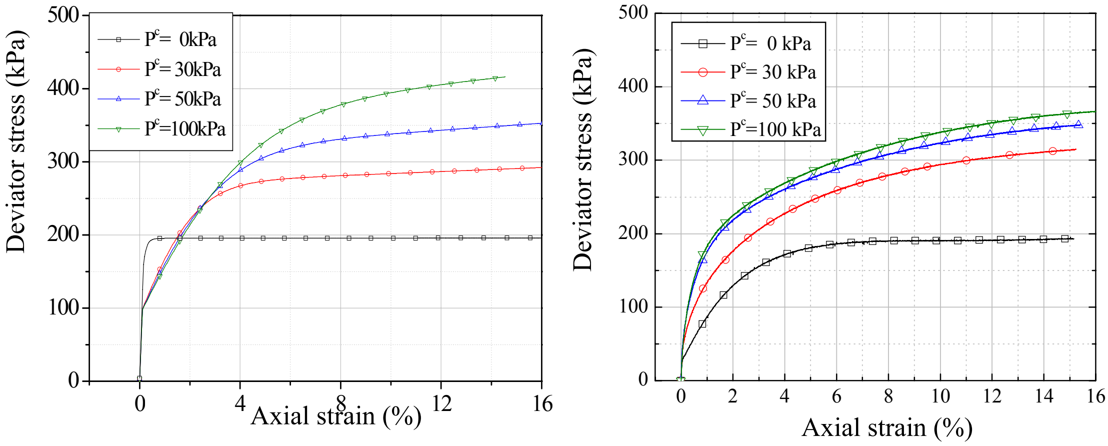

(a)

(b)

Figure 3.17 Deviator stress-axial strain relations with different levels of initial suction: (a) simulated results and (b) experimental results

The predicted volumetric strains during triaxial compression with different levels of initial suction is shown in Figure 3.18. In this model, the pore air is assumed to be compressible and the volumetric strain can be seen as the compression of air. For this reason, the volumetric strain is higher in the case of a higher level of suction due to a higher air content. In this analysis, the degree of saturation depends on sution level which follows the SWCC. In the case of P^c =0 kPa, the calculation is carried out under saturated conditions. As a result, no volumetric strain is predicted.

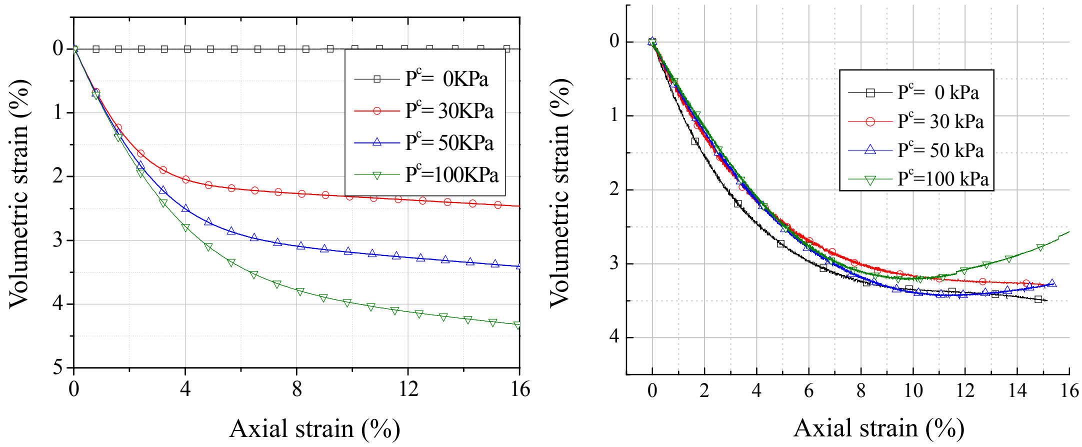

(a) (b)

Figure 3.18 Volumetric strain-axial strain relations with different levels of initial suction: (a) simulated results and (b) experimental results

Figure 3.19 illustrates the relationship between suction and axial strain for different levels of initial suction. Suction ($P^G - P^W$) decreases during compression. This is similar to the experimental results, except at the very beginning where a sudden drop in suction is observed. The cause might the changes in the initial soil structure of the samples.

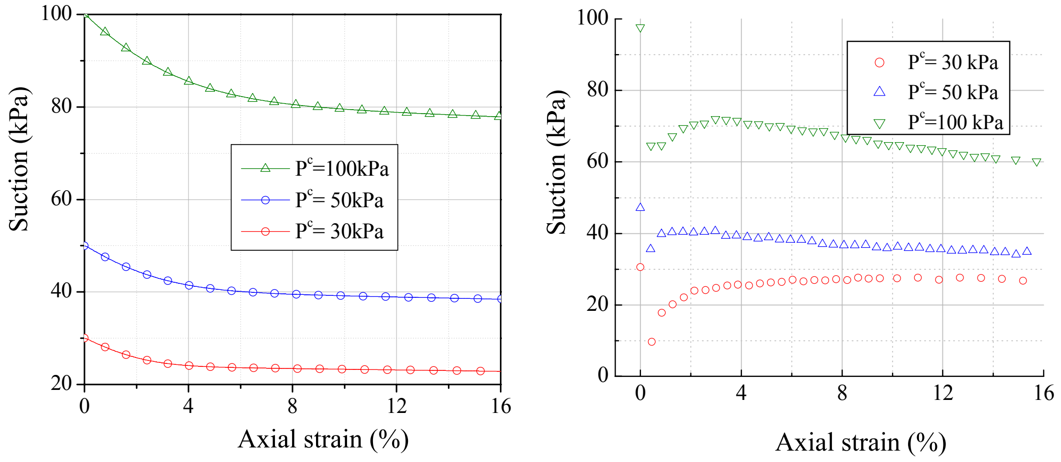

(a) (b)

Figure 3.19 Suction vs. axial strain with different levels of initial suction: (a) simulated results and (b) experimental results

In the coupled multiphase analysis method, the displacement, the pore water pressure, and the pore air pressure are unknown values. Changes in the pore pressure with compression can be calculated under conditions for water and air. Figures 3.20 and 3.21 give the changes in pore water pressure P^W and pore air pressure P^G with compression, respectively. It can be observed that, as with the experimental results, both the pore water pressure and the pore air pressure increase with compression. This means that the proposed model can reflect the changes in pore air pressure change caused by compression. As a result, it is possible to simulate the increase in pore air pressure increase in embankments during heavy rains with this model.

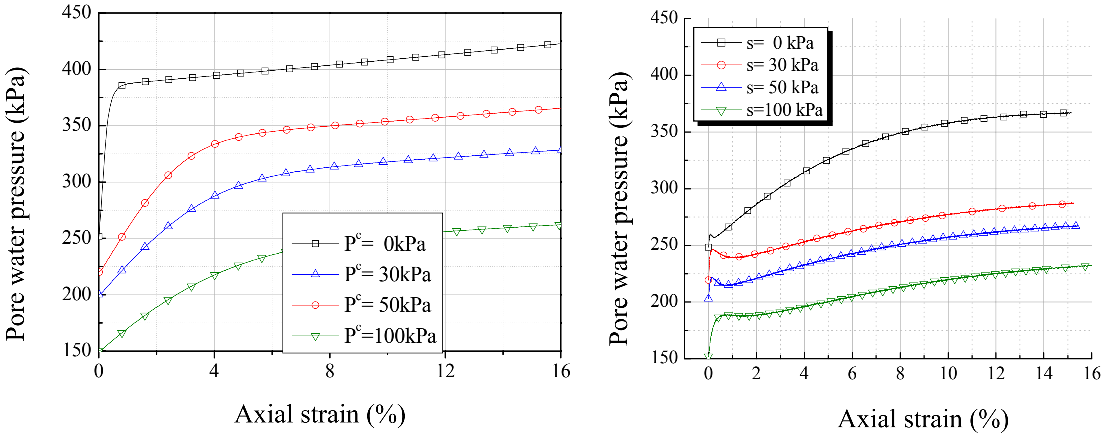

(a) (b)

Figure 3.20 Pore water pressure vs. axial strain with different levels of initial suction: (a) simulated results and (b) experimental results

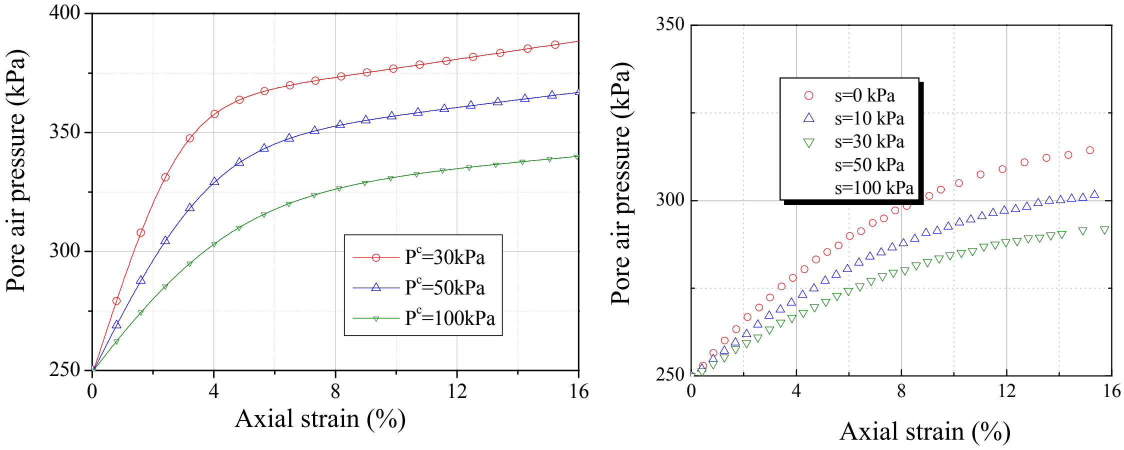

(a) (b)

Figure 3.21 Pore air pressure vs. axial strain with different levels of initial suction

Figure 3.22 shows the distribution of accumulated viscoplastic deviatoric strain, $\gamma^p = \int \sqrt{de_{ij}^{vp} de_{ij}^{vp}}$, at suction levels of 0, 50, and 100 kPa. The regions with higher values indicates larger deformations. It can be observed that at the same axial strain, γ^p is higher for the case of a lower initial suction case. The maximum values for γ^p are concentrated in two separate areas at the beginning, but then move gradually to the center area. This process takes longer when the initial suction is higher. From the figure, suction is seen to affect the mechanical behavior of the unsaturated soil meachnical behavior by delaying the development of the deformation localization.

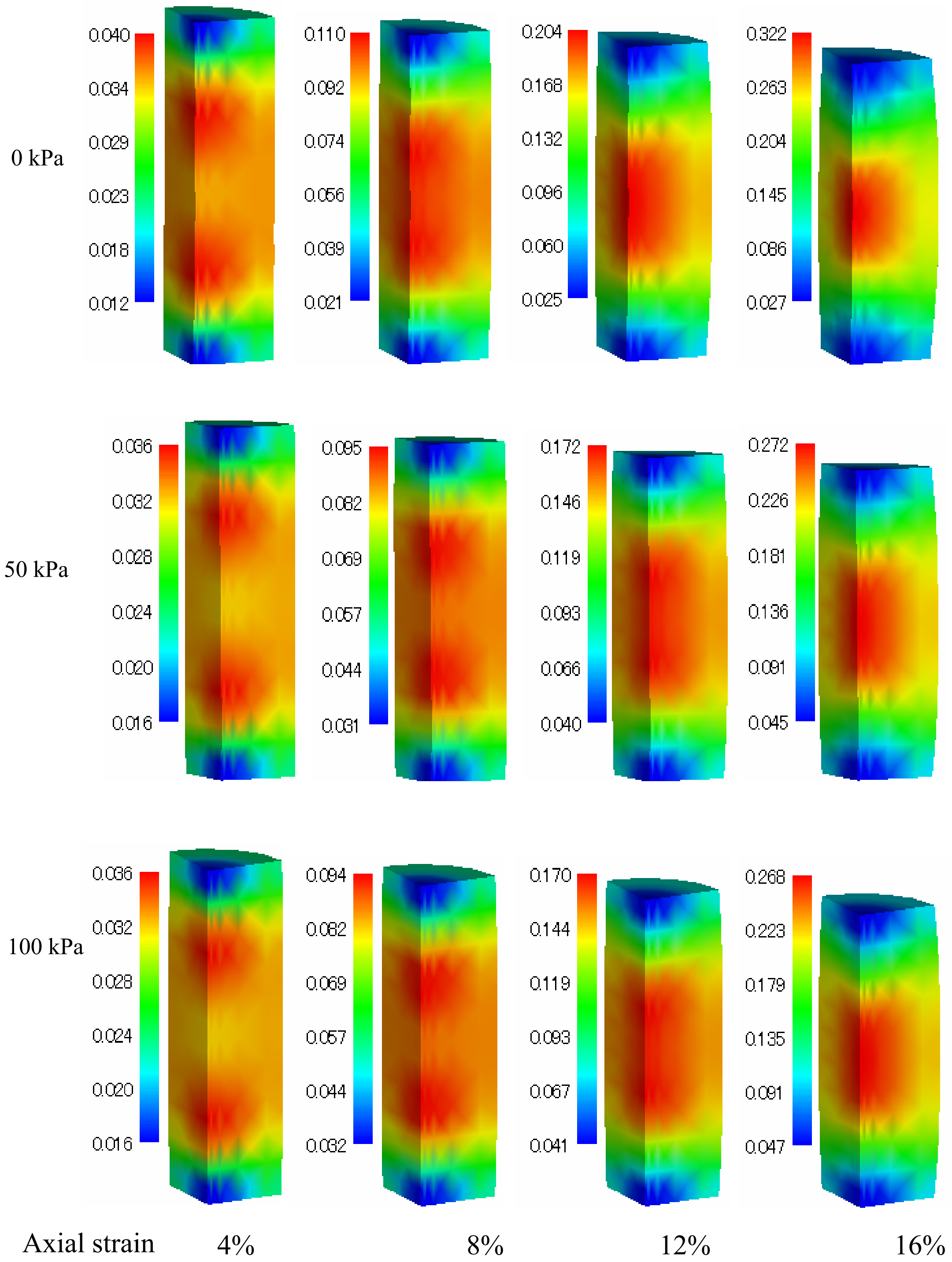

Figure 3.22 Distribution of γ^{P} for the case of different levels of initial suction case (undrained conditions for water and air)

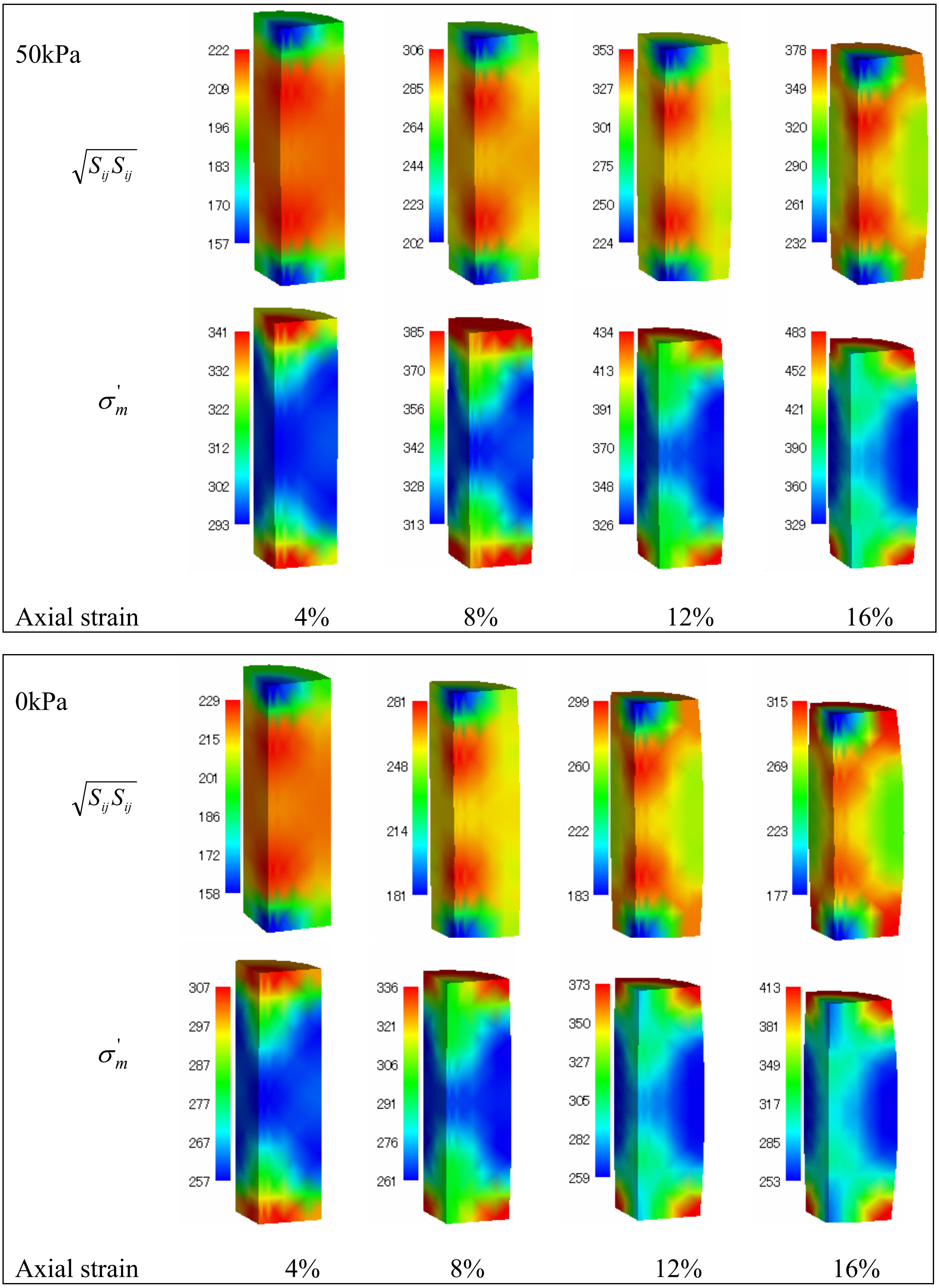

Figure 3.23 Distribution of $\sqrt{S_{ij}S_{ij}}$ and the mean skeleton stress σ'_m under $P^c = 50$ and 0 kPa

Fig. 3.23 shows the distribution of the second invariant value of deviatoric stress $\sqrt{S_{ij}S_{ij}}$, and mean skeleton stress $\sigma_m^{'}$ with the initial suction levels of 50 kPa and 0kPa, respectively. The distribution of mean skeleton stress relates to that of viscoplastic volumetric strain. As a result, we can see that the maximium value of mean skeleton stress are concentrated around the top and the bottom surfaces, since the horizontal deformation is restricted in these regions. The maximium values for both $\sqrt{S_{ij}S_{ij}}$ and $\sigma_m^{'}$, when the initial suction is 50 kPa, are higher than those when the initial suction case is zero. This is due to the effect of suction on soil stiffness.

3.4.2.2 Effects of strain rate on undrained behavior

Rate dependency is an important characteristic of soil for both saturated and unsaturated soil. Many geotechnical problems are related to the rate-dependency property of unsaturated soil, such as the landslides. Therefore, it is necessary to investigate the strain rate behaviors of unsaturated soil under an undrained conditions.

Figures 3.24 and 3.25 show the simulated results for unsaturated soil ($P^c = 50$ kPa) under two different strain rates (0.5%/min and 0.05%/min). The rate-dependent character can be observed in Figure 3.24, namely the higher strain rates lead to higher levels of deviator stress at any given axial strain.

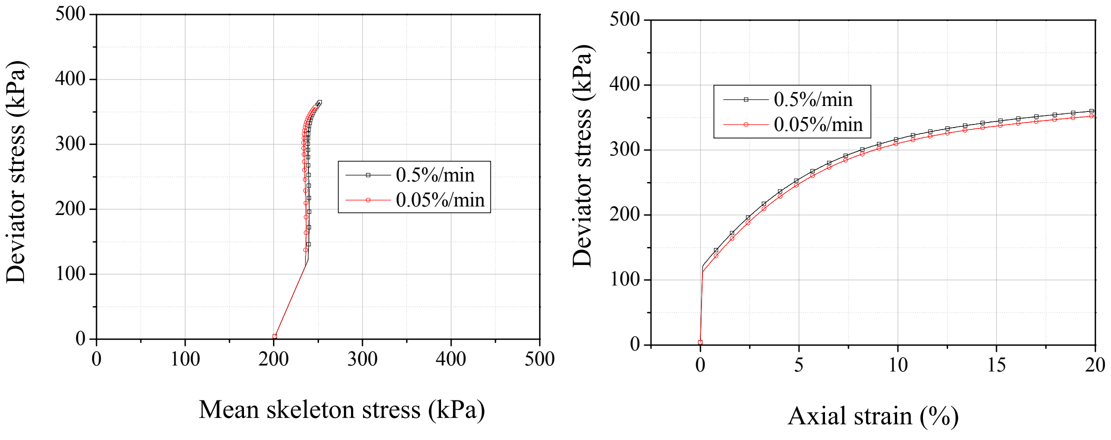

(a) Stress paths

(b) Stress-Strain curves

Figure 3.24 Simulations for different strain rates (P^C =50 kPa)

Changes in volumetric strain are smaller when a higher strain rate is applied, as shown in Figure 3.25 (a). According to the simulated results for changes in pore pressure with compression, higher strain rates generated smaller values of pore water pressure and pore air pressure.

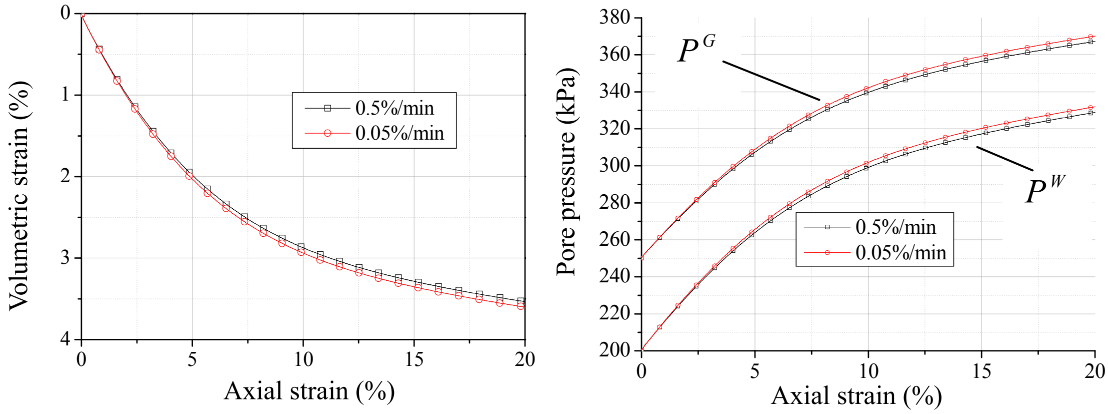

(a) Volumetric strain vs. axial strain (b) Pore pressure vs. axial strain

Figure 3.25 Simulations for different strain rates (P^C =50 kPa)

3.4.2.3 Effects of confining pressure on undrained behavior

In this section, simulations are carried out to investigate the behavior of unsaturated soil under two different levels of confining pressure. Figures 3.26 and 3.27 show the stress paths and stress strain relations.Agreeing well with the experimental results, the strength in the case of a confining pressure of 200 kPa is almost two times of that of the sample with a confining pressure of 100 kPa. In this model, the volumetric strain is related to the mean skeleton stress; therefore, the volumetric strain generated in the case a higher level of confining pressure is larger than that in the case of a lower confining pressure case, as seen in Figure 3.28 (a).

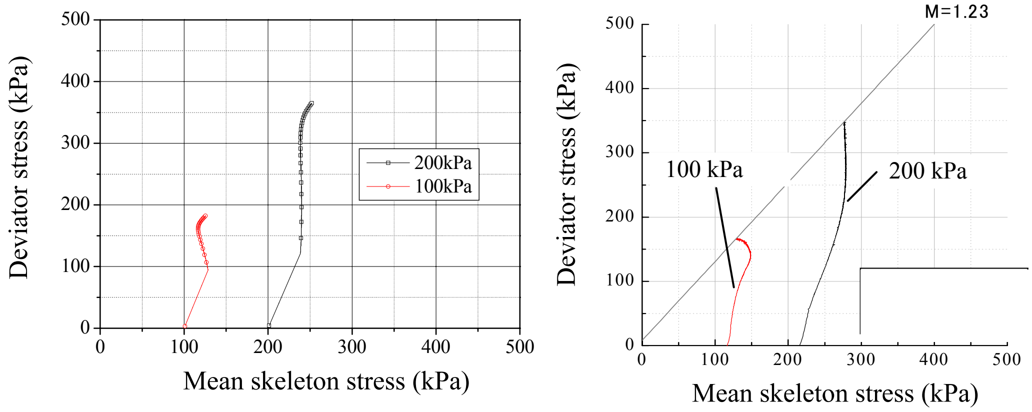

(a) (b)

Figure 3.26 Stress paths for differential levels of confining pressures (P^C =50 kPa): (a) simulated results and (b) experimental results

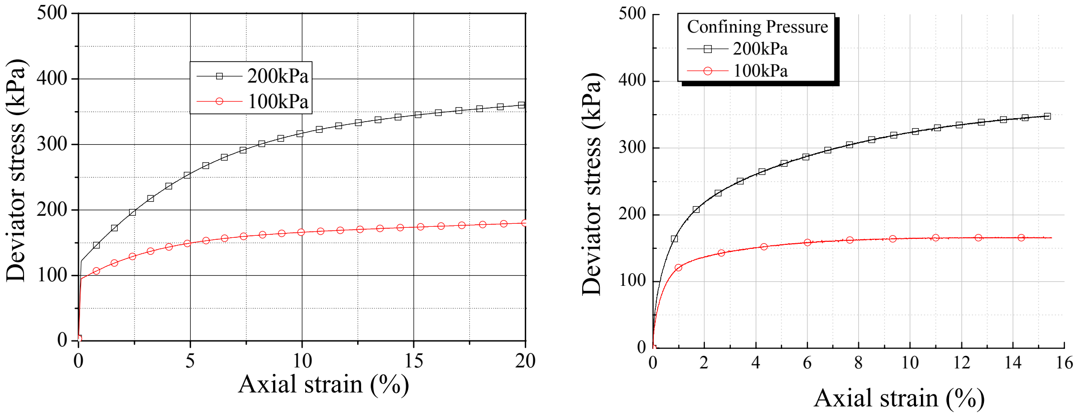

(a)

(b)

Figure 3.27 Simulations for different levels of confining pressures (P^C =50 kPa): (a) simulated results and (b) experimental results

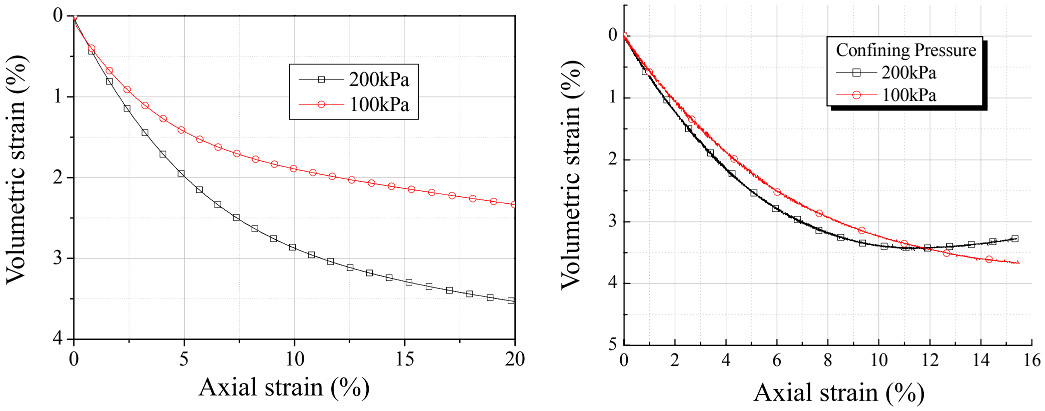

(a)

(b)

Figure 3.28 Volumetric strain-axial strain relations: (a) simulated results and (b) experimental results

3.5 Summary

In this chapter, three-dimensional multiphase numerical simulations of the triaxial compression tests have been conducted using the proposed elasto-viscoplastic model. Using this analysis method, the behaviors of unsaturated soil during triaxial compression under drained and undrained conditions for water and air were reproduced.

Predictions from the elasto-viscoplastic model are in good agreement with the experimental results. The results show that the proposed multiphase formulation is very suitable for describing the mechanical behaviors of unsaturated soil during shearing tests, such as changes in pore-air pressure, pore-water pressure, degree of saturation and volumetric strain. Meanwhile, the model can be used to predict the saturated behavior when the suction is assumed to be zero.

The simulation results also show that by incorporating the suction into the constitutive model, the effects of suction on unsaturated soil can be well described. The results show that a decrease in suction leads to an increase in viscoplastic strain and to an acceleration in strain localization.

In addition, the proposed model can also be used to predict the effects of confining stress and strain rate on unsaturated soil.

Chapter 4

SIMULATION OF THE CYCLIC UNDRAINED BEHAVIOR OF UNSATURATED SOIL USING A CYCLIC ELASTO-VISCOPLASTIC MODEL

4.1 Introduction

The cyclic loading of unsaturated soils is a common phenomenon in geotechnical and geo-environmental engineering. Typical examples are machine foundations on compacted soils, traffic loading on airport and highway pavement, railway embankments, etc. Researchers have recently been focusing on the behavior of foundations composed of different materials, during earthquakes. This behavior includes the interaction of between the sand layer and the clay layer, the total settlement of two layers, and the effect of the clay layer on liquefaction. To accurately predict the behavior of natural foundation with different materials during earthquakes, it is necessary to use the cyclic model in order to reproduce the dynamic behavior of the clay layers. In addition, the natural clay layer is brittle compared to remolded samples due to the ageing and structuralization etc. Most of the cyclic elasto-plastic models proposed up to now, however, do not consider these structure effects of natural clay. Furthermore, it can be found that many civil engineering problems are related to unsaturated soil. Examples of those problems include landslips due to sudden rainstorms, and the damage to natural or constructed slopes brought about by earthquakes. As a consequence, it is important to investigate the deformation behavior of unsaturated structured clay under cyclic loading.

Although the extensive research on the constitutive modeling of unsaturated soils has been conducted, theoretical and experimental investigations into the cyclic behavior of unsaturated soil have been limited (Habte and Khalili 2006). Muraleetharan and Wei (1999) proposed the governing equations for dynamic behavior of unsaturated soil using the Theory of Mixtures with Interfaces. In their model, net stress and suction were adopted as stress variables. Using a single effective stress variable $\dot{\sigma}_{ij}^{'} = \dot{\sigma}_{ij}^{net} + \psi \dot{s} \delta_{ij}$, Habte and Khalili (2006) presented a coupled elasto-plastic model for the cyclic analysis of unsaturated soil. And simulations were carried out under drained condition. However, most of the dynamic engineering problems occur under partially drained condition or undrained condition. For this reason, cyclic triaxial tests of unsaturated silty clay under undrained conditions for water and air have been conducted (Yabuki et al. 2007). In these tests, both the pore water pressure and the pore air pressure have been accurately measured. Based on the elasto-viscoplastic model considering structure degradation effect for saturated soil (Kimoto and Oka 2005), a cyclic elasto-viscoplastic model for unsaturated soil has been proposed (Watanabe et al. 2007).

In this chapter, a cyclic elasto-viscoplastic constitutive model for unsaturated soil is presented. Based on the model, and using the multiphase simulation method, as mentioned in Chapter 2, three-dimensional finite element multiphase simulations of the cyclic behavior of unsaturated soil under undrained conditions for water and air are conducted. The dynamic behavior of unsaturated soil under undrained condition for water and air (constant water and constant air conditions), are investigated with various levels of initial suctions and stress amplitudes.

4.2 Cyclic Elasto-Viscoplastic Constitutive Model for Unsaturated Soil

4.2.1 Assumptions

The cyclic elasto-viscoplastic constitutive model is formulated on the basis of the following assumptions (Oka et al. 1999):

a) Elasto-viscoplastic theory

b) Non-associated flow rule

c) Overconsolidation boundary surface

d) Non-linear kinematic hardening rule

e) Viscoplatic strain-dependent shear modulus (Oka et al. 2004)

f) Suction-dependent boundary surface

The overconsolidation boundary surface adopted to separate the normally consolidated(NC) region from the overconsolidated (OC) region is the one from Equation (2.11).

4.2.2 Static Yield Function

To describe the mechanical behavior of clay at its static equilibrium state, the Cam-clay type of static yield function is assumed as

$$f_y = \overline{\eta}_\chi^* + \widetilde{M}^* \ln \frac{\sigma_m'}{\sigma_{my}'^{(s)}} = 0 \tag{4.1}$$

$$\overline{\eta}_\chi^* = \left\{ \left(\eta_{ij}^* - \chi_{ij}^* \right) \left(\eta_{ij}^* - \chi_{ij}^* \right) \right\}^{\frac{1}{2}} \tag{4.2}$$

where χ_{ij}^* is a nonlinear kinematic hardening parameter, which has the same dimensions as stress ratio η_{ij}^*. In a similar way to Equation (2.24), the value of $\sigma_{my}'^{(s)}$, which controls the size of the static yield surface boundary, changes in suction, viscoplastic volumetric strain, and structure degradation.

4.2.3 Viscoplastic Potential Function

The non-linear kinematic hardening variable is used in the viscoplastic potential function as well as in the yield function. The viscoplastic potential function is given by

$$f_p = \overline{\eta}_\chi^* + \widetilde{M}^* \ln \frac{\sigma_m'}{\sigma_{mp}'} = 0 \tag{4.3}$$

where $\widetilde{M}^*$ is assumed to be constant in the NC region and varies with the current stress in the OC region as

$$\widetilde{M}^* = \begin{cases} (\sigma_m'^* / \sigma_{mb}') M_m^* & (f_b < 0) \\ M_m^* & (f_b \geq 0) \end{cases} \tag{4.4}$$

where $\sigma_m'^*$ denotes the mean effective stress at the intersection of the surface, which has the same shape with f_b and contains the current stress state, with the σ_m' axis as

$$\sigma_m'^* = \sigma_m' \exp\left(\frac{\overline{\eta}_{(0)}^*}{M_m^*} \right) \tag{4.5}$$

4.2.4 Hardening Rule

Nonlinear kinematic hardening parameter χ_{ij}^* is defined by the following differential equation,

$$d\chi_{ij}^* = B^*\left(M_f^* de_{ij}^{vp} - \chi_{ij}^* d\gamma^{vp*}\right) \tag{4.6}$$

where B^* is a material parameter, M_f^* is the stress ratio at the failure state, de_{ij}^{vp} is the deviatoric viscoplastic strain tensor, and $d\gamma^{vp*} = \sqrt{de_{ij}^{vp} de_{ij}^{vp}}$ is the increment of the second invariant deviatoric viscoplastic strain tensor.

Parameter B^* is proposed to be dependent on the viscoplastic strain as follows:

$$B^* = (B_{\max}^* - B_1^*)\exp(-C_f \gamma_{(n)}^{vp*}) + B_1^* \tag{4.7}$$

where B_1^* is the lower boundary of B^*, C_f is the parameter controlling the amount of reduction, $\gamma_{(n)}^{vp*}$ is the accumulated value of the second invariant of the deviatoric viscoplastic strain tensor between two sequential stress reversal points in the previous circle. $B_{\max}^*$ is the maximum value of parameter B^* which is defined by,

$$B_{\max}^* = \begin{cases} B_0^* & \text{Before reaching failure line} \\ \dfrac{B_0^*}{1 + \gamma_{apc}^{vp*} / \gamma_{apr}^{vp*}} & \text{After reaching failure line} \end{cases} \tag{4.8}$$

where, B_0^* is the initial value of B^*, γ_{apc}^{vp*} is the accumulated value of the second invariant of the deviatoric viscoplastic strain tensor after reaching the failure line, and γ_{apr}^{vp*} is the viscoplastic reference strain.

After the stress reaches the failure line, the elastic shear modulus G is also assumed to decrease as

$$G = \frac{G_0}{1 + \gamma_{apc}^{vp*} / \gamma_{apr}^{e*}} \sqrt{\frac{\sigma_m'}{\sigma_{m0}'}} \tag{4.9}$$

G_0 is the initial value of elastic shear modulus G, and γ_{apr}^{e*} is assumed to be the elastic reference strain.

4.2.6 Viscoplastic Flow Rule

The viscoplastic stretching tensor is given in Equation (2.21), in which the static yield function f_y is determined by Equation (4.1), namely,

$$D_{ij}^{vp} = \begin{cases} C_{ijkl}\sigma_m \exp\left\{ m' \left(\overline{\eta}_{\chi}^{*} + \widetilde{M}^{*} \ln \dfrac{\sigma_m'}{\sigma_{mb}'} \right) \right\} \dfrac{\partial f_p}{\partial \sigma_{kl}'} & : \quad f_y > 0 \\ 0 & : \quad f_y \leq 0 \end{cases} \tag{4.10}$$

The viscoplastic deviatoric strain rate and the viscoplastic volumetric strain rate are obtained by

$$\dot{e}_{ij}^{vp} = C_1 \exp\left\{ m' \left(\overline{\eta}_{\chi}^{*} + \widetilde{M}^{*} \ln \frac{\sigma_m'}{\sigma_{mb}'} \right) \right\} \frac{\eta_{ij}^{*} - \chi_{ij}^{*}}{\overline{\eta}_{\chi}^{*}} \tag{4.11}$$

$$\dot{\varepsilon}_{kk}^{vp} = C_2 \exp\left\{ m' \left(\overline{\eta}_{\chi}^{*} + \widetilde{M}^{*} \ln \frac{\sigma_m'}{\sigma_{mb}'} \right) \right\} \left\{ \widetilde{M}^{*} - \frac{\eta_{mn}^{*} \left(\eta_{mn}^{*} - \chi_{mn}^{*} \right)}{\overline{\eta}_{\chi}^{*}} \right\} \tag{4.12}$$

As mentioned in Chapter 2, in order to evaluate viscoplastic stretching tensor D_{ij}^{vp}, the tangent modulus method (as mentioned in section 2.3.3) is adopted. Considering adoption of nonlinear kinematic hardening parameter χ_{ij}^{*}, in this model, the tangential stiffness matrix $C_{ijkl}^{\tan}$ and relaxation stress Q_{ij} are given as follows:

$$C_{ijkl}^{\tan} = C_{ijkl}^{e} - C_{ijrs}^{e} C_{rsmn} \frac{\partial f_p}{\partial T_{mn}'} \frac{1}{1+\xi} \theta \Delta t \frac{\partial \Phi}{\partial T_{pq}'} C_{pqkl}^{e} \tag{4.13}$$

$$Q_{ij} = C_{ijkl}^{e} C_{klmn} \frac{1}{1+\xi} \left[\Phi_t + \theta \Delta t \frac{\partial \Phi}{\partial \chi_{st}'} B^{*} (M_f^{*} \dot{e}_{st}^{vp} - \chi_{st}^{*} \dot{\gamma}^{vp}) \right] \frac{\partial f_p}{\partial T_{mn}'} \tag{4.14}$$

4.3 Numerical Analyses

Using the cyclic elasto-viscoplastic constitutive model and the multiphase coupled formulations which are presented in Chapter 2, three-dimensional multiphase finite element simulations are conducted to simulate the triaxial cyclic behaviors of unsaturated soil. In most dynamic civil engineering problems, such as natural slope under earthquakes, happen under undrained conditions, simulations are carried out under undrained conditions for water and air (constant water and constant air content).

The finite element mesh and the boundary conditions for the analyses are shown in Fig. 3.3. As shown in Table 4.1, the triaxial cyclic behavior of unsaturated soil at different levels of initial suction and stress amplitude are investigated. In the computations, the cyclic load is applied using the strain rate control method. At the beginning, the axial strain rate is set at 0.5%/min; once the stress amplitude is reached, -0.5%/min is applied. This pattern is repeated until the end. The time increment is 0.48, and the increment in axial strain for each step used is $\Delta\varepsilon_{zz} = 0.004\%$.

The parameters used in the analyses are listed in Table 4.2. All together, there are twenty seven material parameters are required by in present multiphase analysis. In addition to the twenty two parameters used for monotonic analysis (as mentioned in 3.3.2), there are five new parameters are adopted to describe the cyclic behavior of unsaturated soil. They are non-linear kinematic hardening parameters B_0^*, B_1^*, C_f, and γ_{apr}^{vp*}; and elastic reference strain γ_{apr}^{e*}. Parameter study method is adopted to determine the five parameters.

Table 4.1 Simulated cases

Case	U0-40/80/100			U50-40/80/100		
Initial suction (kPa)	0			50		
Deviator stress amplitude (kPa)	0	80	100	0	80	100

Table 4.2 Material parameters

Initial void ratio e_0	1.14
Elastic shear modulus G_0 (GPa)	34.8
Initial yield stress σ'_{mbi} (kPa)	200
Swelling index κ	0.0094
Compression index λ	0.105
Viscoplastic parameter m'	52
Viscoplastic parameter C_1(1/s)	6.0×10^{-7}
Viscoplastic parameter C_2(1/s)	4.0×10^{-7}
Stress ratio at critical state M^*_m	1.0
Structural parameter σ'_{maf} (kPa)	60
Structural parameter β	4.5
Reference suction P_i^C (kPa)	100
Suction parameter S_I	0.4
Suction parameter S_d	0.6
Parameter α (1/kPa)	0.04
Parameter n	1.25
Hardening parameter B_0^*	80
Hardening parameter B_1^*	15
Hardening parameter C_f	2.0
Viscoplastic reference strain γ_{apr}^{vp*} %	0.12
Elasto reference strain γ_{apr}^{e*} %	0.18

4.3.1 Simulated Results at P^C=0 kPa

In this section, simulation results for the case in which $P^c = 0$ kPa are presented. As mentioned in Chapter 3, when the suction is equal to 0 kPa in analyses, the degree of saturation is set to be 1, namely, under saturated conditions.

The simulated results and the corresponding experimental results (Yabuki 2007) for the case of U0-40 are shown in Figures 4.1~4.4. For this case, 150 cycles are simulated. Figure 4.1 shows the deviator stress-strain curves. In agreement with the experimental results, the extensive axial strain is very small in comparison to the compressive axial strain. The stress paths under cyclic loading are shown in Figure 4.2. It can be seen that the decrease in amplitude of the mean skeleton stress is larger in the first compression cycle than that during the following cycles. The possible reason is that the overconsolidation boundary surface expanded with the accumulation of viscoplastic strain. It can also be seen that due to the lower stress amplitude, the sample has still not reached the failure line after 150 cycles.

Changes in the pore water pressure with time are shown in Figure 4.3. The simulated results show that the average pore water pressure keeps increasing with time. It can be seen that, compared with the experimental results, the simulated pore water pressure increases more quickly. The reason is that for the experiments, the soil is still unsaturated in the case where the suction is equal to zero. The existence of the gas phase in the soil reduces the generation of pore water pressure with cyclic loading.

For the similar reason, as shown in Figure 4.4, the simulated volumetric strain is almost equal to zero, while the volumetric strain can be observed with increase of cyclic axial strain in triaxial cyclic experimental results.

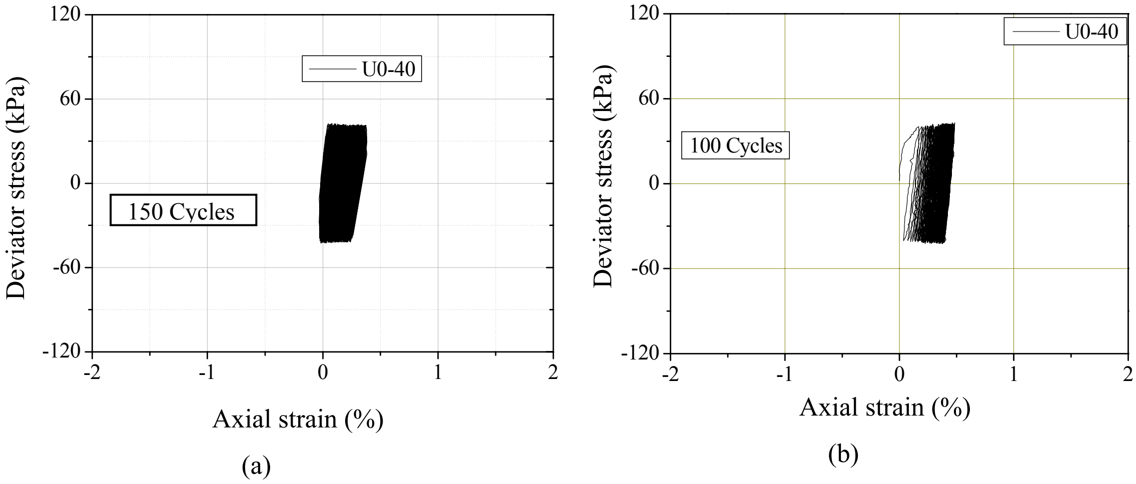

Figure 4.1 Deviator stress-axial strain relations: (a) Simulated results and (b) experimental results

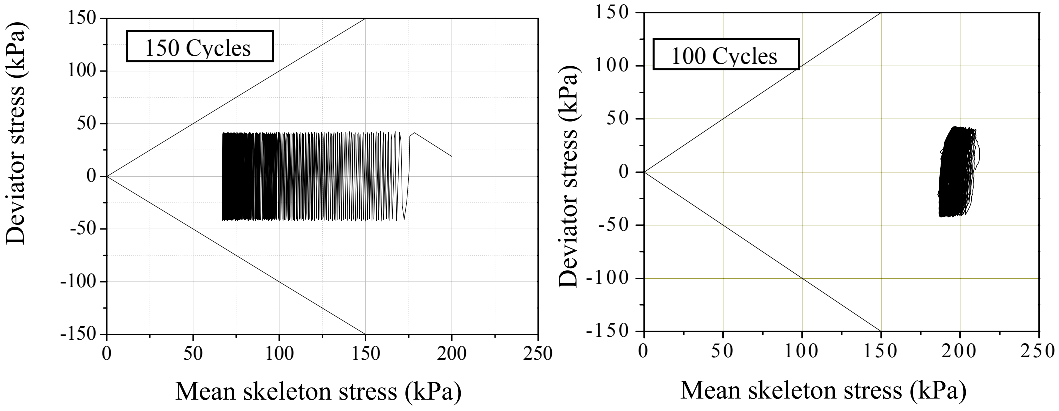

(a) (b)

Figure 4.2 Stress paths: (a) simulated results and (b) experimental results

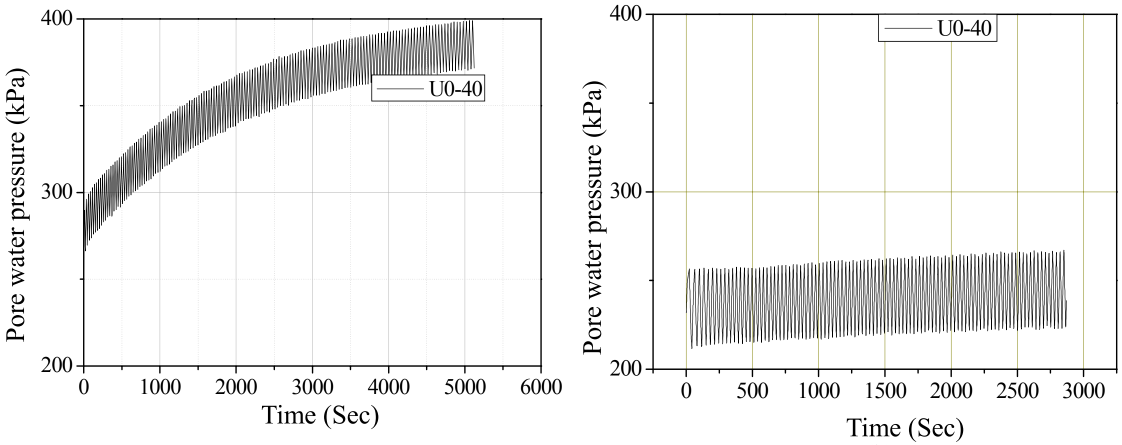

(a) (b)

Figure 4.3 Pore water pressure vs. time: (a) simulated results and (b) experimental results

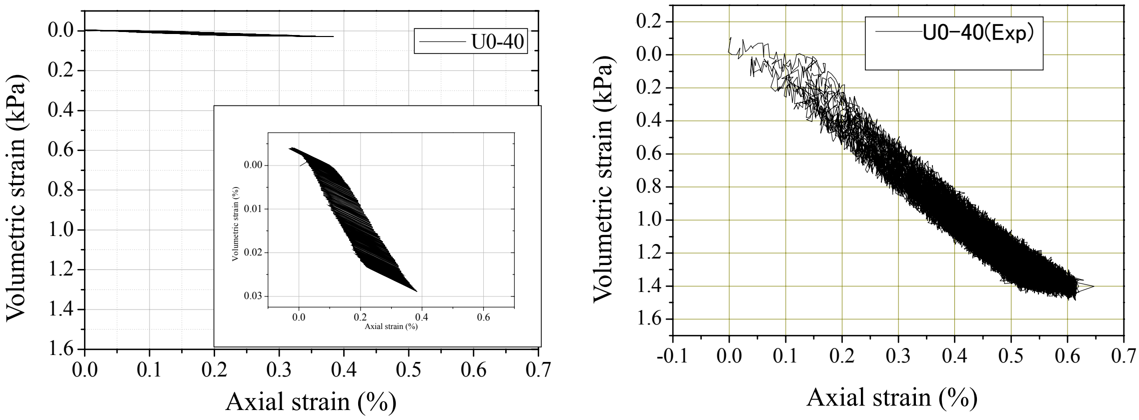

(a) (b)

Figure 4.4 Volumetric strain-axial strain relations: (a) Simulated results and (b) Experimental results

Figures. 4.5~ 4.8 show the simulated results for the case in which the stress amplitude is 80 kPa. In this case, the loading has been carried out until 50 cycles. The deviator stress-axial strain curves are shown in Fig. 4.5. The axial strain is larger that the case in which stress amplitude is equal to 40 kPa. It also can be seen that once the stress state reached the failure line, the axial strain becomes large.

Fig. 4.6 shows the stress paths. As expected, the sample reaches the failure line after 50 cycles due to the increase of stress amplitude. As shown in Figure 4.7, no volumetric strain is simulated for the same reason as that mentioned previously. Changes in the pore water pressure with cyclic loading are shown in Figure 4.8. It can be observed that the produced average excess pore water pressure is higher than in the case with a lower stress amplitude.

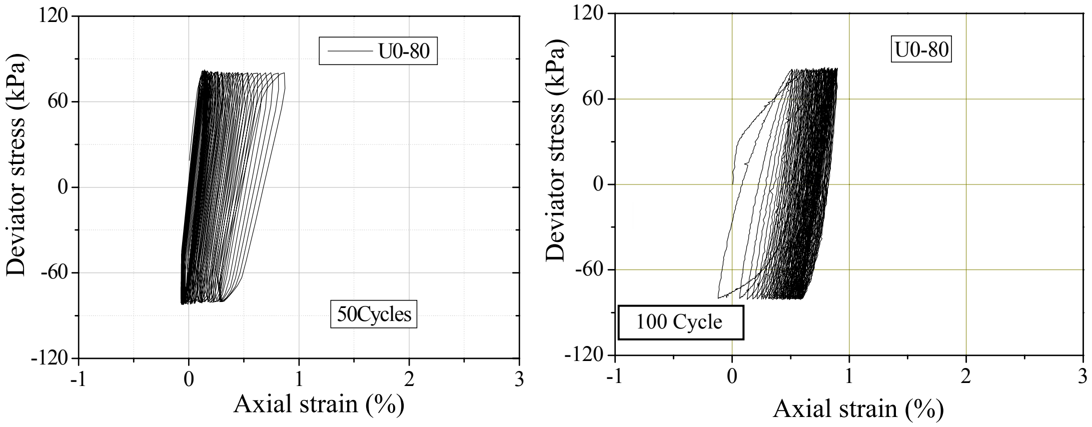

(a) (b)

Figure 4.5 Deviator stress-axial strain relations: (a) simulated results and (b) experimental results

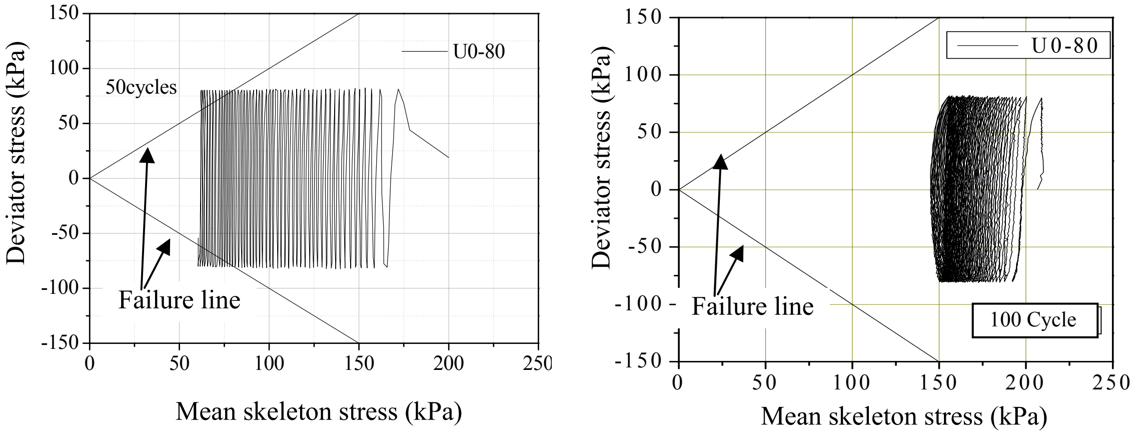

(a) (b)

Figure 4.6 Stress paths. (a) simulated results and (b) experimental results

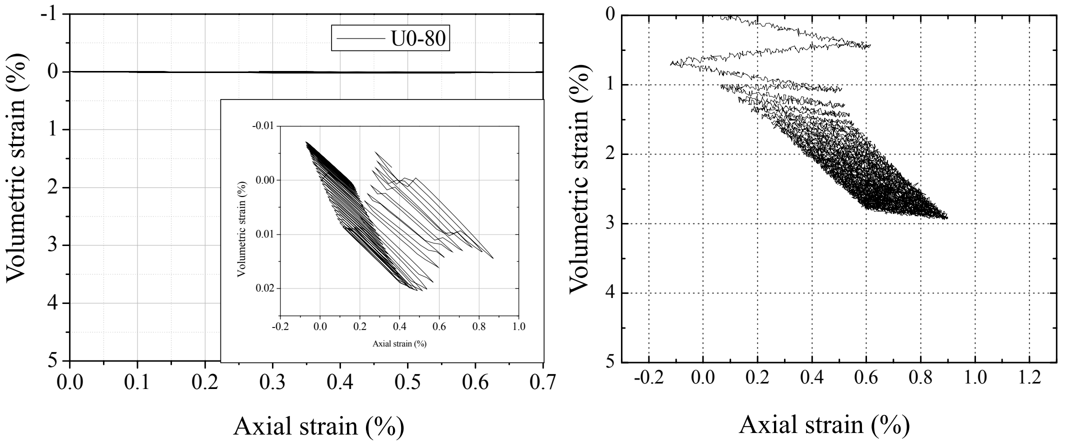

(a) (b)

Figure 4.7 Volumetric strain-axial strain relations: (a) simulated results and (b) experimental results

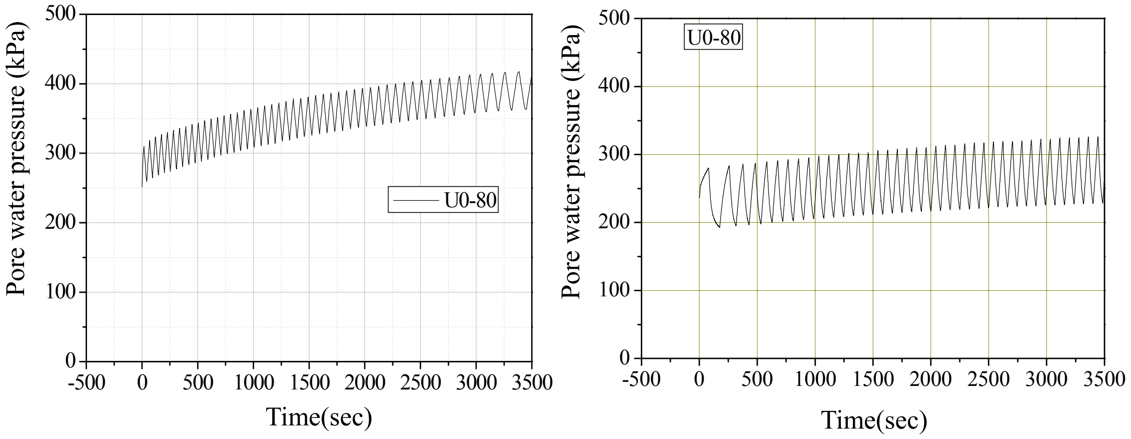

(a) (b)

Figure 4.8 Pore water pressure vs. time:(a) simulated results and (b) experimental results

Figures 4.9~4.12 show the simulated and the experimental results for the case in which the stress amplitude is 100 kPa and the initial suction of 0 kPa. The calculation is carried out until 29 loading cycles have been applied. The deviator stress-axial strain relations are shown in Figure 4.9. The simulation results show that after the failure line has been reached, the axial strain-stress loop becomes larger. The reason is similar to the case in which the stress amplitude is 80 kPa. Meanwhile, the deviatoric stress-strain loops gradually move to compressive strain side with the loading. However, the experimental results show opposing behavior. Figure 4.10 provides the stress paths for the simulation and the experiment. Figure 4.11 presents the changes in pore water pressure with time. As shown in Figure 4.12, in a similar way to the other cases in which the initial suction is zero, the simulation results show no volumetric strain.

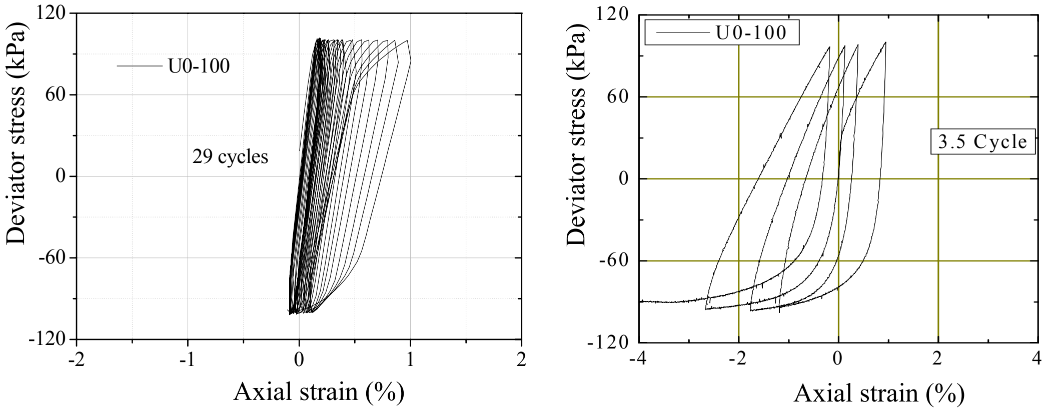

(a) (b)

Figure 4.9 Deviator stress-axial strain relations: (a) simulated results and (b) experimental results

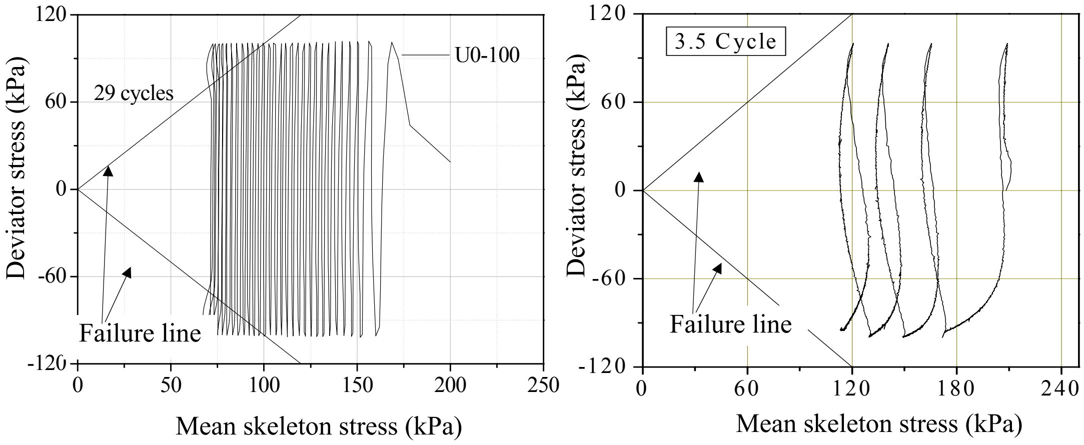

(a) (b)

Figure 4.10 Stress paths: (a) simulated results and (b) experimental results

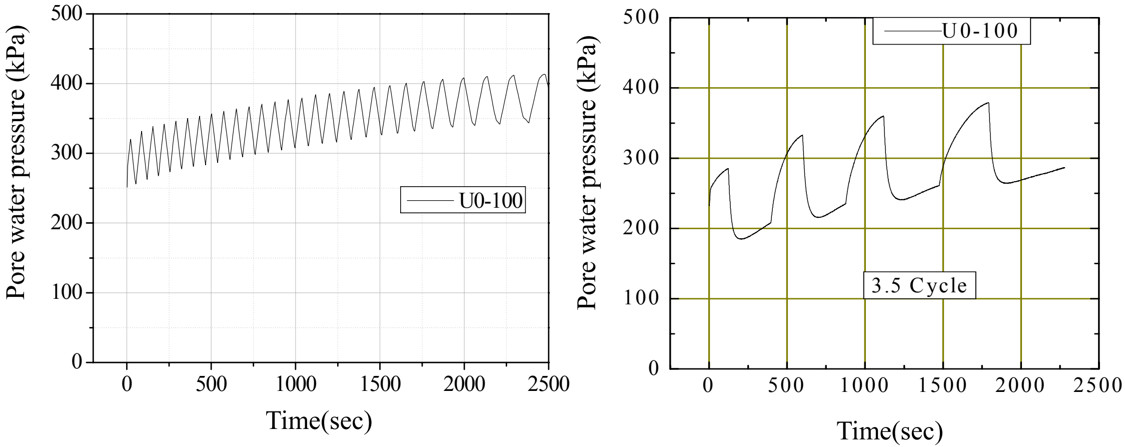

(a) (b)

Figure 4.11 Pore water pressure vs. time: (a) simulated results and (b) experimental results

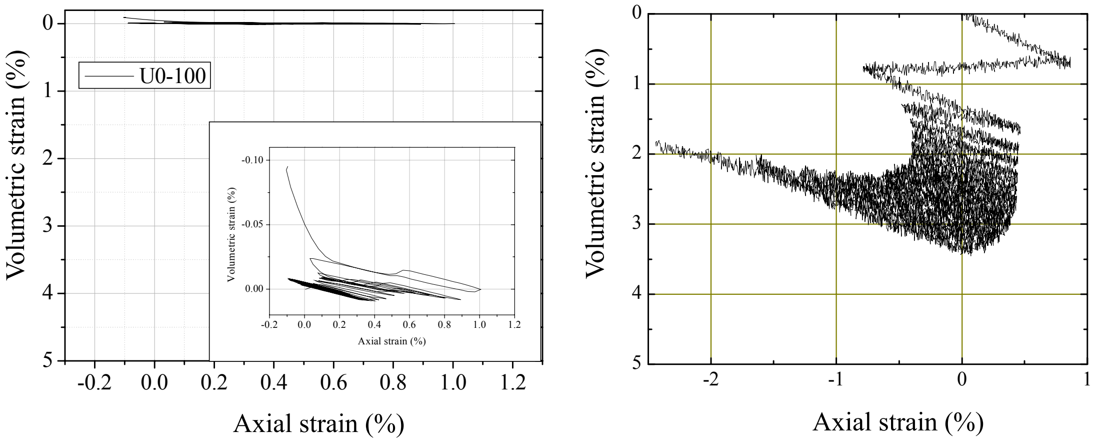

(a)　　(b)

Figure 4.12 Volumetric strain-axial strain relations: (a) simulated results and (b) experimental results

4.3.2 Simulated Results at P^C=50 kPa

In this section, the undrained cyclic behavior of the sample under an initial suction of 50 kPa is investigated.

Figures 4.13~ 4.18 provide the simulated results and the corresponding experimental results for the case in which the stress amplitude is 40 kPa (U50-40). The deviator stress-axial strain relationships are given in Figure 4.13. due to the lower stress amplitude, the development of axial strain for each cycle is small. A good agreement can be seen between the simulated results and the experimental results. The stress paths are shown in Figure 1.14. It can be observed that the mean skeleton stress increases during compression under undrained conditions due to the suction effect. A similar phenomenon can also be seen in the case of monotonic loading.

Figure 4.15 presents the changes in pore water pressure and the pore air pressure with time. It can be seen that the average values for both the air pressure and water pressure increases with time. As for the experimental results, the pore water pressure increases in a similar way, while the pore air pressure increases only at the beginning. Consequently, the increase in the predicted suction is lower than in the experimental results, as shown in Figure 4.16. Figure 4.17 shows the changes in the degree of saturation with time. Figure 4.18 illustrates the changes in volumetric strain with axial strain. Good agreement can be observed between the predicted volume change and experimental results.

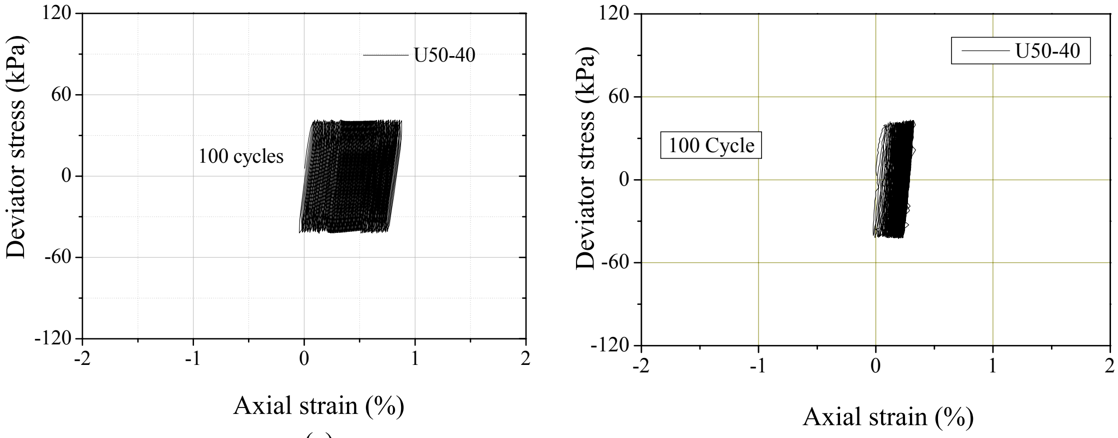

(a) (b)

Figure 4.13 Deviator stress-axial strain relations: (a) simulated results and (b) experimental results

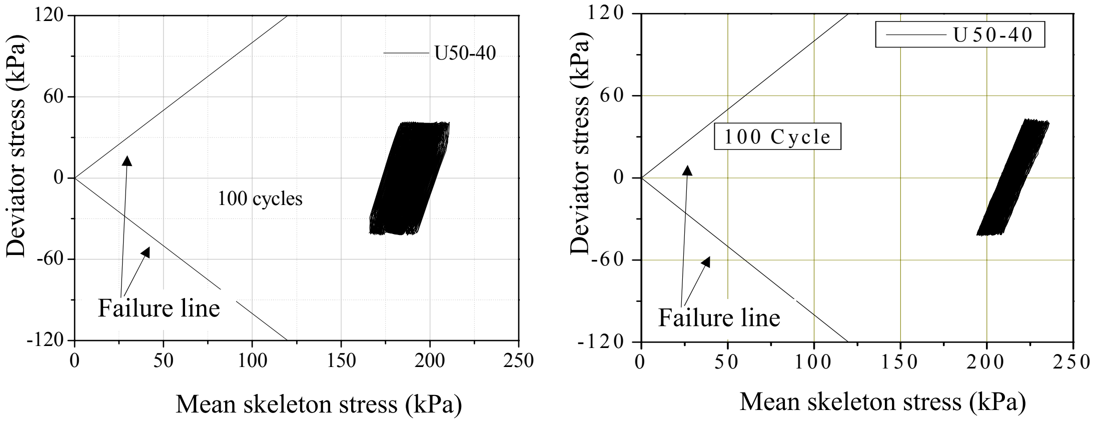

(a) (b)

Figure 4.14 Stress paths: (a) simulated results and (b) experimental

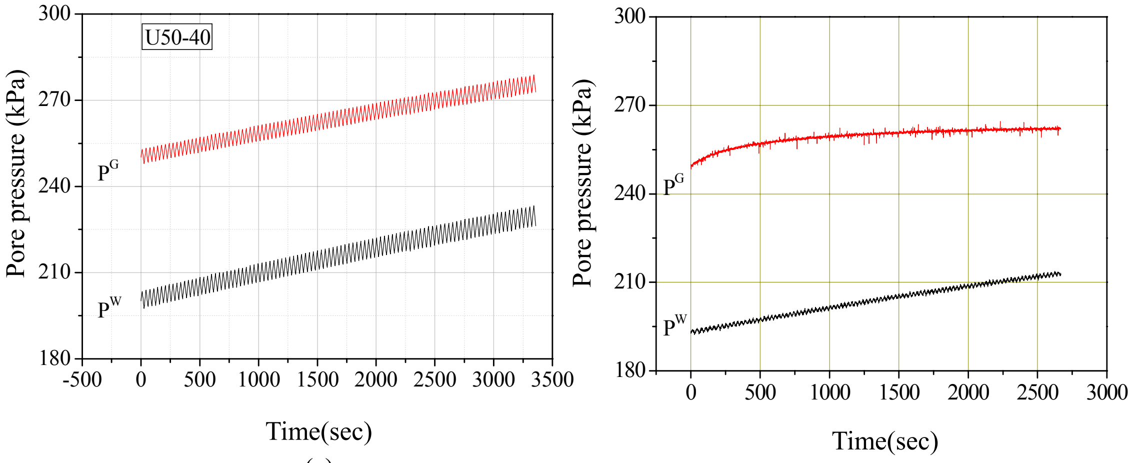

(a) (b)

Figure 4.15 Pore pressure vs. time: (a) simulated results and (b) experimental results

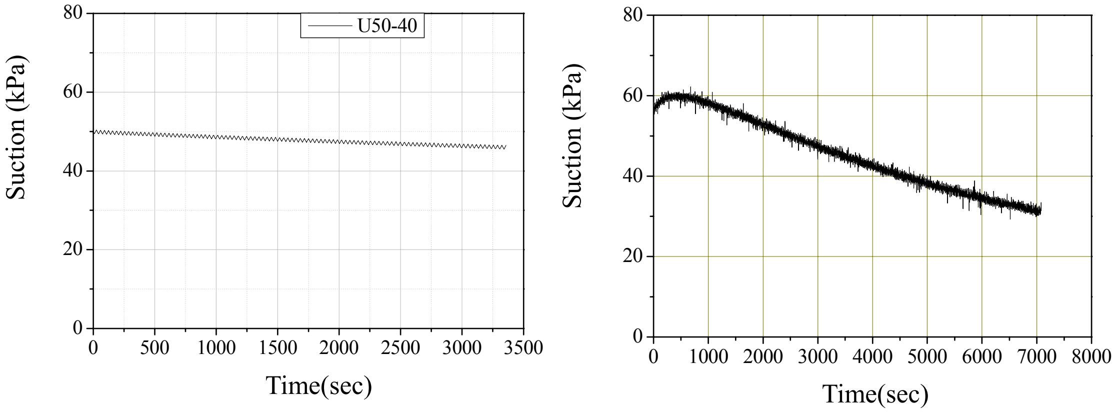

(a)

(b)

Figure 4.16 Suction vs. time: (a) simulated results and (b) experimental results

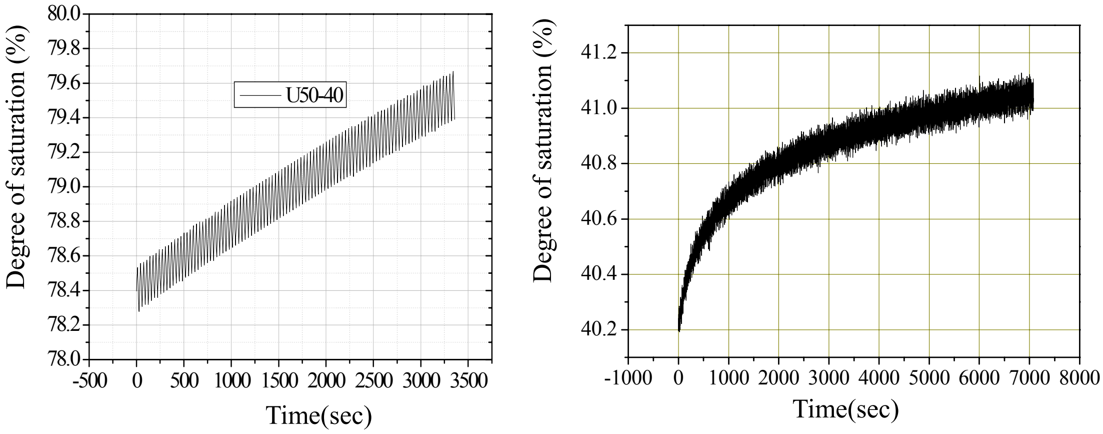

(a)

(b)

Figure 4.17 Degree of saturation vs. time: (a) simulated results and (b) experimental results

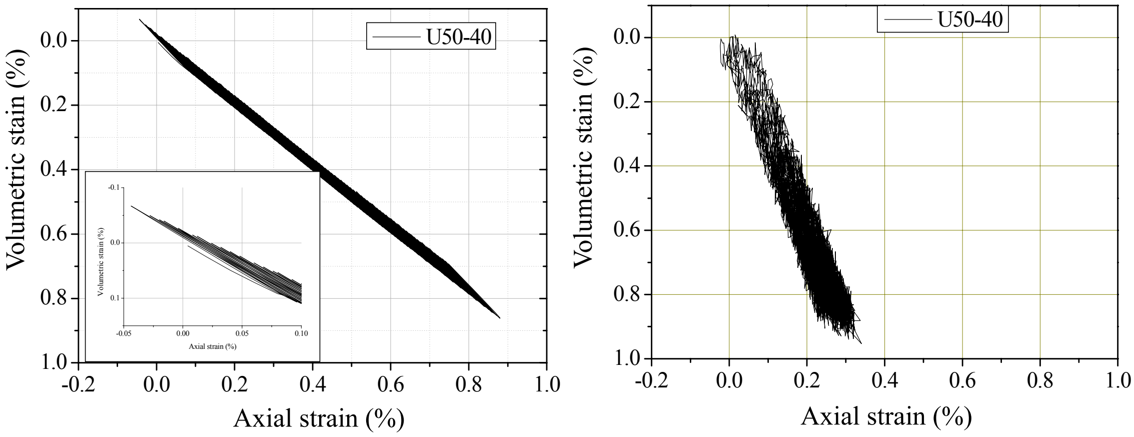

(a)

(b)

Figure 4.18 Volumetric strain-axial strain relation: (a) simulated results and (b) experimental results

Figures 4.19~4.24 provide the results for the case in which the stress amplitude is 80 kPa. The simulation is carried out until the failure line is reached at 100 loading cycles. The deviator stress-axial strain relations are shown in Figure 4.19. The deviator stress-strain loops are closer to the previous ones with an increased number of cycles. The same phenomenon can be observed in the stress path, as shown in Figure 4.20.

Time changes in the pore water pressure and the pore air pressure are shown in Figure 4.21. Compared with Figure 4.15, both the pore water pressure and the pore air pressure are larger than those in the case of a small deviator stress amplitude. Figure 4.22 shows changes in suction with number of cycles. Figure 4.23 provides the changes in the degree of saturation with time. It can be seen that the suction decreases with an increase in the number of cycles. The volumetric strain with cyclic loading is shown in Figure 4.24.

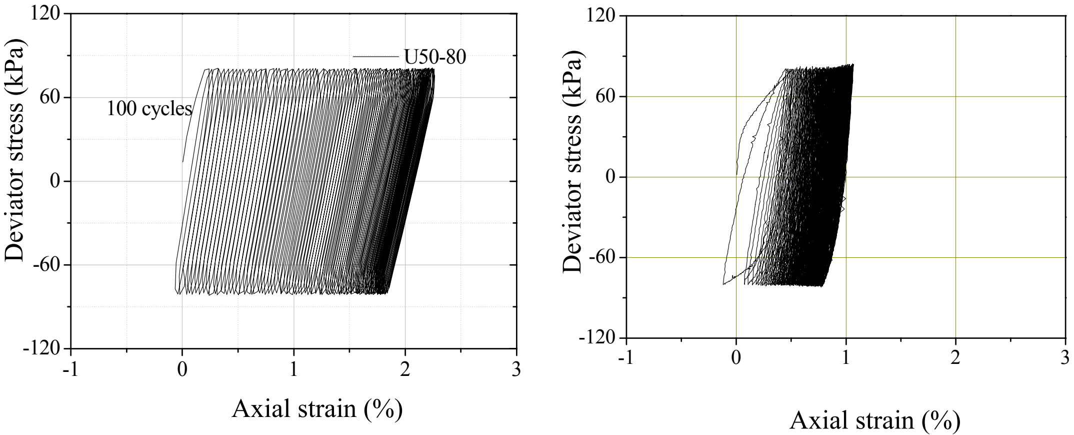

(a)

(b)

Figure 4.19 Deviator stress-axial strain relations: (a) simulated results and (b) experimental results

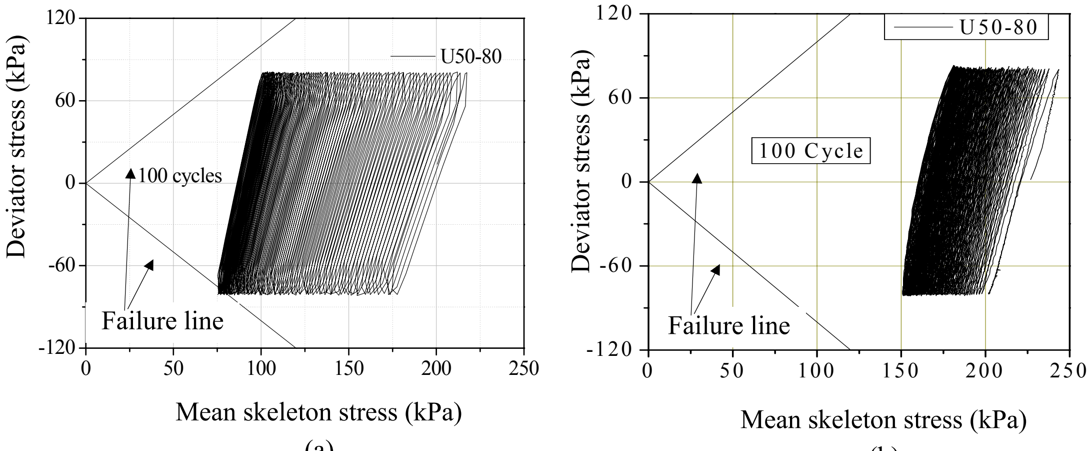

(a)

(b)

Figure 4.20 Stress paths: (a) simulated results and (b) experimental results

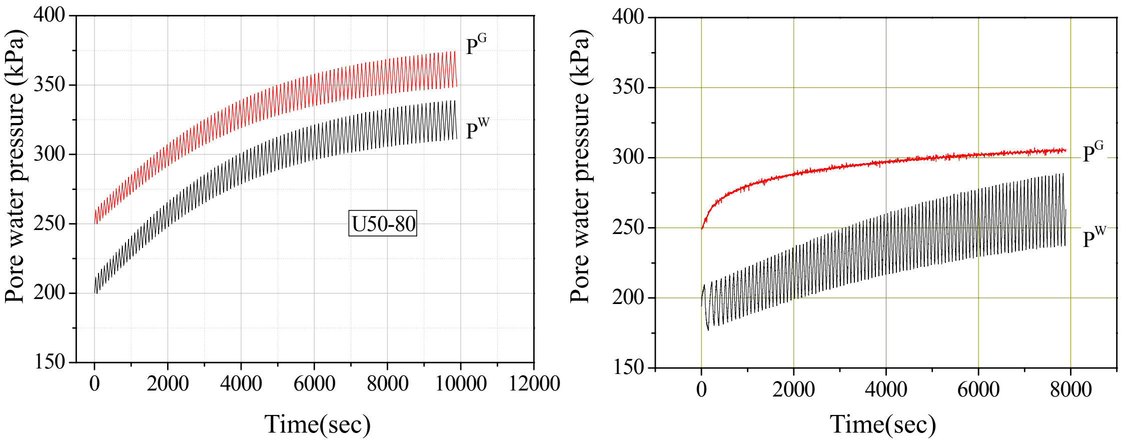

(a)

(b)

Figure 4.21 Pore pressure vs. time: (a) simulated results and (b) experimental results

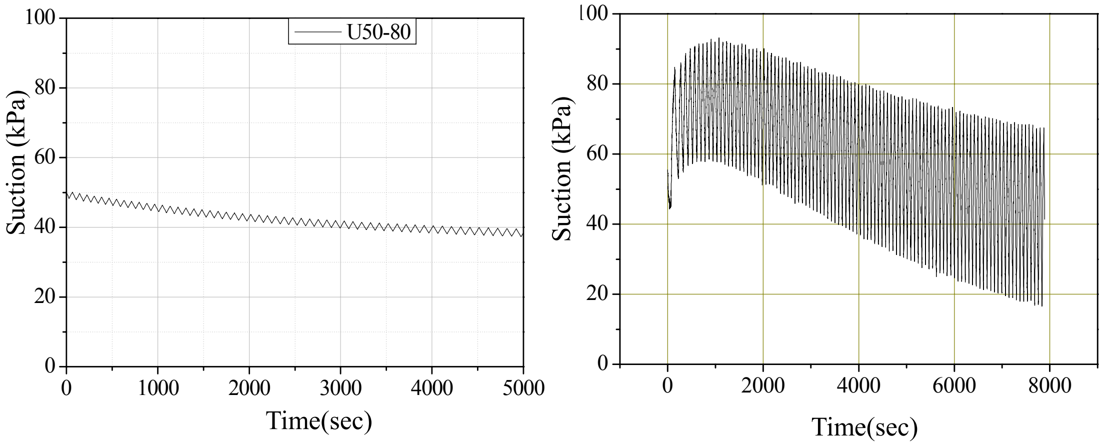

(a)

(b)

Figure 4.22 Suction vs. time: (a) simulated results and (b) experimental results

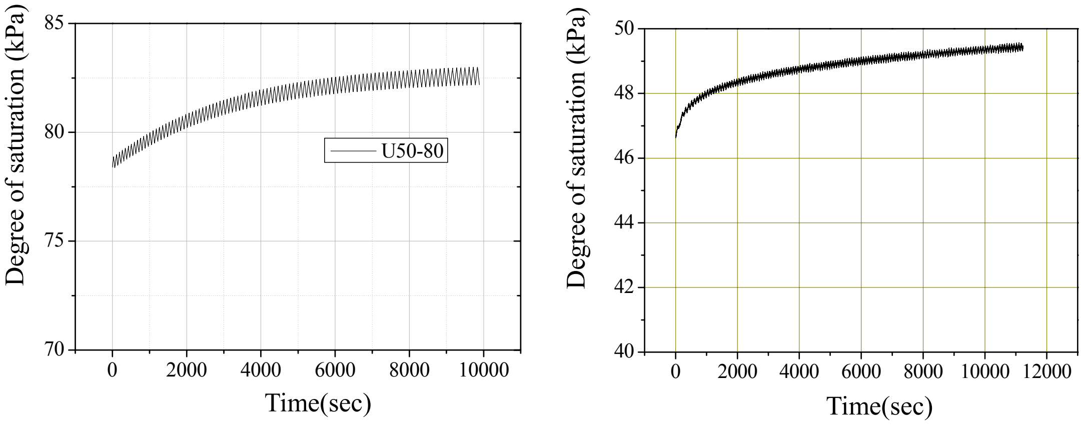

(a)

(b)

Figure 4.23 Degree of saturation vs. time: (a) simulated results and (b) experimental results

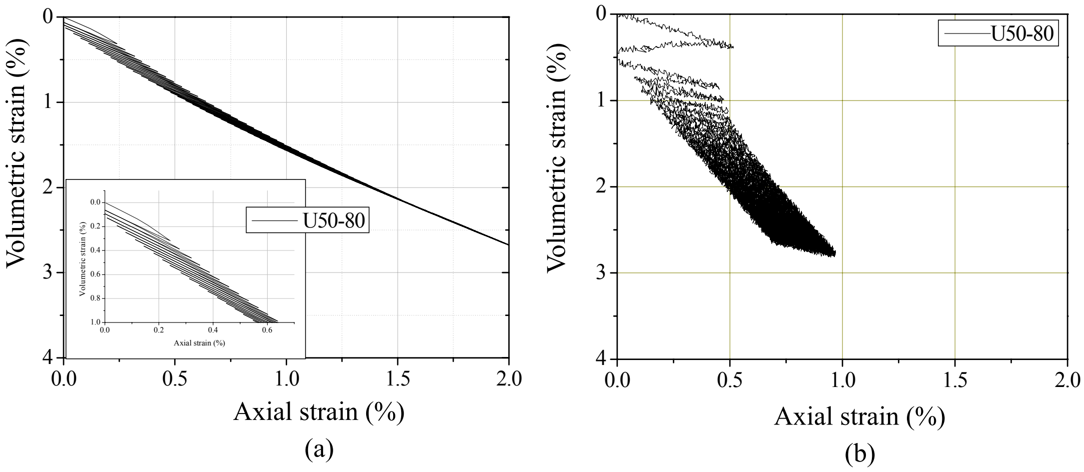

Figure 4.24 Volumetric strain-axial strain relation: (a) simulated results and (b) experimental results

Finally, the results for the case in which the initial suction is 50 kPa and the deviator stress amplitude is 100 kPa are shown in Figures 4.25~4.30. The failure line is reached after 50 cycles.

Figure 4.25 shows the stress-strain relationships for simulation and for the experiment. It can be seen that the stress-strain loops get closer to the previous loops with an increasing number of cycles. Meanwhile, almost no extensive strain has been predicted. Figure 4.26 shows the stress paths for this case. The figure shows that due to the application of higher deviator stress amplitude, the sample reaches the failure line after 50 cycles.

The changes in the pore water pressure and the pore air pressure are shown in Figure 4.27. In the experimental results, it can be observed that the amplitude of the pore water pressure is very large compared to the changes in pore air pressure. Subsequently, high suction amplitude can be observed in the experimental results, as shown in Figure 4.28.

Figure 4.29 shows changes in the degree of saturation with time. It can be seen that the degree of saturation increases with cyclic loading under undrained conditions for water and air. The reason is that, as Figure 4.30 shows, the volumetric strain decreases with time.

From the above analyses at P^C=50 kPa, it can be seen that with an increase in deviator stress amplitude, the number of load cycles needed to reach the failure line decreases. Meanwhile, changes in the pore pressures are greater for the case in which the large deviator stress amplitude is applied. In addition, when a higher level of stress amplitude is applied, a larger the volumetric strain is produced.

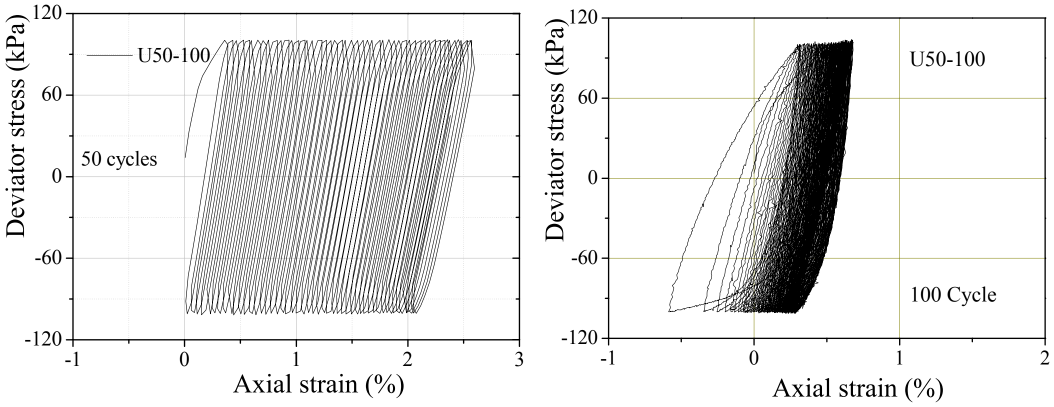

(a) (b)

Figure 4.25 Deviator stress-axial strain relations: (a) simulated results and (b) experimental results

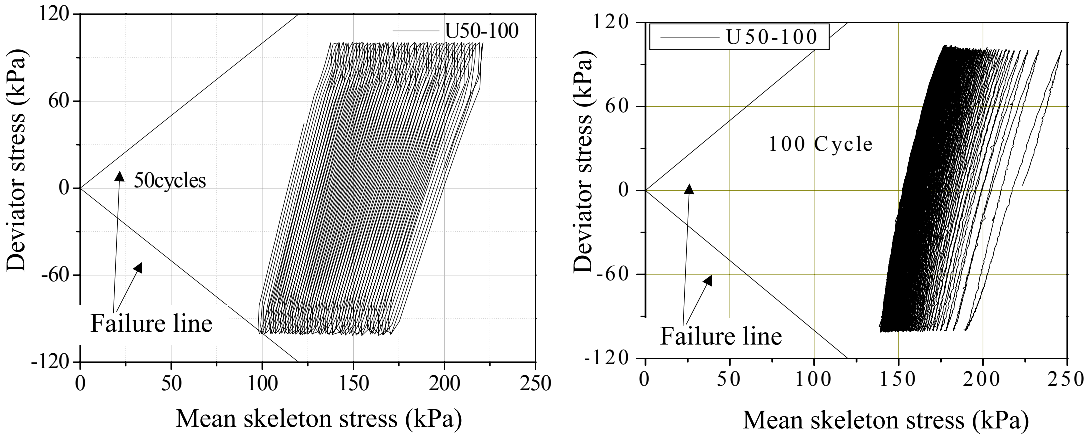

(a) (b)

Figure 4.26 Stress paths: (a) simulated results and (b) experimental results

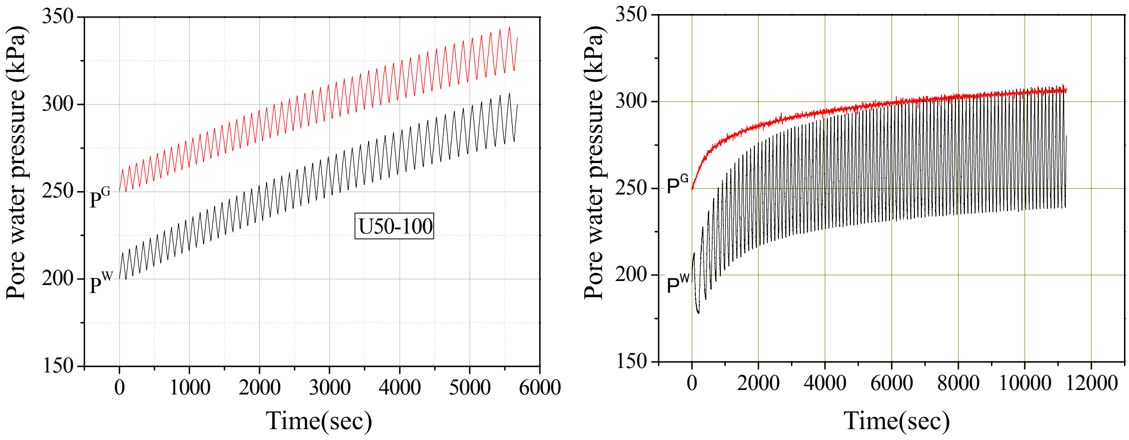

(a) (b)

Figure 4.27 Pore pressure vs. time: (a) Simulated results and (b) experimental results

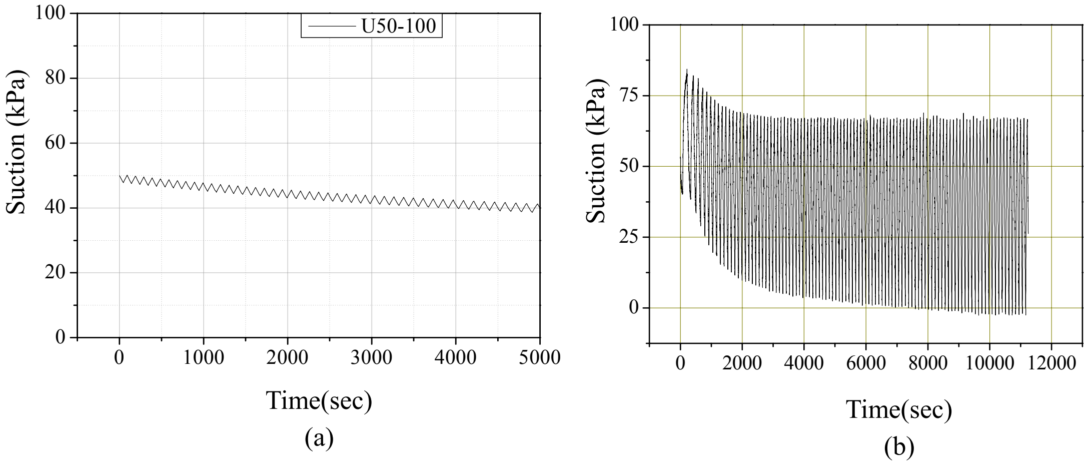

Figure 4.28 Suction vs. time: (a) simulated results and (b) experimental results

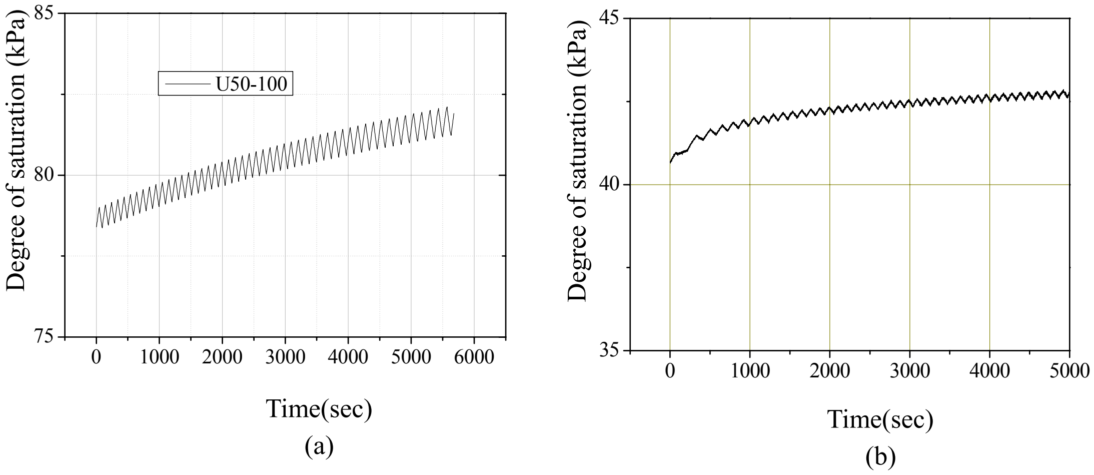

Figure 4.29 Degree of saturation vs. time: (a) simulated results and (b) experimental results

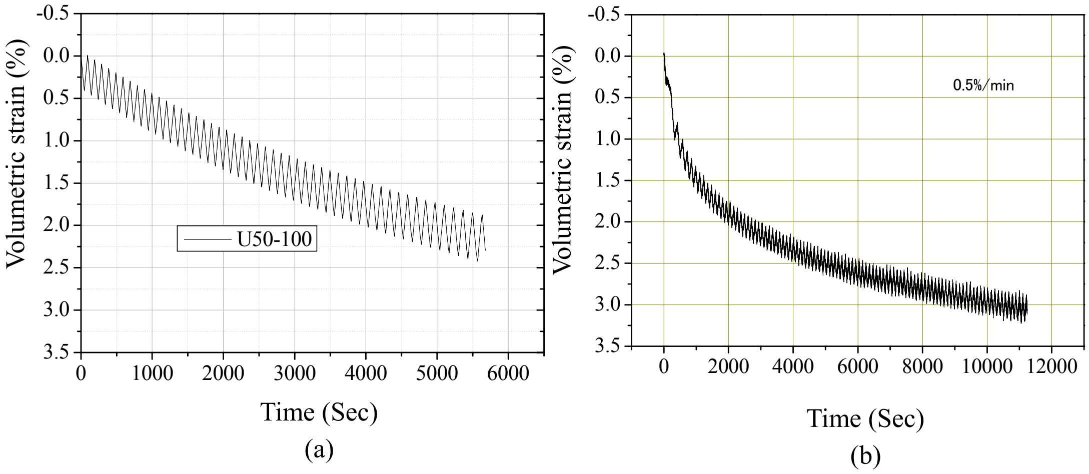

Figure 4.30 Volumetric vs. time: (a) simulated results and (b) experimental results

4.3.3 Effects of Suction on the Cyclic Behavior

In this section, the effect of the initial suction on the cyclic behavior of the unsaturated soil is summarized based on simulations.

From the results, axial strain generated with the same stress amplitude is observed. In the case U0-40, the axial strain is still less than 0.5% after 150 cycles, while it reaches almost 1% for case U50-40 after 100 cycles.

Then, the numbers of cycles needed to reach the failure line are compared. For case U50-80, the number is more than 100, while it is 50 cycles for case U0-80. With a stress amplitude equal to 100 kPa, failure line was reached after 29 cycles in the saturated case, while 100 cycles were required for the unsaturated case.

According to the above comparisons between the cases with the same deviator stress amplitude and but different levels of initial suction, it can be seen that the unsaturated sample (P^C =50 kPa) exhibited a stiffer response and higher strength than the saturated samples.

4.4 Summary

In chapter 4, three-dimensional multiphase numerical simulations of the cyclic triaxial tests on unsaturated soil have been conducted using the proposed elasto-viscoplastic model. Using the multiphase finite element method, the cyclic behaviors of unsaturated soil under undrained conditions for water and air were reproduced.

From the simulation of the experimental results of unsaturated soil, the proposed multiphase analysis method can be applicable to analyze the cyclic behaviors of unsaturaetd soil, such as change of strain, pore-air pressure, pore-water pressure, degree of saturation and volumetric strain, under undrained conditions for water and air. The prediction indicates, however, that the further research is necessary from the quantitative point of view. The predicted axial strains for all the cases, for example, are larger than that of the experimental results.

It has been shown that the unsaturated sample exhibited stiffer response and higher strength than the sample with low suction. As the stress amplitude increased, the number of cycles needed to reach failure line decreased.

Chapter 5

ELASTO-VISCOPLASTIC CONSTITUTIVE MODEL FOR SWELLING UNSATURATED BENTONITE

5.1 Introduction

Expansive soil is found in many parts of the world, particularly in semi-arid regions. Expansive soil (e.g., bentonite or bentonite mixtures) undergoes huge volumetric changes when exposed to water. The heaving of foundations is one of the serious consequences of lightly loaded structures founded on expansive soils. Under displacement-confined conditions, expansive soil will exhibit considerable swelling pressures, which results in serious damage to buildings and other structures. Therefore, it is necessary to have an advance understanding of the mechanical behavior of this type of material.

Many attempts have been made in the past to understand the swelling mechanism of expansive soils. Volume change in clay is due to the clay-water-cation interaction (Bolt 1956). The Gouy-Chapman diffuse double layer theory (Gouy 1910; Chapman 1913) has been the most widely used approach to relate clay compressibility to basic particle-water-cation interaction (Olson and Mesri 1970; Mesri and Olson 1971; Marcial et al. 2002). As shown in Figure 5.1, the swelling of bentonite is due to the absorption of water molecules into the interlayers. The bonding force between negative charge the surface and interlayer cations is lower than the interaction force between the interlayer cations and water molecules. Consequently, the gap between layers is widened as the interlayer cations attract the water molecules. When the interaction between the interlayer cations and water molecules reaches its limit, the swelling stops.

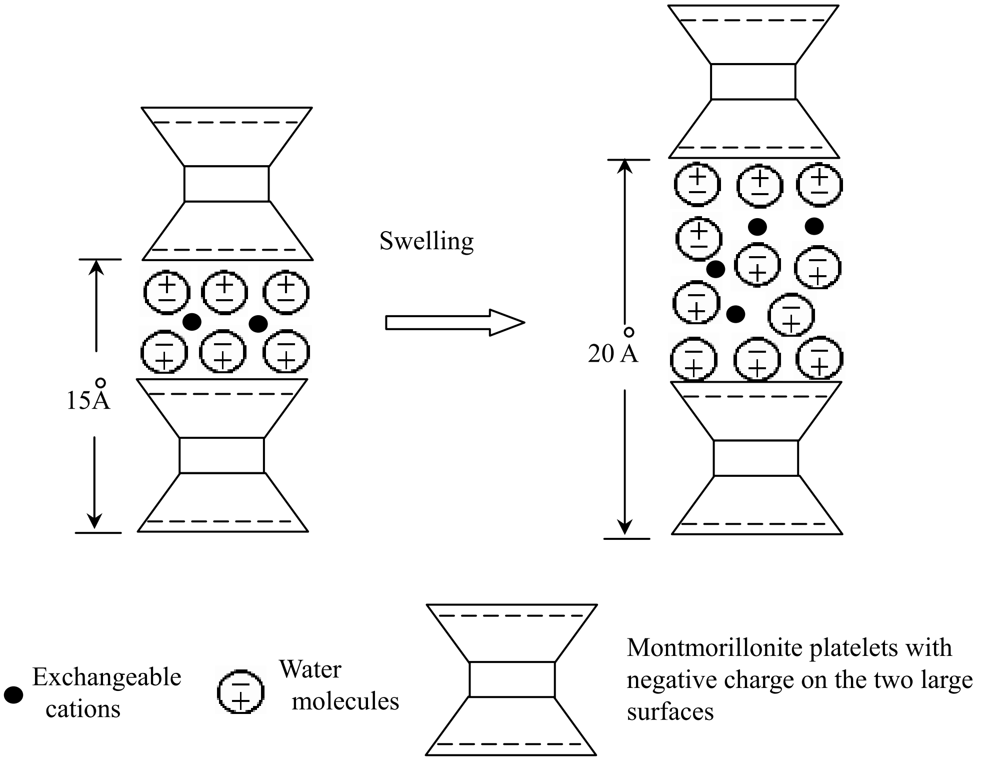
Swelling
15Å
20 Å
Exchangeable cations
Water molecules
Montmorillonite platelets with negative charge on the two large surfaces

Figure 5.1 The swelling structure of montmorillonite (Kurahayashi 1980)

During the last few years, a number of experimental and theoretical research works have been carried out on bentonite and bentonite-soil mixtures. A relationship between swelling deformation and the distance between two montmorillonite layers was proposed (Komine H. 1996). Sridharan and Choudhury (2002) proposed a swelling pressure equation for Na-montmorillonite while analyzing the compression data of slurred samples of montmorillonite reported by Bolt (1956). However, some researchers (Mitchell 1993; Tripathy, Sridharan and Schanz 2004) have shown that very little information is available on the use of the diffuse double layer theory for the determination of the swelling pressure of compacted bentonite. In addition, the microstructure of compacted expansive clays has been studied by Push (1982), who observed a double structure made up of clay aggregates and large macrostructure pores. Gens and Alonso (1992) presented a conceptual basis of a model for expansive soils. And several numerical model have also been proposed to simulate expansive soil (Alonso et al. 1991, 1999, and 2000) based on the elastoplastic theory. According to their theory, two levels are distinguished for the structure, (1) a microstructural level that corresponds to the active clay minerals and their vicinity and (2) a macrostructural level that accounts for the larger structural soil arrangements. The microstructure, namely, the swelling domain that expands when hydrated, is thought to be water-saturated even at large levels of suction levels. In contrast, the macrostructure is assumed to be unsaturated when subjected to suction, and its behavior may be described by conventional frameworks for unsaturated soils. In addition, a theoretical model has been proposed by Shuai and Fredlund (1998) to describe the volume changes during various oedometer swell tests.

The fully experimental study of expansive soil present very significant challenges because the experiments need cover large suction range. An experiment has been carried out on highly compacted bentonite by Lloret et al. (2003). The swelling pressure tests on compacted bentonite have been conducted by some researchers (Pusch 1982; Kanno and Wakamatsu 1992; Komine and Ogata 1996).

In this chapter, an elasto-viscoplastic swelling model for unsaturated bentonite is developed based on the elasto-viscoplastic model for unsaturated soil. An internal variable H, which controls the growth of absorption of water into the clay interlayer, is introduced to describe the large volumetric expansive behavior of the microstructure. This model includes the effects of suction and swelling effect into the hardening parameter, and a van Genuchten type of soil water characteristic curve is adopted as the constitutive equation between suction and degree of saturation. Using the proposed model, the swelling behavior of bentonite has been simulated with the finite element method. This model can also simulate the swelling process of bentonite in the wetting process. By adopting parameter γ, this model can also reflect the effects of initial density and water content on the swelling behavior.

5.2 Elasto-viscoplastic Constitutive Model for Unsaturated Swelling Soil

An elasto-viscoplastic model for unsaturated soil has been presented in Chapter 2. This model takes the suction effect into the constitutive model, which can describe the collapse behavior of unsaturated soil caused by a decrease in suction. As shown in Chapter 3, the three-dimensional numerical results show that using this model, the behavior of unsaturated soil, such as the changes in pore air pressure, pore water pressure, and volumetric strain, can be simulated well with this model. However, this model can predict the viscoplastic volumetric swelling phenomenon during the wetting process. To reproduce the swelling phenomenon caused by the clay particles, such as Montmorillonite particles, the elasto-viscoplastic constitutive model for unsaturated soil is extended to be able to reproduce the volumetric swelling. In the present model, a swelling equation is proposed to describe the viscoplastic volumetric swelling. Meanwhile, in order to reflect the compacting-like phenomena caused by the swelling of the microstructure, the microstructural swelling is introduced to the model.

5.2.1 Model Assumptions

In order to carry out a multiphase analysis of unsaturated expansive soil, two levels of structures are considered. In the present study, the following are assumed:

1. The behavior of the macrostructure of bentonite includes the normal behavior of unsaturated soil. The initial suction level and the SWCC being considered in this paper stand for those of macrostructural behavior.
2. Assumed as a special viscoplastic stretching tensor, the microstructural swelling is introduced into the total stretching tensor in addition to the elasto-viscoplastic stretching tensor for the macrostructure.
3. In addition to the effect of suction, the effect of internal compaction caused by the microstructural swelling is introduced in the constitutive equation as shrinkage or the expansion of the yield surface and the overconsolidation boundary surface.

In the present model, it is assumed that the strain rate tensor consists of the elastic stretching tensor D_{ij}^{e}, the viscoplastic stretching tensor D_{ij}^{vp}, and the additional viscoplastic stretching tensor $D_{ij}^{vp(s)}$, caused by the microstructural swelling. The total stretching tensor D_{ij} is defined in the following equation:

$$D_{ij} = D_{ij}^{e} + D_{ij}^{vp} + \frac{1}{3}\delta_{ij} D_{kk}^{vp(s)} \tag{5.1}$$

where D_{ij}^{e} is the elastic stretching tensor given by a generalized Hooke type of law, determined by Equation (2.17).

5.2.2 Swelling Equation for Interparticles

From the experimental results on bentonite (Komine and Ogata 1996; Push 1982), the swelling phase is followed by an asymptotic tendency towards a constant final value. In this model, the following evolutional equation is proposed to describe the viscoplastic volumetric swelling of the swelling domain:

$$\begin{aligned} D_{kk}^{vp(s)} &= -\dot{H} \\ \dot{H} &= B(A - H) \end{aligned} \tag{5.2}$$

where H is an internal variable that describes the growth in the obsorption of water into the clay particles, and A and B are material parameters.

Figure 5.2 shows the swelling equation curves at various values for parameters A and B. It can be seen that A is a parameter for the potential of absorption of water, and B is a parameter which controls the evolution rate of H.

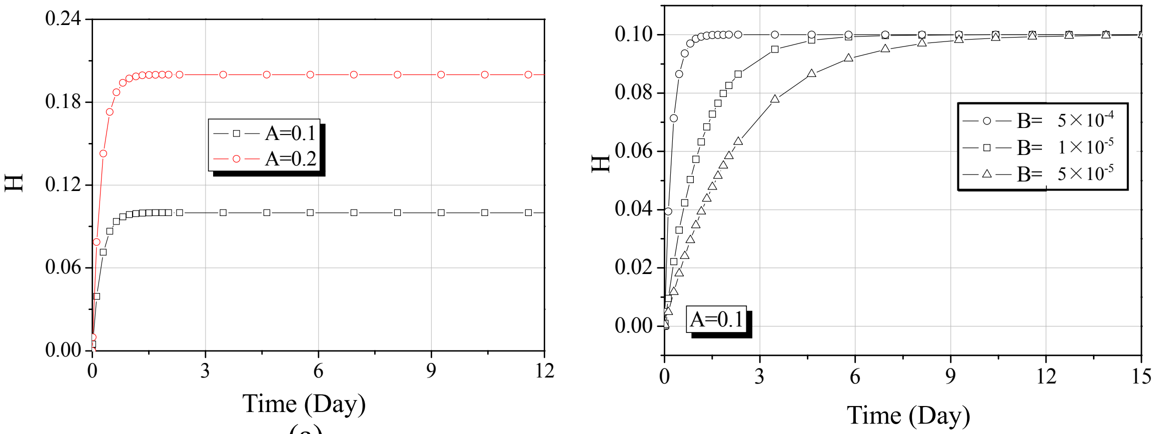

(a)

(b)

Figure 5.2 Swelling equations with different parameters for A and B

5.2.3 Hardening Rule Including Swelling Effect

In Equation (5.1), D_{ij}^{vp} is the viscoplastic stretching tensor, which is determined by the model in Chapter 2. As mentioned in Equations. (2.11) and (2.16), an overconsolidation boundary surface f_b and static yield function f_y are defined. σ'_{mb} of σ'_{my} are values which control the size of f_b and f_y. According to the elasto-viscoplastic theory (Kimoto and Oka 2005), and considering the suction effect, the hardening rule are defined as follows:

$$\sigma'_{mb} = \sigma'_{ma} \exp\left(\frac{1+e}{\lambda-\kappa}\varepsilon_{kk}^{vp}\right)\left[1+S_I \exp\left\{-S_d\left(\frac{P_i^c}{P^c}-1\right)\right\}\right] \tag{5.3}$$

$$\sigma'^{(s)}_{my} = \frac{\sigma'^{(s)}_{myi}}{\sigma'_{mai}}\sigma'_{ma} \exp(\frac{1+e}{\lambda-\kappa}\varepsilon_{kk}^{vp})\left[1+S_I \exp\left\{-s_d\left(\frac{P_i^c}{P^c}-1\right)\right\}\right] \tag{5.4}$$

with the absorption of water into the interlayers, apparent volume of bentonite particles increases. In fact, the distance between two platelets increases from 15 Å to 20 Å (Figure 5.1). With the scanning electron microscope, as shown in figure 5.3, the SEM image of the wetting process of the bentonite has been reported by Komine and Ogata (2004), in which the bentonite content is 100% mass percent. It can be seen that the macro voids are finally filled up by the volume increase of bentonite.

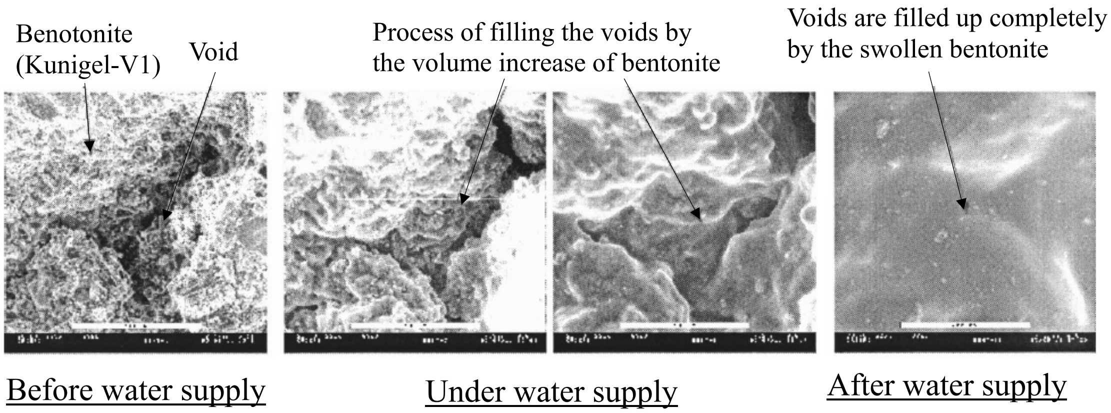
Benotonite
(Kunigel-V1)
Void
Process of filling the voids by the volume increase of bentonite
Voids are filled up completely by the swollen bentonite
Before water supply
Under water supply
After water supply

Figure 5.3 SEM image of wetting process of bentonite (Komine and Ogata 2004)

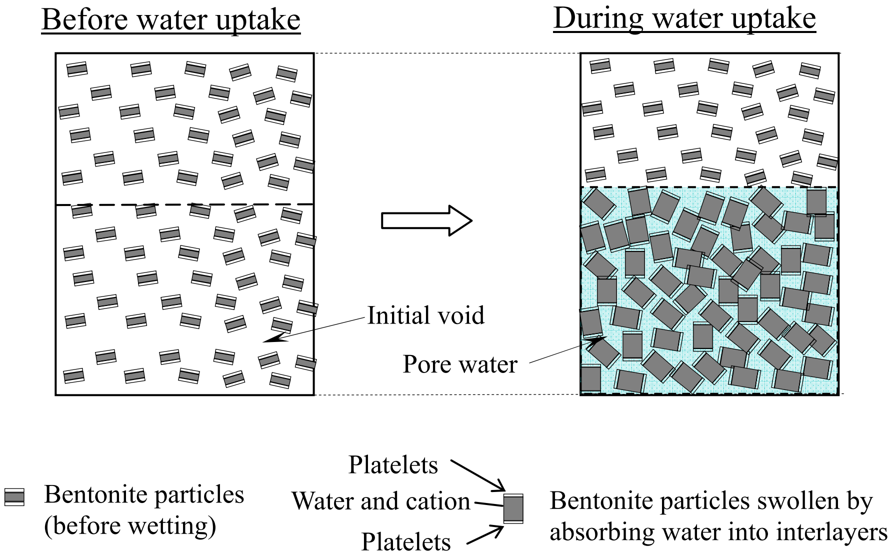
Before water uptake
During water uptake
Initial void
Pore water
Bentonite particles
(before wetting)
Platelets
Water and cation
Platelets
Bentonite particles swollen by
absorbing water into interlayers

Figure 5.4 Process of swelling with deformation restricted

Figure 5.4 illustrates the swelling process in the case the swelling deformation is restricted. From Fig. 5.4, it can be found that with the wetting, the void ratio of the macrostructure is gradually packed by the swollen Montmorillonite particles when the swelling deformation is restricted. As a result, the sample becomes stiffer and with higher strength, which is similar with the soil being highly compacted. Hereafter, we called the phenomenon as "internal compaction effect", which is different with traditional compaction in changes of water content. In the present study, this internal compaction effect is expressed as expansion of overconsolidation boundary surface, the static yield surface as following:

$$\sigma'_{mb} = \sigma'_{ma} \exp\left(\frac{1+e}{\lambda-\kappa}\varepsilon_{kk}^{vp*}\right)\left[1 + S_I \exp\left\{-S_d\left(\frac{P_i^c}{P^c}-1\right)\right\}\right] \tag{5.5}$$

$$\sigma_{my}^{'(s)} = \frac{\sigma_{myi}^{'(s)}}{\sigma_{mai}^{'}} \sigma_{ma}^{'} \exp(\frac{1+e}{\lambda-\kappa} \varepsilon_{kk}^{vp*}) \left[1 + S_I \exp\left\{ - S_d \left(\frac{P_i^c}{P^c} - 1 \right) \right\} \right] \tag{5.6}$$

where ε_{kk}^{vp*} is the viscoplastic volumetric strain including the special swelling effect into account which is defined as

$$\varepsilon_{kk}^{vp*} = \varepsilon_{kk}^{vp} + \gamma |H| \tag{5.7}$$

where, γ is adopted to reflect the percentage of swelling viscoplastic strain considered, which varies from 0 to 1. γ being equal to 0 means that the swelling viscoplastic strain does not affect the expansion or shrinkage of the overconsolidation boundary surface and the static yield boundary surface, while γ being equal to 1 means that all levels of viscoplastic swelling volumetric strain have an effect on expansion or shrinkage the of the boundary surface.

5.3 Simulation of Swelling Pressure Tests

An eight-node quadrilateral isoparametric element with a reduced Gaussian(2 × 2) integration (see Figure 5.5) is used for the displacement in order to eliminate shear locking as well as to reduce the appearance of the spurious hourglass mode. The pore pressures values for air and water are defined by a four-node quadrilateral isoparametric element. As shown in Figure 5.6, the initial thickness of the soil sample is 0.02 m with ten elements, the bottom of which is set to be permeable for water and air by assuming that the water pressure at the bottom is -10 kPa and the air pressure keeps 0 kPa. The other boundaries are assumed to be impermeable to water and air. The time increment is set to be 600 seconds when there are any elements still swelling. Otherwise, it is 1200 seconds.

The displacements in both X and Y directions at the top and the bottom are fixed, while the displacements are fixed only in X direction for other boundaries. The initial conditions and the material parameters for the analyses are shown in Table 5.1. These parameters are measured for Kunigel GX bentonite sample. The initial suction, which is the macrostructural suction, is assumed to be 100 kPa for all the analyses.

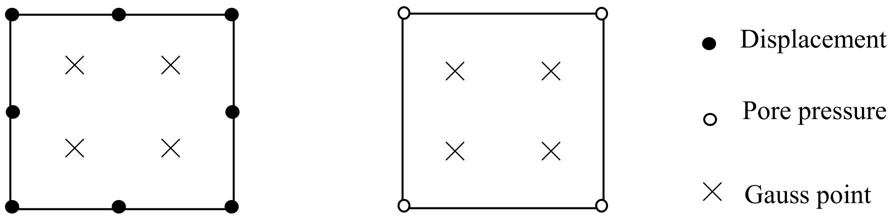

Figure 5.5 Isoparametric elements for the soil skeleton and the pore pressure

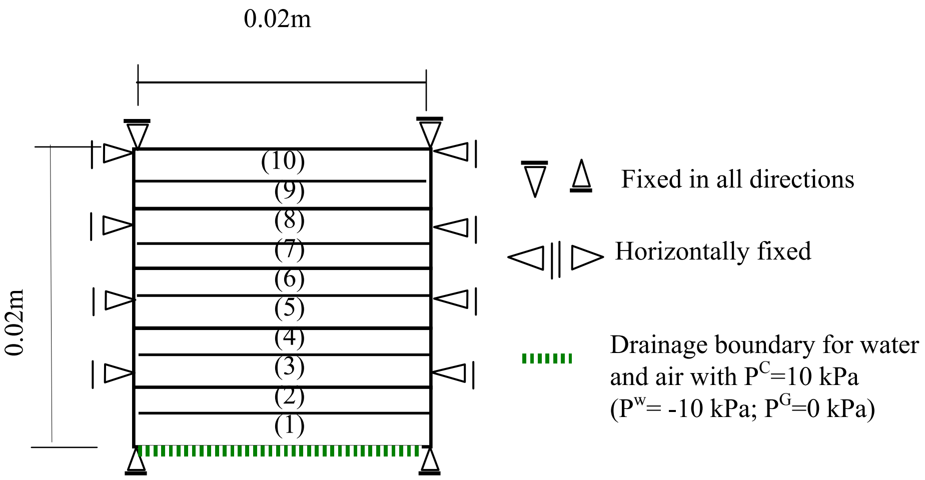

Figure 5.6 Finite element mesh and boundary conditions

Table 5.1 Initial conditions for the simulations

Initial suction	P^c (kPa)	100
Initial void ratio	e_0	0.66
Initial saturation	s^w (%)	69.98
Initial water pressure	P^w(kPa)	-100
Initial air pressure	P^g(kPa)	0

5.3.1 Swelling Pressure with Wetting Process

The wetting process is shown in Figures. 5.7 and (5.8). Figure 5.7 shows the changes in the degree of saturation for each element with wetting. The decreas in suction for every element with wetting is shown in Figure 5.8. In this analysis, it is assumed that each element starts to swell when the degree of saturation reach a given value. From figure 5.8, it can be seen that the degree of saturation of the elements, starting with the element at the bottom, reaches the onset saturation for swelling element by element. Consequently, the swelling starts from the bottom element and moves upwards, element by element. Accordingly, the decrease in suction, with wetting, also starts from the bottom element and move upwards, as shown in Figure 5.8.

As mentioned previously, the predictions of the swelling pressure are affected by the following parameters: the parameter A, and γ, permeability, and the initial swelling saturation. The first two parameters are newly introduced to the model and control the swelling equation. The last two parameters control the time needed to complete the swelling process. In the next sections, the effects of these parameters are investigated.

Table 5.2 Material parameters

Elastic shear modulus	G_0(kPa)	3.74×10^{4}
Initial yield stress	σ'_{mbi} (kPa)	100
Swelling index	κ	0.078
Compression index	λ	0.117
Viscoplastic parameter	m'	95.4
Viscoplastic parameter	C_1(1/s)	9.47×10^{-18}
Viscoplastic parameter	C_2(1/s)	9.47×10^{-18}
Stress ratio at critical state	M^*_m	0.4736
Suction parameter	S_I	0.5
Suction parameter	S_d	0.25
Structural parameter	σ'_{maf} (kPa)	83
Structural parameter	β	5.0
van Genuchten parameter	α (1/kPa)	0.015
van Genuchten parameter	n	1.517
Permeability of water at s_r=1	k^W(m/s)	2.0×10^{-13}
Permeability of gas at s_r=0	k^G (m/s)	1.3×10^{-11}
Shape parameter	a	3.0
Shape parameter	b	2.3
Maximum saturation	$s_{\max}$	1
Minimum saturation	$s_{\min}$	0
Expansive parameter	A	0.1
Expansive parameter	B	0.00001
Expansive parameter	γ	0.4
Onset saturation for swelling	(%)	70.5

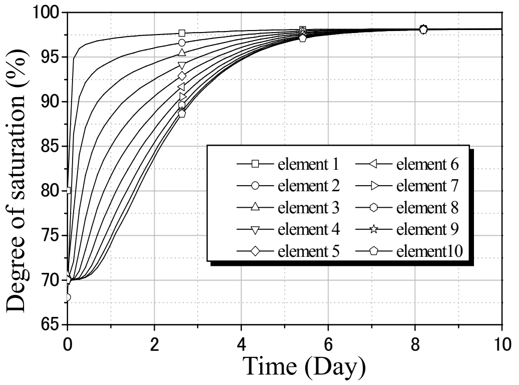

Figure 5.7 Degree of saturation for each element with wetting

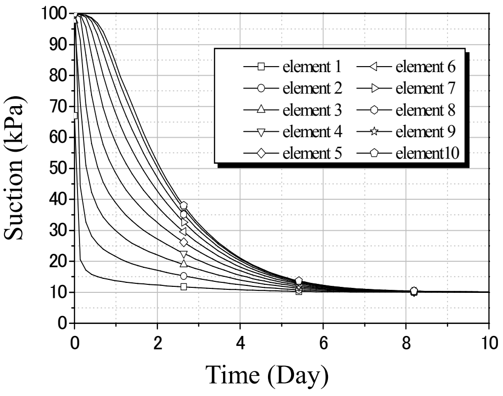

Figure 5.8 Suction for each element with wetting

5.3.1.1 Swelling Pressure with Different Permeabilities

As previously mentioned, the swelling of the sample depends on the degree of saturation, which in turn is strongly affected by the permeability. In this section, the effect of permeability on the swelling pressure is investigated using the proposed model. In these analyses, changes in the permeability of water are examined. The onset saturation for swelling is set to be 75% in all calculations in this section. The remaining soil material parameters are listed in Table 5.2. Figure 5.9 provides the changes in swelling pressure with wetting obtained from the simulations. From Figure 5.9, it is confirmed that permeability k^W delays the time needed for swelling. For higher permeability, the sample starts to swell after a short time. For lower permeability, on the contrary, the sample does not appear to start swelling until a long wetting period has passed.

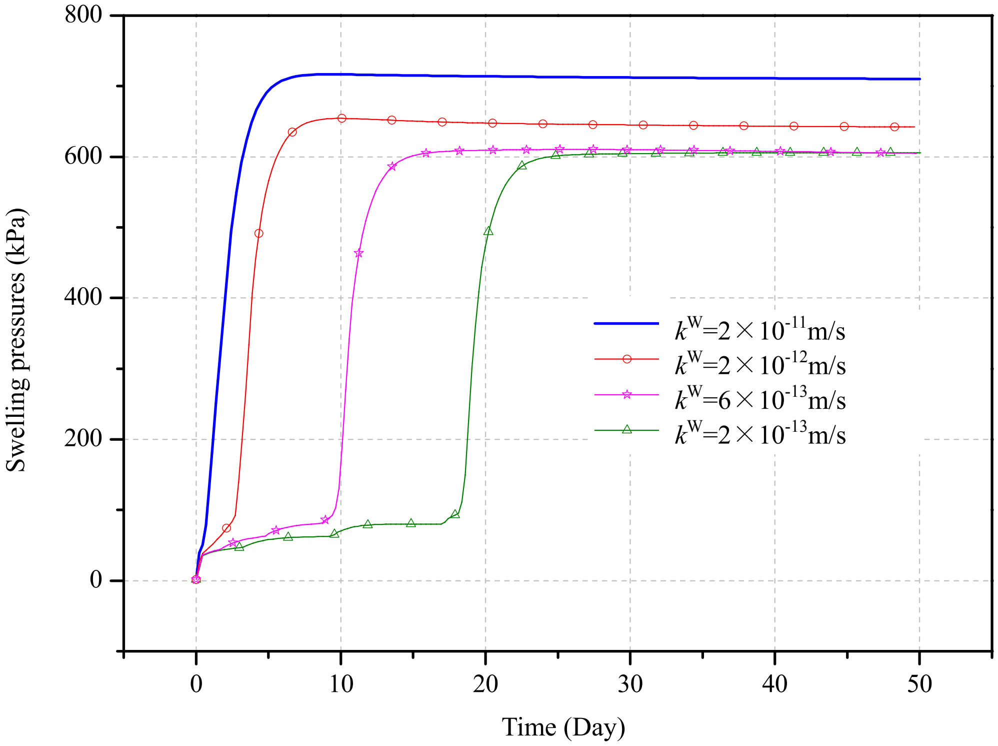

Figure 5.9 Effect of permeability on the swelling pressure

5.3.1.2 Swelling pressure with different onset saturation for swelling

As it is known, the swelling behavior is presented due to the absorption of water into the interlayers. In this model, onset saturation for swelling is assumed to be the degree of saturation from which the microstructure starts to swell. In the previous section, the swelling was assumed to start when saturation is reached 75%. In this section different levels of initial swelling saturation are investigated. The permeability of water is set to be

2.0×10^{-13}m/s, and the remaining parameters are listed in Table 5.2. Six cases are studied with levels of onset saturation for swelling from 70% to 75%.

Figure 5.10 shows the predicted swelling pressure curves at various levels of onset saturations. Similar to the effect of permeability, the decrease in onset saturation for swelling leads to a delay in swelling. For the case in which the onset saturation for swelling is 70%, the swelling starts just after a very short time, because the initial swelling saturation is very close to the initial saturation (69.98%). With an increase in the onset saturation value, a longer wetting period is required for the swelling to begin.

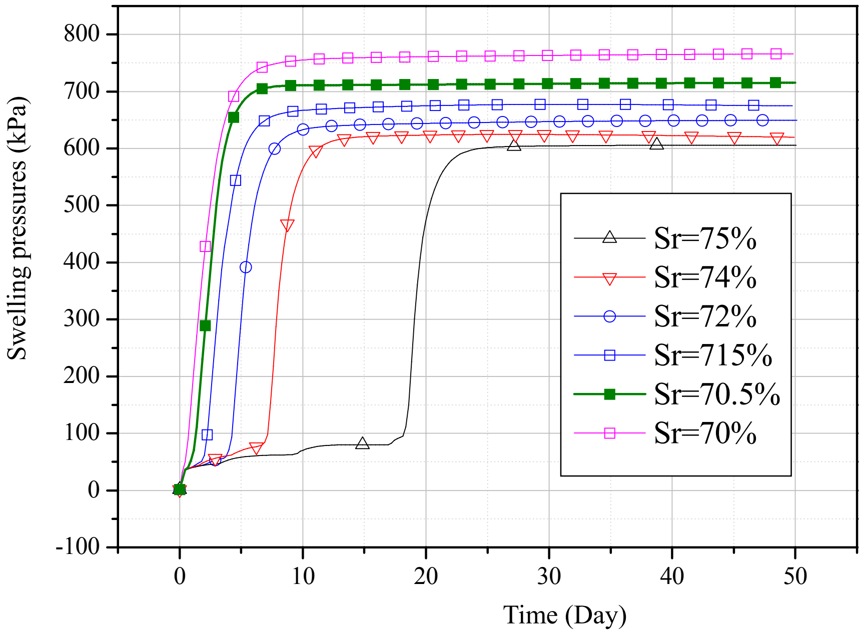

Figure 5.10 Effect of the onset saturation for swelling on the swelling pressure

5.3.1.3 Effect of γ on the swelling pressure

In this section, the effects of parameter γ, which is newly introduced in the model, are studied. Parametric studies on the changes in γ from 0.0 to 1.0 are performed. The other soil parameters are listed in Table 5.2. The simulated results of the swelling pressures during the wetting process with different values for γ are shown in figure 5.11. From this figure, it is seen that parameter γ ($0 \leq \gamma \leq 1$) affects not only the final pressure, but also the shape of the swelling pressure curves. In cases where without or only little parts of viscoplastic swelling volumetric strain ($\gamma < 0.3$) are considered, a time-softening behavior can be observed. However, for the case in which a higher percentage of swelling strain ($\gamma > 0.4$) is considered, time-hardening behavior can be observed. Additionally, it is found that the predicted final swelling pressure increases with an increase in γ; however, the final swelling pressure remains almost constant when $\gamma > 0.5$.

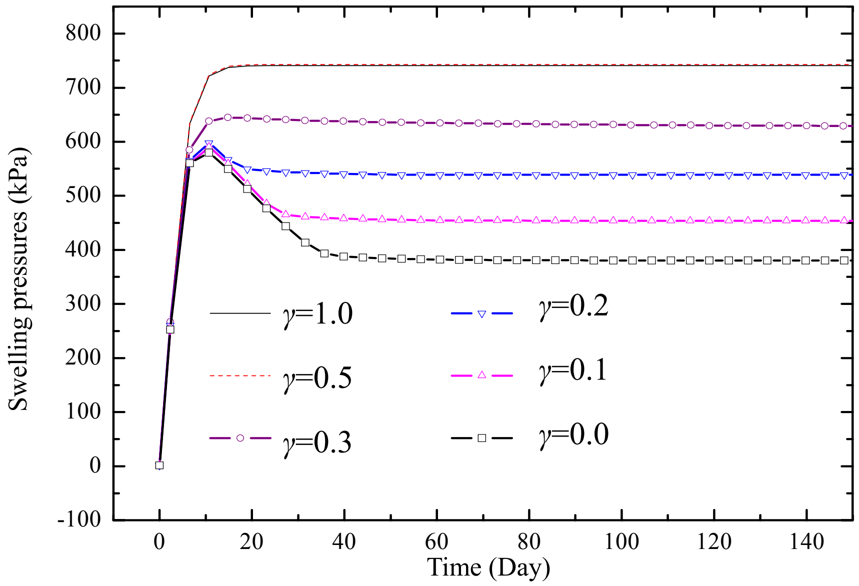

Figure 5.11 Effect of parameter γ on the swelling pressure

According to this elasto-viscoplastic model, viscoplastic strain increments for the overstress type of model depend on the difference between the current stress state and the static stress state. This means that a large difference between the current stress state and $\sigma_{my}^{'(s)}$ will lead to an obvious relaxation. Figure 5.12 presents the changes in $\sigma_{mb}^{'}$ with the wetting process. It can be seen that by considering the viscoplastic swelling strain, as in Equations (5.5) and (5.6), that the value of $\sigma_{mb}^{'}$ increases quickly and reaches a higher value compared to the value of $\sigma_{mb}^{'}$ for which no swelling effect is considered. In the case of a lower percentage of microstructural swelling being considered, we can see that compared with mean skeleton stress $\sigma_{m}^{'}$, $\sigma_{mb}^{'}$ or $\sigma_{my}^{'(s)}$ increase slowly. Therefore, the slow increase in the static yield surface and the quick increase in the mean skeleton stress due to the swelling yield increases of the viscoplastic strain increments. As a result, the relaxation happens and the time-softening behavior could be observed. When significant microstructural volumetric swelling effect are taken into account, e.g. $\gamma > 0.3$, this time-softening behavior can not be observed. It is also found that γ affects the final swelling pressure.

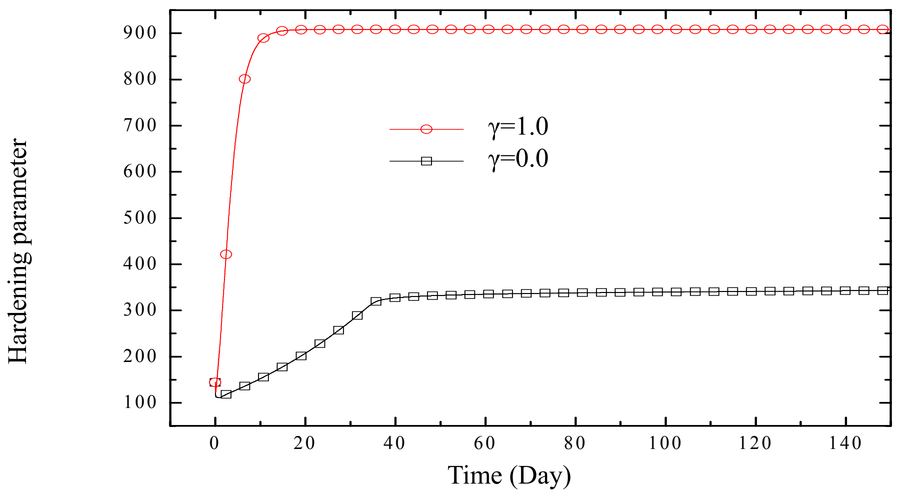

Figure 5.12 Changes in hardening parameter σ'_{mb} with different γ values

5.3.1.4 Effect of *A* on swelling pressure

As mentioned previously, *A* is a material parameter, which represents the potential to absorb water. In this section, the effect of parameter *A* on the final swelling pressure is investigated. The remaining parameters are listed in Table 5.2. Figure 5.13 provides the development of swelling pressure with wetting under different values of parameter *A*. From Figure 5.13, it is found that *A* controls the magnitude of the swelling pressure. It is seen that with larger values for *A* comes higher levels of swelling pressure.

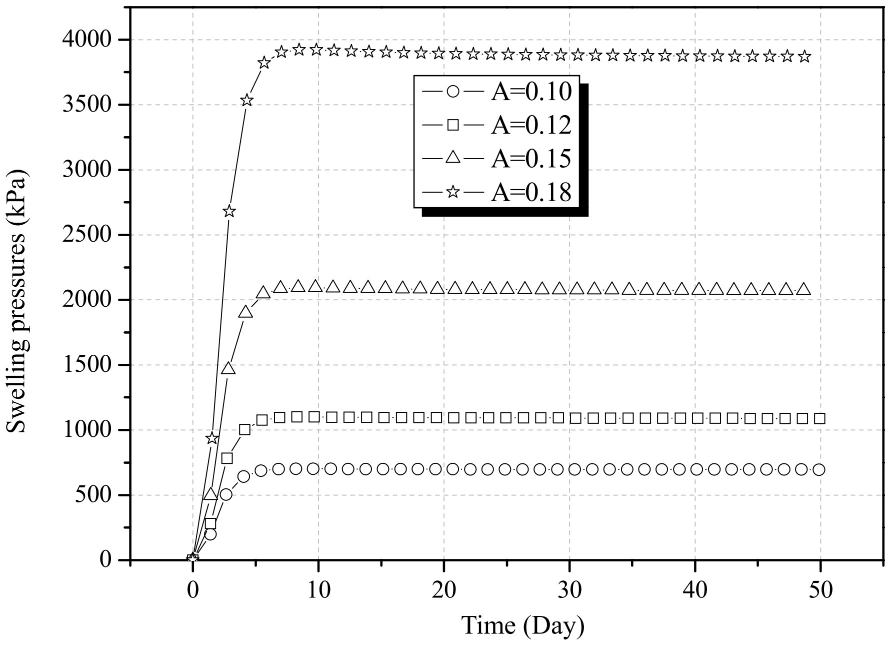

Figure 5.13 Effect of parameter A on the swelling pressure

5.3.1.5 Swelling pressure considering the initial dry density and the water content

In the previous sections, the effects of swelling parameters A and γ on the swelling pressure have been examined. From Figure 5.13, it can be observed that at a given value for γ, the final swelling pressure will increase as parameter A increases. And then, as shown in Figure 5.11, by decreasing the value of γ, the time-softening behavior for the swelling pressure can be simulated. Meanwhile, we can see that the final value for swelling pressure also decreases with a decrease in the γ value even at same value for A, as shown in Figure 5.11. According to the experimental results, we can assume that the swelling potential of the sample is affected both by the type of special minerals, such as montmorillonite and swelling chlorite, etc., and by its concentration. This means that for a soil, the parameter A is affected by the dry density (high mineral concentration).

For the swelling process, it is reasonable to think that the initial water content can also cause some degree of swelling. Figure 5.14 illustrates a comparison between two types of compacted bentonite with different levels of initial water content. As shown in the figure, a certain amount of swelling is seen within the samples with higher levels of initial water content even before the wetting process begins. In this model, parameter γ can be used to reproduce the compacted effect caused by swelling. Therefore, parameter γ can be adopted to reflect the effect of the initial water content. Theoretically, by adopting proper values for parameters A and γ, the effect of dry densities and initial water contents on swelling pressure can be reproduced with this model.

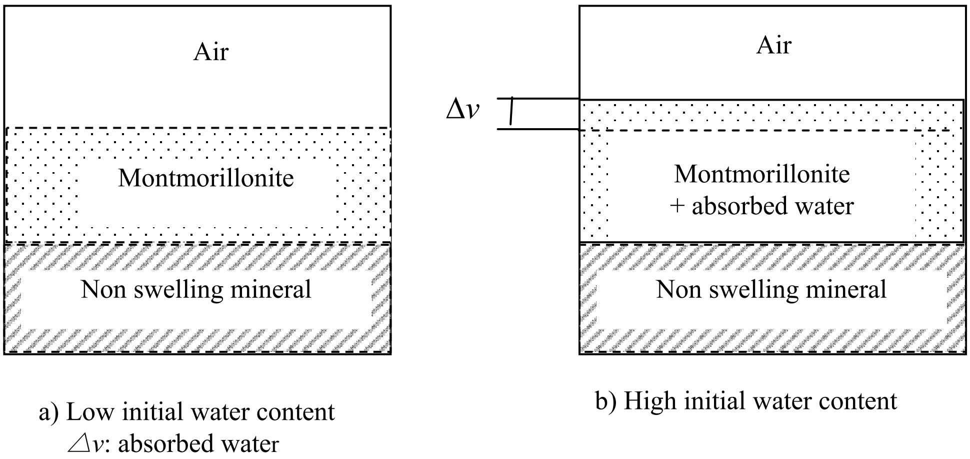

a) Low initial water content
△v: absorbed water

b) High initial water content

Figure 5.14 Comparison of compacted bentonite with different initial water contents

5.3.2 Application to Kunigel GX Bentonite

Swelling pressure tests are conducted for a confined situation in which changes of volume for the specimen are not permitted. Using commercial Kunigel GX bentonite, the swelling pressure of the bentonite has been tested by Ono et al. (2006). The properties of this bentonite are shown in Tables 5.1 and 5.3. As shown in Table 5.4, experiments at different dry densities and initial degrees of saturation were carried out for the bentonite. The experimental results are shown in Figure 5.15. From the experimental results with different dry densities, it is confirmed that the dry density controls the final swelling pressure, which means the higher the dry density of bentonite the higher the final swelling pressure. Meanwhile, it is confirmed that, at a given dry density, initial water content affects the initial part of swelling pressure curves. For the case of lower initial water content (SW1, SW2, and SW3), the swelling pressure increases to a peak value fairly quickly. Then a time-softening phenomenon can be observed. For the cases of high initial water content (SW4, SW5, and SW6) without this type of time-softening behavior, the swelling pressure gradually reaches to the final value.

Table 5.3 Properties of the Kunigel GX

		Sodium bentonite
Density	g/cm^3	2.65
Liquid limit	%	416
Plastic limit	%	21
Plasticity index		395
Activity		8.53
Clay content (<2 μm)	%	51.6

Table 5.4 Experimental cases (Ono, 2006)

Case	Dry density (Mg/m^3)	Water content (%)	Degree of Saturation (%)
Sw1	1.4	6.5	20
Sw2	1.6	6.5	27
Sw3	1.8	6.5	39
Sw4	1.4	29.5	91
Sw5	1.6	21.6	91
Sw6	1.8	15.3	92

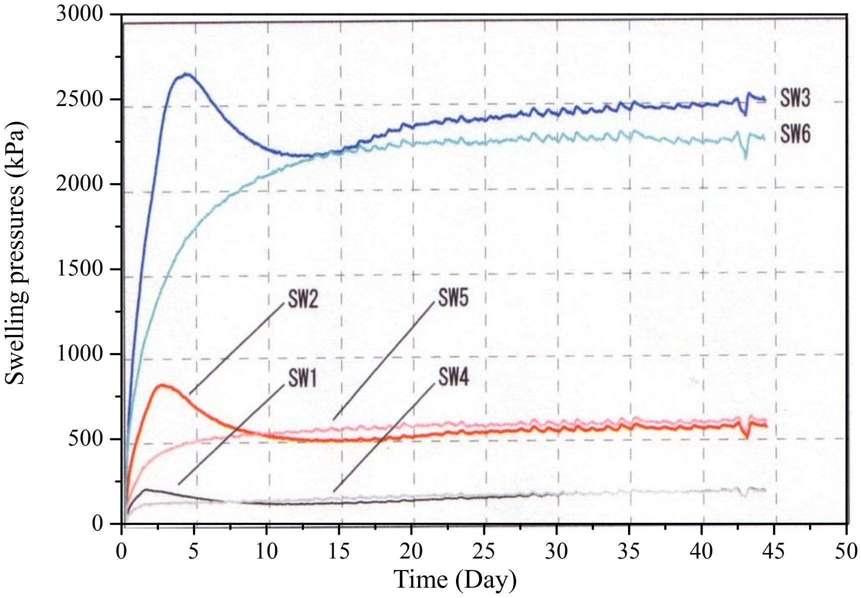

Figure 5.15 Experimental results (Ono et al., 2006)

As discussed in the previous section, by adjusting the parameters A and γ, finite element simulations are carried out to simulate swelling pressure tests with different dry densities and initial water contents. Material parameters A and γ are listed in Table 5.5. The remaining parameters and initial conditions are listed in Tables 5.1 and 5.2. The predicted swelling pressures, with the wetting process, is shown in Figure 5.16. For reference cases SW3 and SW6, with higher initial dry densities, higher A values (0.18 and 0.16) are adopted. For cases with higher initial water content values (SW5 and SW6), a larger γ (0.3) is used to represent the initial hardening effect.

As Table 5.5 shows, a little lower value is adopted for parameter A for high initial water contents (S5 and S6) even though they have the same dry densities. This is because for cases of high initial water contents, some amount of swelling has already taken place before wetting, so the swelling potential should be lower than in samples with lower initial water contents at the same dry densities.

Table 5.5 Parameters for the simulation

Simulation case	A	γ	No. of Exp.
S2	0.12	0.1	SW2
S3	0.18	0.1	SW3
S5	0.10	0.3	SW5
S6	0.16	0.3	SW6

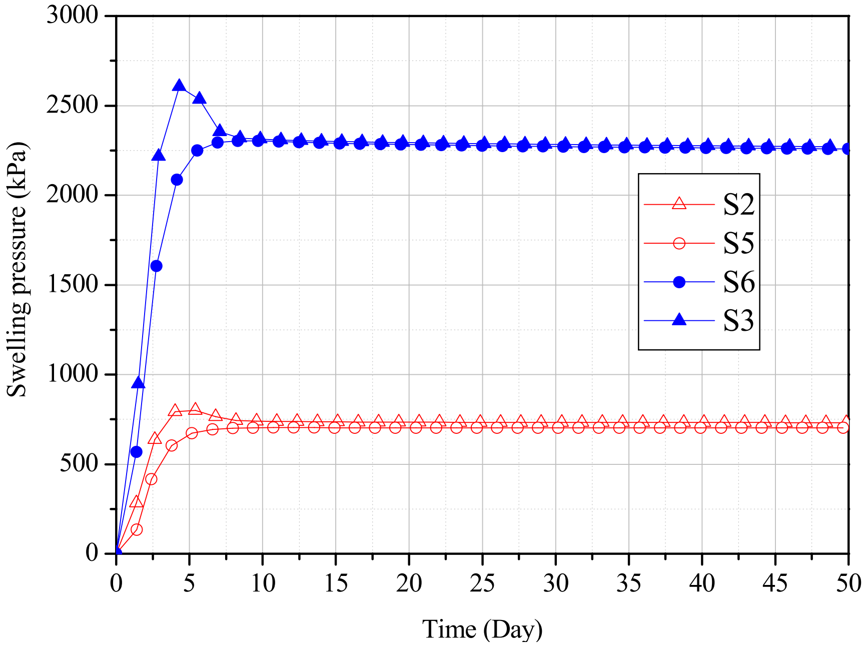

Figure 5.16 Simulated results for swelling pressure

5.4 Summary

In Chapter 5, based on the elasto-viscoplastic constitutive model for unsaturated soil, an elasto-viscoplastic model for unsaturated expansive soil has been proposed. An internal variable H that reflects the growth of absorption of water into interclay is adopted to describe the expansive behavior of microstructures. Due to the absorption of water into the interlayers, apparent volume of montmorillonite particles increases. In restricted swelling deformation condition, this process leads to the decrease of micro void. In the present model, this internal compaction effect is expressed with the expansion of the overconsolidation boundary surface and the static yield surface.

Using the proposed model, one-dimensional FEM analyses were conducted to simulate the swelling pressure. The results show that the proposed model can reproduce the swelling behavior during the wetting process of unsaturated bentonite. In addition, the effects of parameters on the predicted swelling pressure were investigated.

Parameter A and γ are adopted to describe the swelling potential and internal compaction effect of bentonite. The proposed model has been applied to the swelling pressure tests on bentonite (Kunigel GX). Compared with the experimental results, it has been found that the proposed model can well reproduce the effect of dry density and initial water content on swelling pressure.

Chapter 6

NUMERICAL SIMULATION OF SWELLING PRESSURE OF DISPOSAL BARRIERS

6.1 Introduction

Highly expansive soils, such as bentonite are currently considered to be a suitable barrier for isolation of waste, e.g. nuclear, industrial or mining wastes, from surrounding environment due to the low permeability. Due to the swelling properties, cracks that may exist in surrounding soils and rocks can be filled up by the bentonite. In such a problem, according to conventional designs, it is acceptable to assume that the groundwater will eventually saturate the bentonite barriers. Therefore, it is important to evaluate the swelling pressure that bentonite impose on the containers, surrounding soils and rocks due to seepage of groundwater, as well as the long-term stability of the barrier structure itself. It shows that the swelling pressure determination is an important aspect of all high-level radioactive waste disposal projects (e.g. Tripathy, Sridharan and Schanz 2004).

Numerous laboratory swelling tests (Pusch 1982; Gray et al. 1984; Komine and Ogata 1996; Japan Nuclear Cycle Development Institute 1999; Tripathy, Sridharan and Schanz 2004) have been reported on the bentonite. However, these test methods generally involve the use of a conventional one-dimensional oedometer apparatus. Several numerical models of expansive soils (Gens and Alonso 1992; Frendlund and Rahardjo 1993) have been proposed. Two-dimensional finite element analyses are, however, rarely reported. Based on the hydro-chemical formulation, two-dimensional wetting process and the diffusion of cation were studied without considering the swelling effect of bentonite.

An elasto-viscoplastic expansive unsaturated model has been proposed in chapter 5. The proposed model was used to simulate the behaviors of one-dimensional oedometer apparatus tests. Finite element simulation results show that the proposed model can describe the effect of dry density and initial water content effect on swelling pressure. In this chapter, by using this model, two dimensional simulations are carried out to investigate the development of swelling pressure with wetting process. In addition, the long-term safety of structure is also discussed.

6.2 Numerical Simulations

The numerical examples presented in this section exhibit behavior of bentonite buffer in nuclear waste problem. The effects of swelling pressure with wetting by surrounding water on the rock and container structure are investigated. A small example concerning the spreading of swelling phenomena in two-dimensional condition is firstly introduced. As follows, a simplified simulation of nuclear waste barrier is presented. To make a detail investigation on the behaviors of bentonite buffers, simulation with fine buffer layer mesh is carried out. Finally, the multiphase analysis is applied to a two-dimensional nuclear waste barrier problem wetted by the surrounding water. The main material parameters and initial conditions are listed in Table 6.1.

In simulations, the time increment is automatically selected method based on the saturation and swelling state for all the elements. The time increment is set to be 600 s when there are any elements still swelling. When the saturation of one element get close to the onset saturation (<0.1%), the time increment is set to be 1200 s. At the other situation, the time increment set to be 10800 s.

6.2.1 Swelling Behavior of Bentonite

In this section, a simple two-dimensional numerical analysis is carried out to investigate the swelling behaviors of bentonite. The material parameters and initial conditions used in this analysis are listed in Table 6.1. Fig. 6.1 shows the finite element mesh and boundary conditions in the analysis. In the analysis, the displacements on the top and bottom boundary are constrained, in X-direction the movements are fixed for the other two boundaries. Water pressure P^W is assumed to be applied with $P^W =$ -10 kPa on the boundary as shown in Fig. 6.1.

The distributions of mean skeleton stress with wetting are shown in Fig. 6.2. It shows that after 5 hours, the sample starts to swelling to the elements close to the drained boundary. The other element starts to swell after 24 hours. Fig. 6.3 shows the distribution of pore water pressure with swelling. It can be seen that the wetting starts from the drained boundary and reach the full saturation after 24 hours. From the simulation, it can be seen that the proposed constitutive model can reproduce the wetting process. In addition, the swelling process also can be simulated in two-dimensional problem.

Table 6.1 Material parameters and initial conditions for bentonite

Initial suction	P^c (kPa)	100
Initial void ratio	e_0	0.66
Initial saturation	s^w (%)	69.98
Initial water pressure	P^w(kPa)	-100
Initial air pressure	P^g(kPa)	0
Initial Suction	P^c (kPa)	100
Elastic shear modulus	G_0(kPa)	3.74×10^4
Consolidation yield stress	σ'_{mbi} (kPa)	100
Swelling index	κ	0.078
Compression index	λ	0.117
Viscoplastic parameter	m'	95.4
Viscoplastic parameter	C_1(1/s)	9.47×10^{-18}
Viscoplastic parameter	C_2(1/s)	9.47×10^{-18}
Stress ratio at critical state	M^*_m	0.4736
Suction parameter	S_I	0.7
Suction parameter	S_d	0.005
Structural parameter	σ'_{maf} (kPa)	100
Structural parameter	β	0.0
Van Genuchten parameter	α (1/kPa)	0.065
Van Genuchten parameter	n	1.6
Permeability of water at s_r=1	k^W(m/s)	2.0×10^{-13}
Permeability of gas at s_r=0	k^G (m/s)	1.3×10^{-11}
Shape parameter	a	3.0
Shape parameter	b	2.3
Maximum saturation	s_{max}	1
Minimum saturation	s_{min}	0
Expansive parameter	A	0.1
Expansive parameter	B	0.00001
Expansive parameter	γ	0.4
Onset saturation for swelling	(%)	70.5

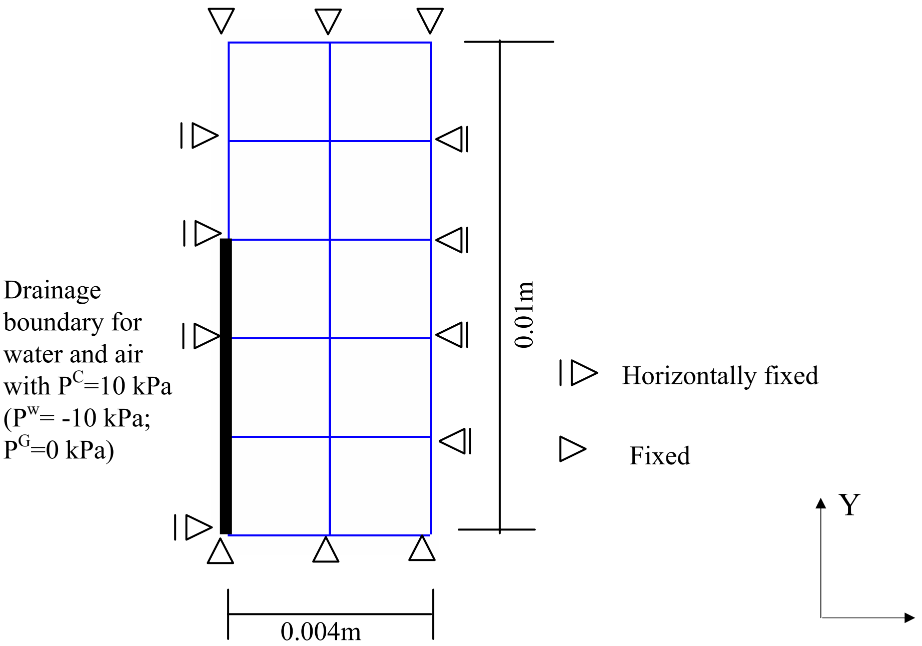
Drainage boundary for water and air with P^C=10 kPa (P^w= -10 kPa; P^G=0 kPa)
0.01m
Horizontally fixed
Fixed
Y
0.004m

Fig. 6.1 Finite element mesh and boundary conditions

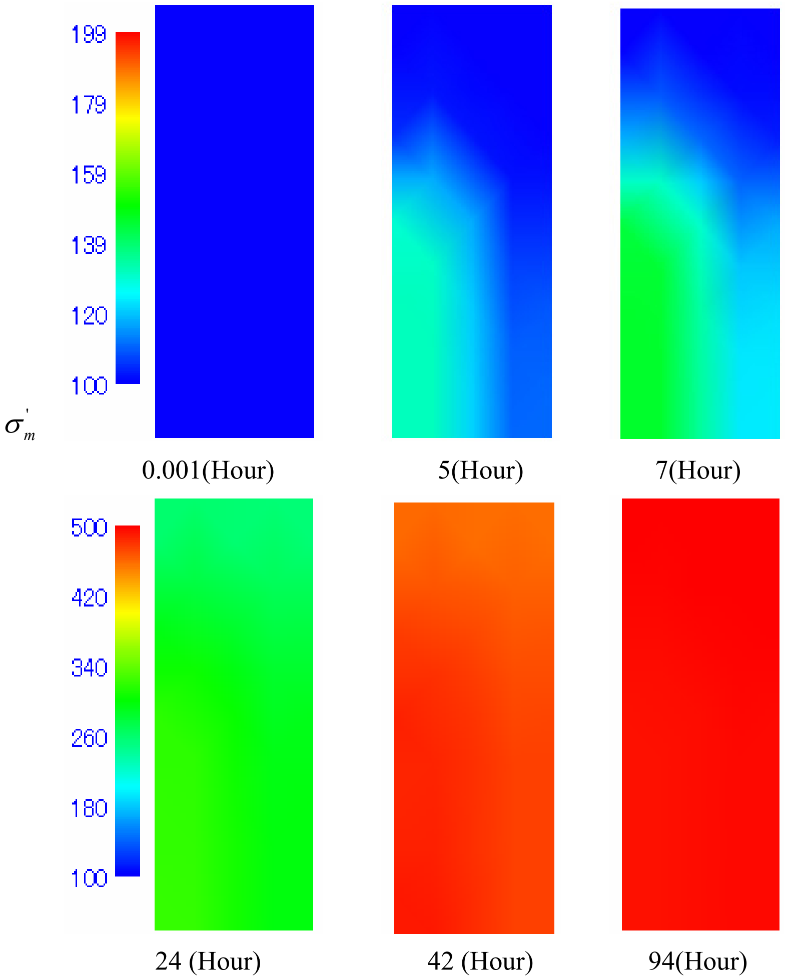

0.001(Hour) 5(Hour) 7(Hour)

24 (Hour) 42 (Hour) 94(Hour)

Figure 6.2 Distribution of mean skeleton stress with wetting (kPa)

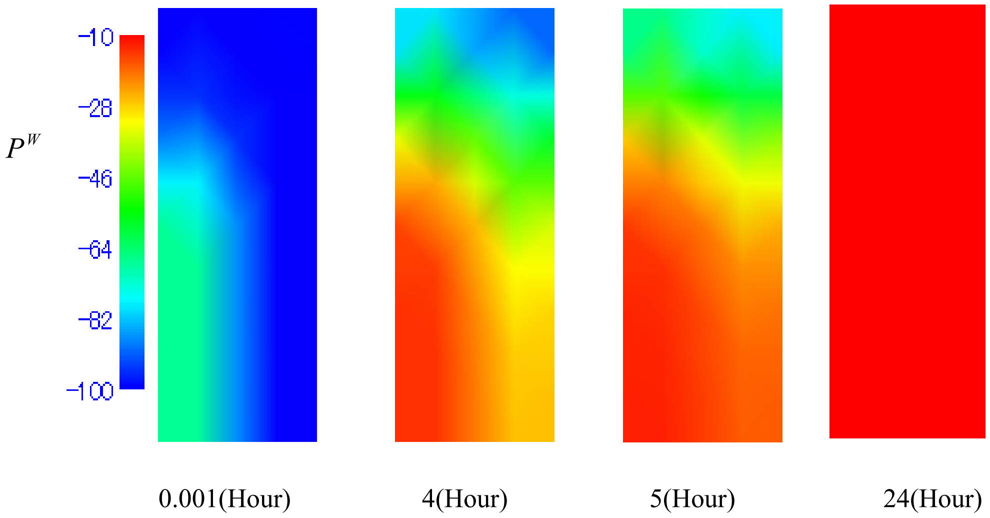

Figure 6.3 Distribution of pore water pressure with wetting (kPa)

6.2.2 A Waste Barrier Example

The second numerical example concerns the 2-dimensional description of the waste barrier problem in which wetting is from surrounding rock. Fig. 6.4 shows the finite element mesh and boundary conditions for the analysis. As the figure shows, the model domain measures 27 m in width and by 20 m in depth. The model has been discretised using 8-node quadrilateral elements and consists of 168 elements and 557 nodes. The size of the model has been reduced by 25% via the assumption of vertical and horizontal symmetry. In the model, there are three kind of materials are used, those are, surrounding rock, bentonite buffer, and waste container. The analysis is simplified by assuming the surrounding rock and the container is a homogeneous. The left and bottom boundaries are set to be drained boundaries with P^W=10 kPa and P^G=0 kPa. The other boundaries are assumed to be impermeable.

Furthermore, a higher permeability of bentonite is adopted by $k^W = 5 \times 10^{-9}$ m/s in the analysis to save the analysis time. The other material parameters for bentonite are listed in Table 6.1. The material parameters for rock are listed in Table 6.2.

Table 6.2 The parameter for rock and container

Material parameter	Rock	Container
E_0 (kPa)	780×10^3	4660×10^3
υ	0.47	0.47
Permeability k (m/s)	3.03×10^{-7}	5×10^{-8}

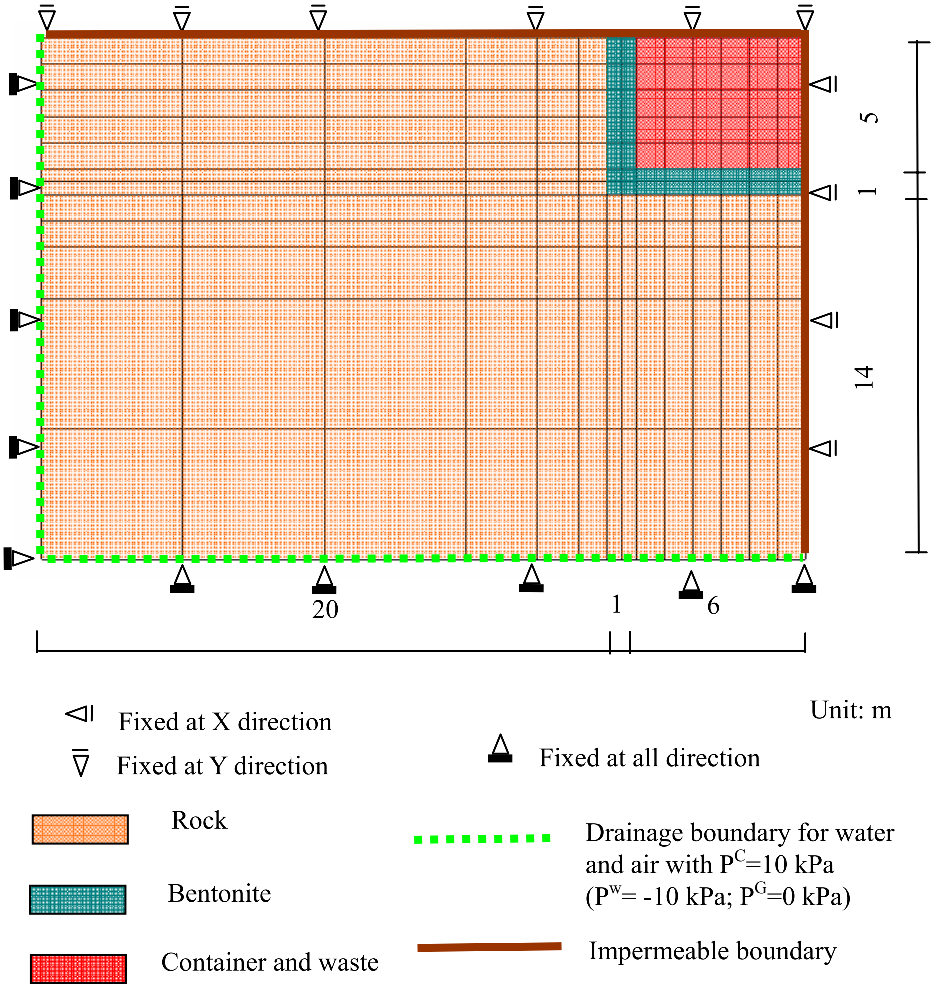
5
1
14
20
1
6
Unit: m
Fixed at X direction
Fixed at Y direction
Fixed at all direction
Rock
Bentonite
Container and waste
Drainage boundary for water and air with P^C=10 kPa (P^W= -10 kPa; P^G=0 kPa)
Impermeable boundary

Figure 6.4 Finite element mesh and boundary conditions

Fig. 6.5 shows contours of the change of degree of saturation with wetting. As shown in figure, the water flows into the rock and reaches the bentonite layer. Finally the bentonite layer is saturated. The changes of distribution of suction with time are shown in Fig. 6.6.

Fig 6.7 shows the distribution of the mean skeleton stress with wetting. It can be seen that the bentonite layer starts to swell after 1.3 days. The bentonite in the elements at the corner starts to swell firstly. Then the swelling develops to the adjacent elements. Because a higher value of permeability for bentonite is used, the whole of the bentonite layer becomes swollen after 180 days. The accumulated nodal displacement vector at the 29.8 days is shown in Fig. 6.7. Since the elastic modulus of surrounding rock is small compared with that of the container, the deformation toward the rock side is larger than deformation to inside due to the swelling of the bentonite layer. The distributions of the deformation along the bentonite layer after swollen are shown in Fig.6.9. It can be seen that the maximum of deformation appears at the outside of the center with almost 3 mm.

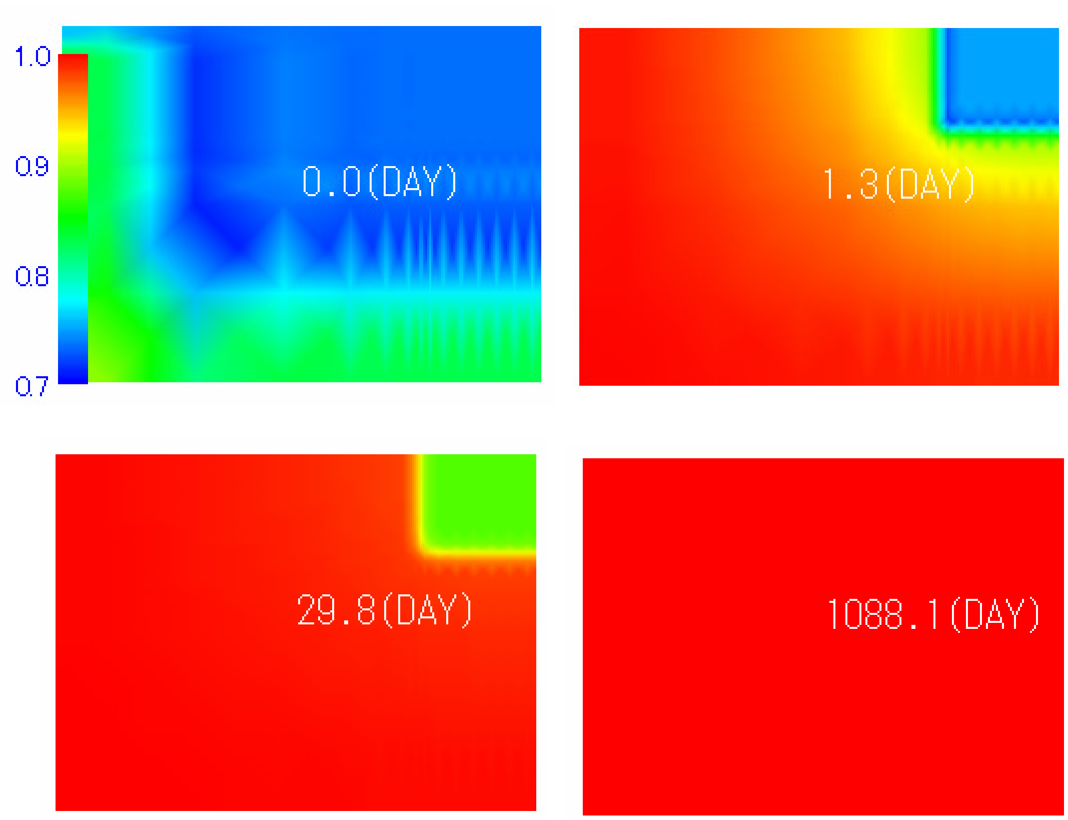

Figure 6.5 Distribution of degree of saturation

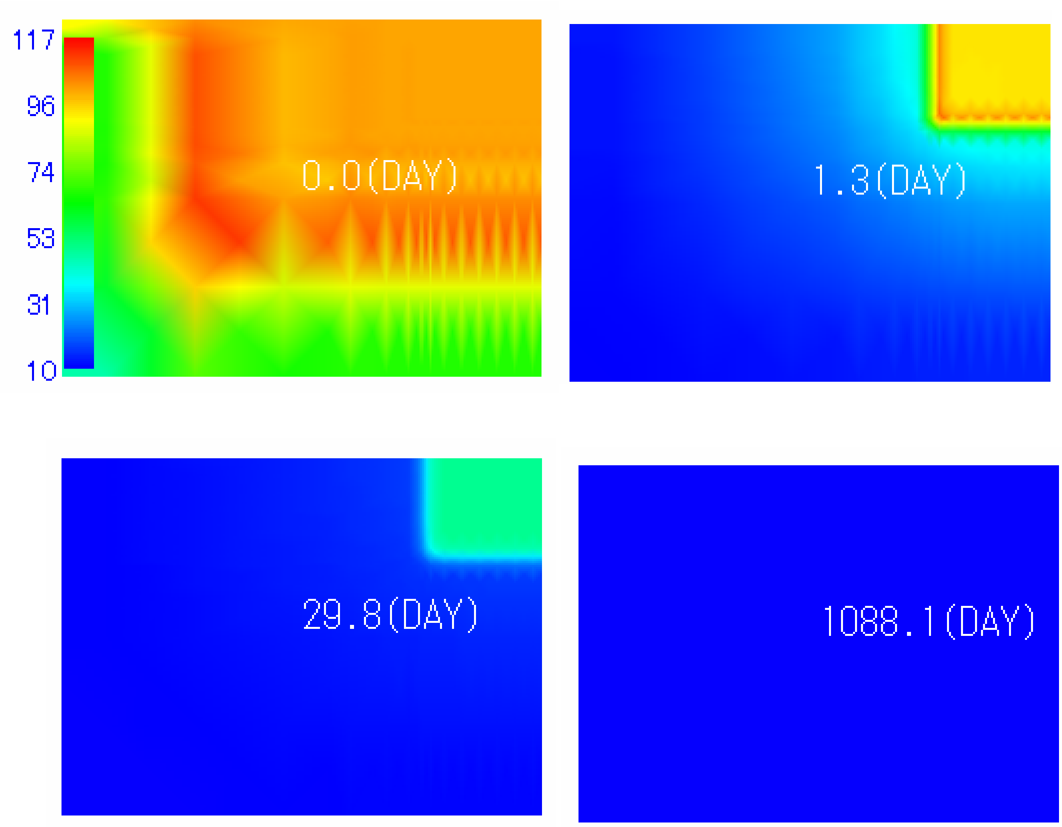

Figure 6.6 Distribution of the suction with wetting (kPa)

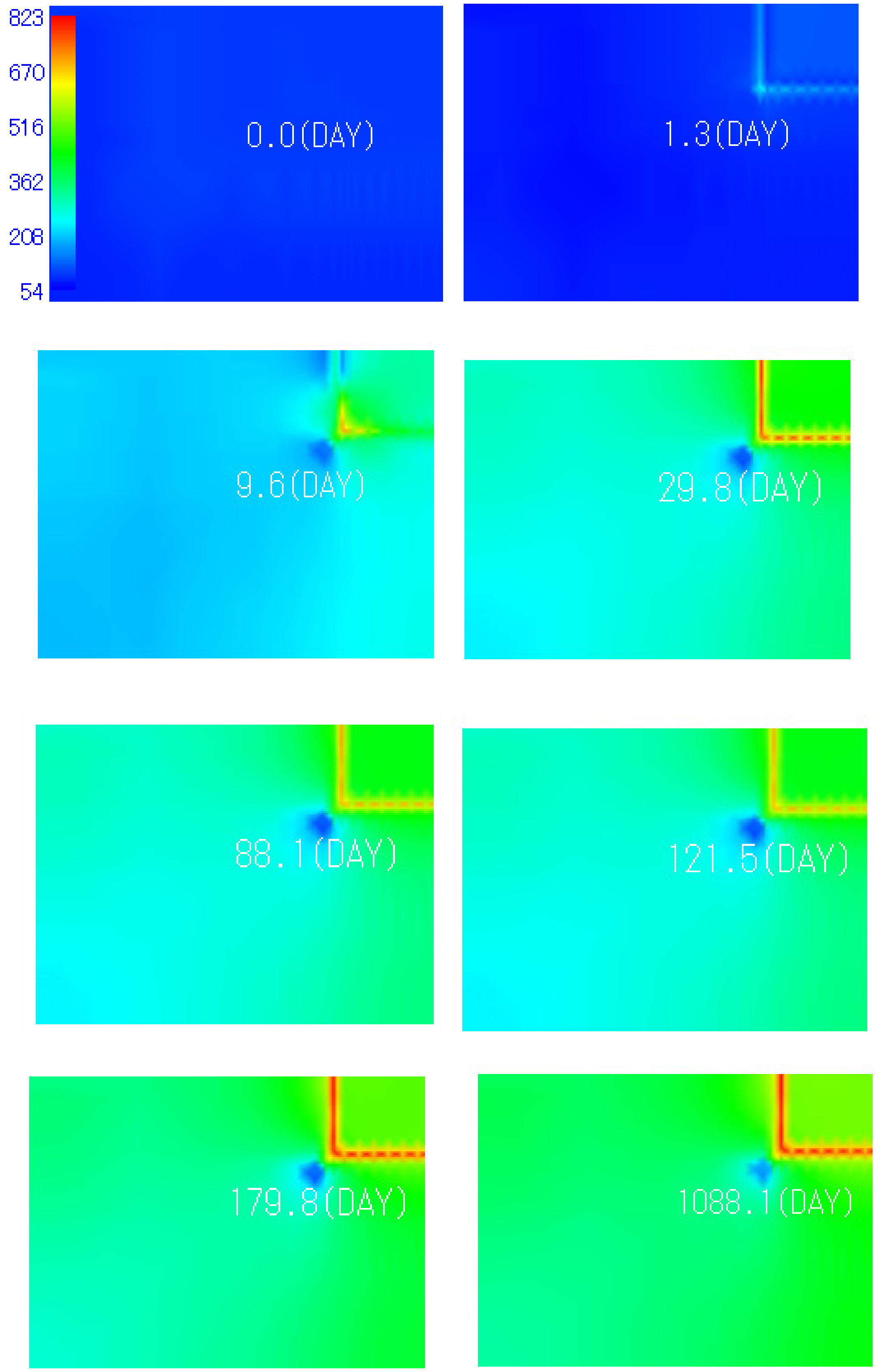

Figure 6.7 Distribution of mean skeleton stress with wetting (kPa)

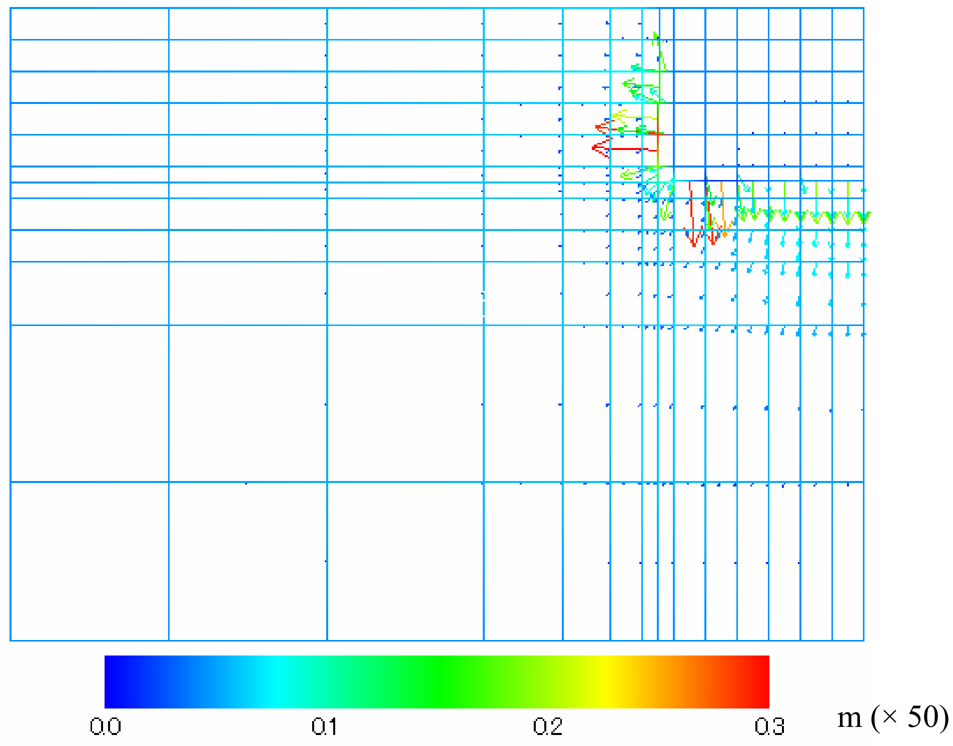

Figure 6.8 Vector of the displacements at 29.8 days

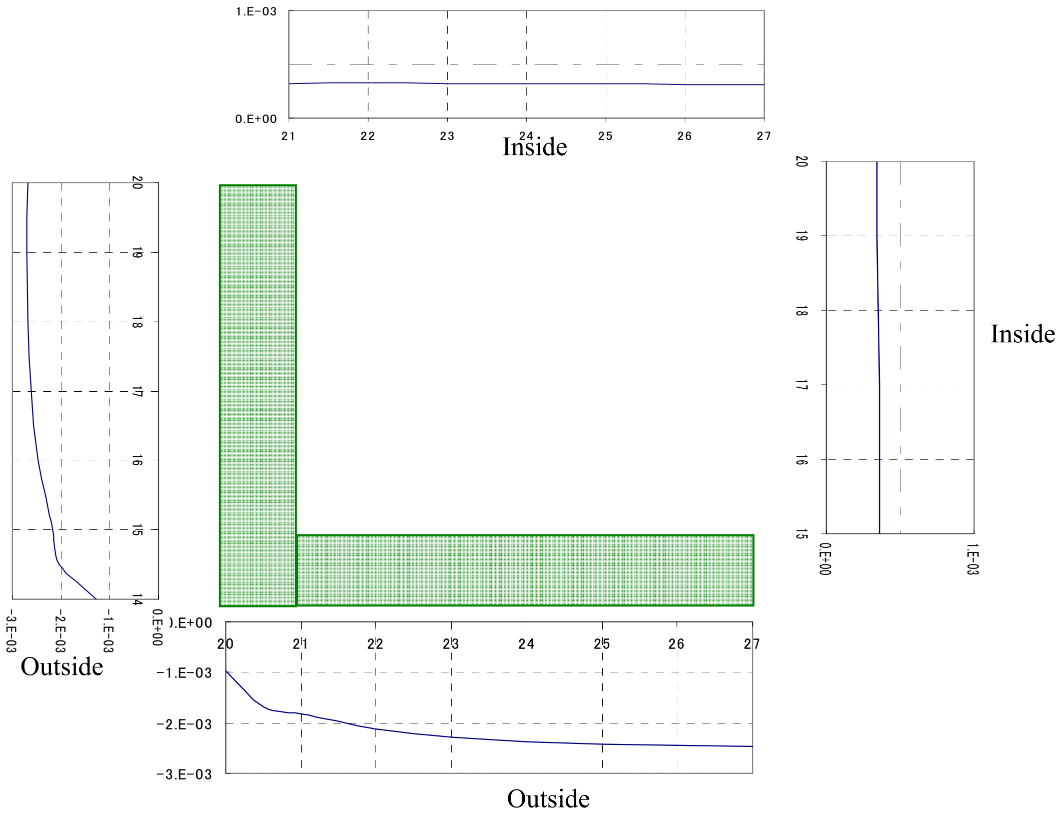

Figure 6.9 Displacement along the buffer layer (m)

6.2.3 Swelling of Bentonite Layer with Fine Element Size

In the previous section, the inside container structure is simplified by assuming to be homogeneous. In the real case, concrete lining are constructed between the buffer layer and waste container, as shown in Fig. 6.10. In addition, the coarse meshes are adopted for bentonite with thickness of 0.5m in previous analysis. In this section, the behavior of the bentonite layer and inside structure are investigated in detail, by refining the mesh with thickness of 0.2m. Fig. 6.10 shows the finite element mesh and the boundary conditions used in the analysis. The concrete lining and waste container are assumed as elastic material, and the material parameters are listed in Table 6.3. The material parameters for bentonite are listed in Table 6.1. The permeability of bentonite (Kunigel V1) is affected by the dry density of bentonite. According to the experimental relationship between the dry density and permeability, the permeability of bentonite is set to be 2×10^{-13}m/s, as shown in Table 6.1. However, a long calculating time is needed to reach the full saturation of buffer layer, using the permeability of 2×10^{-13}m/s. To save the calculation time, a calculation is also carried out using permeability of 2×10^{-11}m/s.

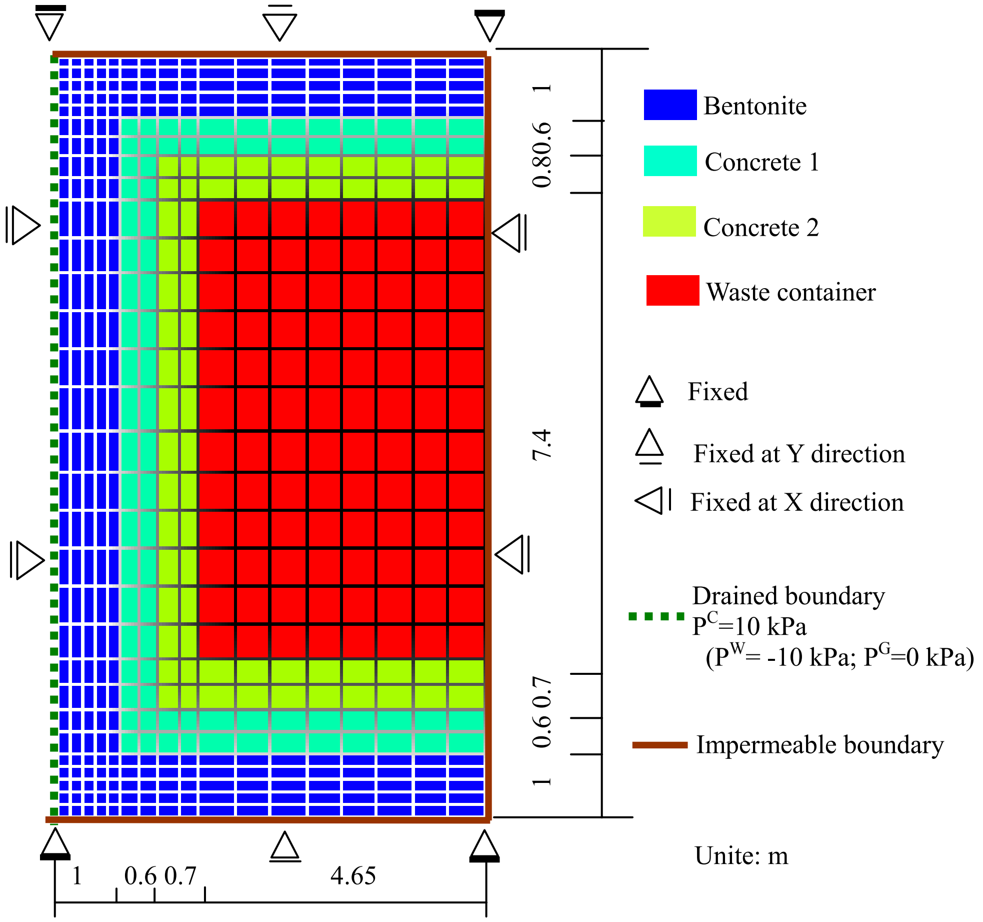
Bentonite
Concrete 1
Concrete 2
Waste container
Fixed
Fixed at Y direction
Fixed at X direction
Drained boundary
P^C=10 kPa
(P^W= -10 kPa; P^G=0 kPa)
Impermeable boundary
Unite: m
1
0.6
0.7
4.65
1
0.8
0.6
7.4
0.6
0.7
1

Figure 6.10 Finite mesh and boundary conditions

Table 6.3 Parameters for the elastic materials

Material parameters	Waste container	Concrete 1	Concrete 2
E_0 (MPa)	88000	46600	46600
ν	0.2	0.2	0.2
Permeability k (m/s)	1.03×10^{-8}	1.03×10^{-9}	1.03×10^{-8}

6.2.3.1 Simulation with a higher permeability

Fig. 6.11 shows the distribution of degree of saturation with wetting process in the case of permeability of 2×10^{-11}m/s. The bentonite layer close to the drained boundary become saturated from outside to inside gradually. After almost 6 months, the left side of bentonite layer becomes saturated. Fig 6.12 shows the distribution of the mean skeleton stress. The swelling process can be clearly simulated. Swelling starts from the outside of the left part to inside. This process needs almost 46 days. After that, the top and bottom parts of bentonite layer starts to swelling. It can be observed that in the top and bottom layers, the swelling develops from the left to right, however, this process is not uniform. It develops faster near the concrete boundary, as shown in the Fig. 6.12.

Fig. 6.13 shows the distribution of the accumulated displacement vectors from the beginning to the end of analysis.

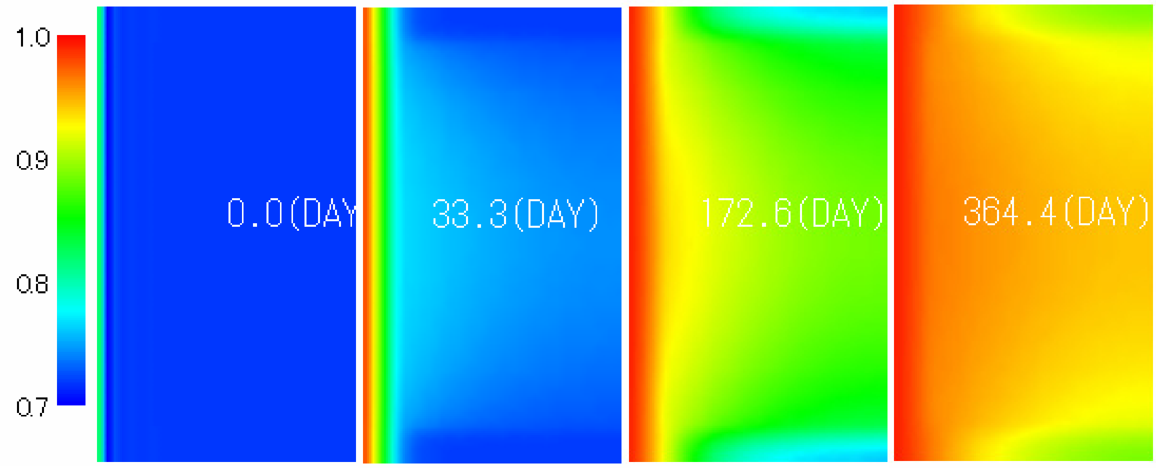

Figure 6.11 Distribution of the degree of saturation (%)

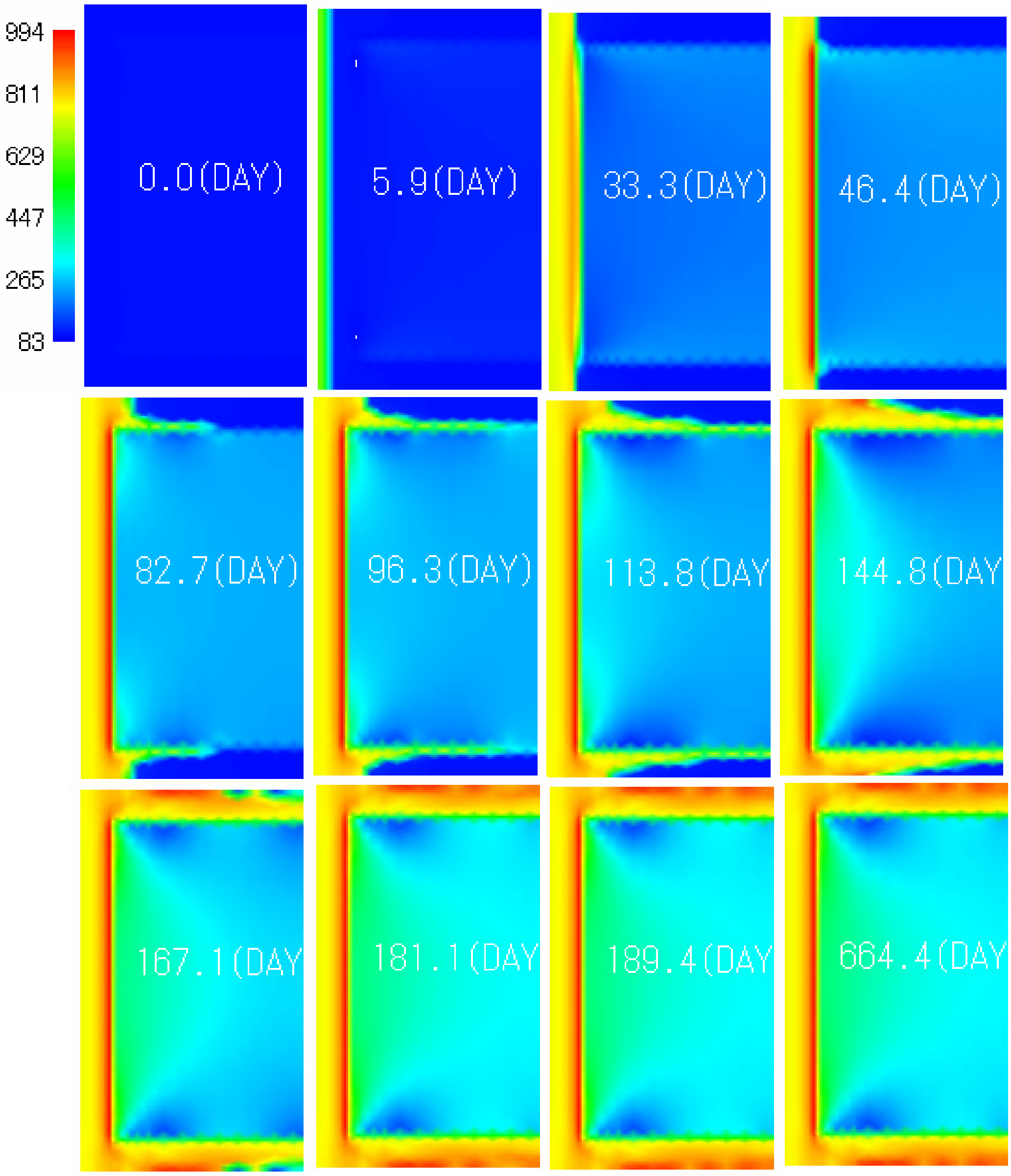

Figure 6.12 Distribution of the mean skeleton stress (kPa)

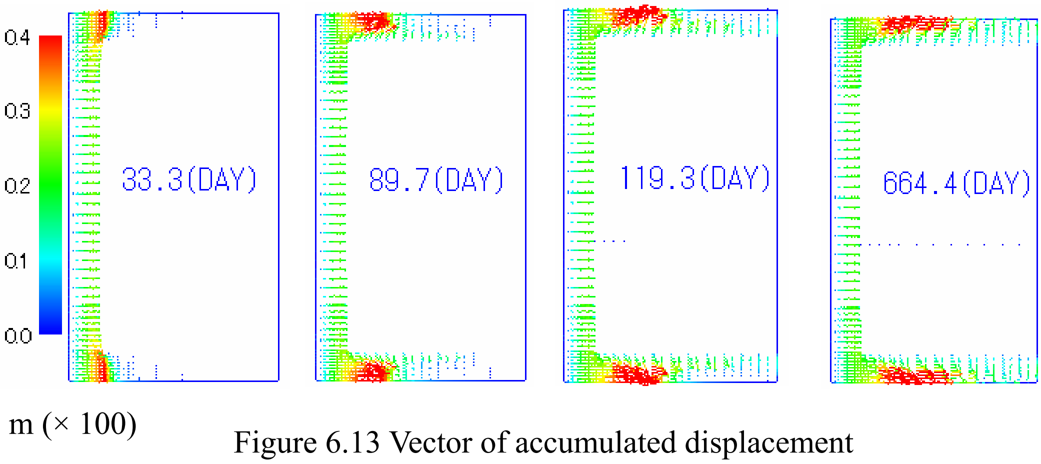

Figure 6.13 Vector of accumulated displacement

6.2.3.2 Simulation with a lower permeability

The simulation is carried out in the case permeability of 2×10^{-13}m/s. Fig. 6.14 shows the distribution of degree of saturation with wetting process. It can be seen that the wetting process need a long time. Fig 6.15 shows the distribution of the mean skeleton stress. After more than 120 years, swelling only happened in the small part of bentonite layer within the depth of 0.6m, as shown in Fig 6.15. The calculation is still going on to investigate the long-time behavior. The time increment are shown in Figure 6.16.

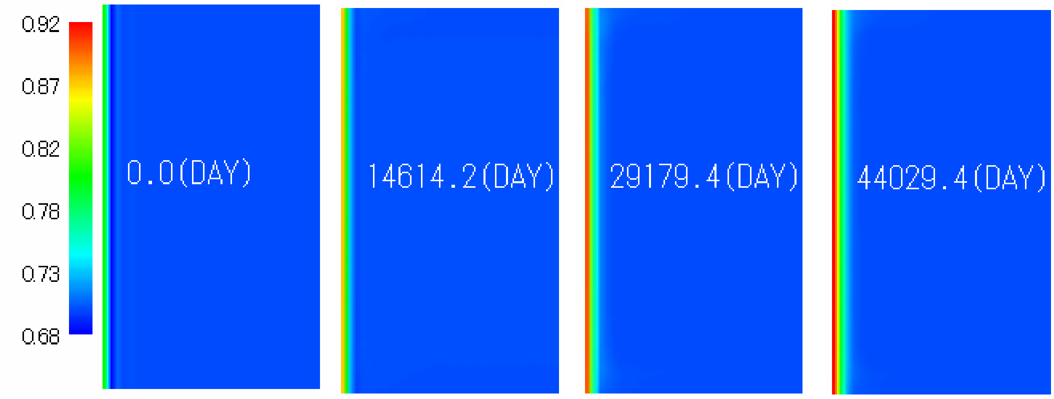

Figure 6.14 Distribution of degree of saturation (%)

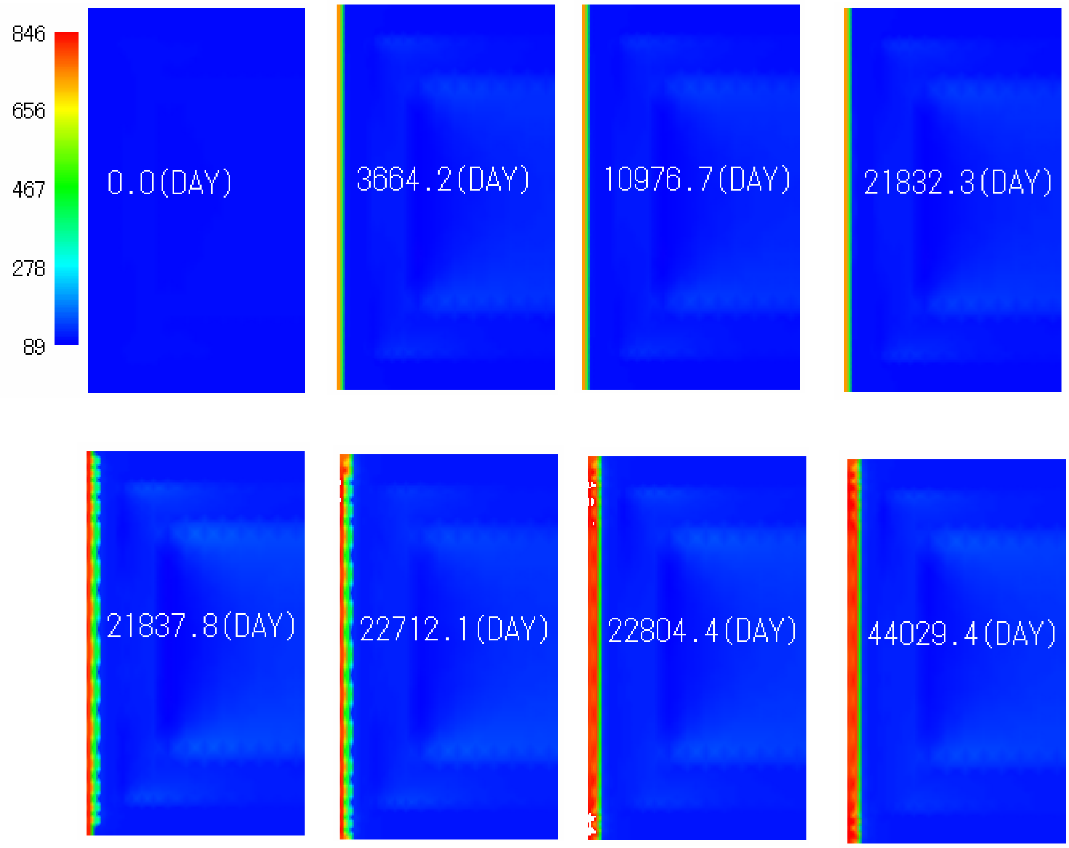

Figure 6.15 Distribution of the mean skeleton stress (kPa)

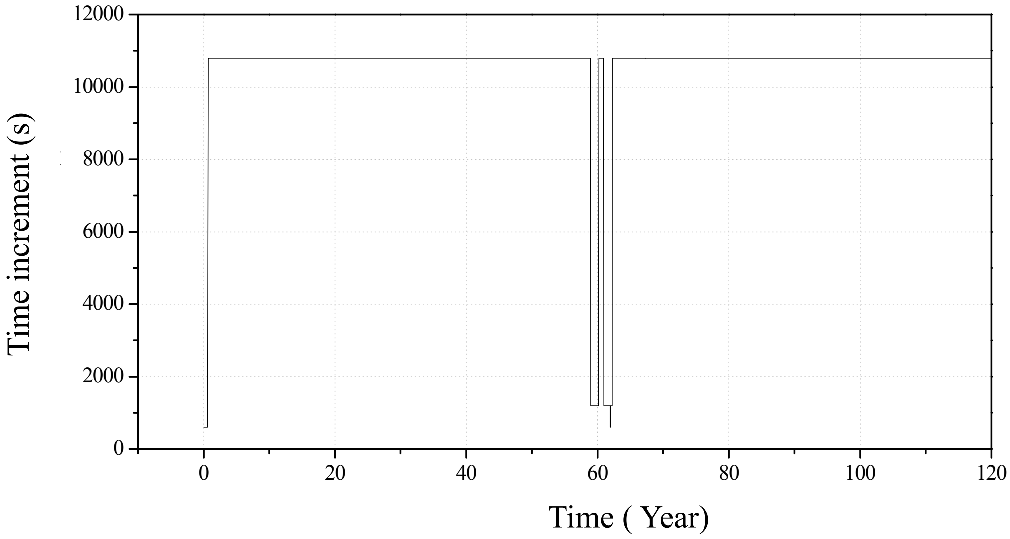

Figure 6.16 Time increment employed in analysis

6.2.4 Application to a Large Scale Problem

In this section, a full two-dimensional analysis of bentonite based engineered barriers (Horikoshi et al. 2007) incorporating all of the primary features of the tunnel is developed. Fig. 6.17 shows the finite element mesh and the boundary conditions used in the analysis. In particular, the model domain has a height of 54.27 m and width of 29.55 m as shown in Fig. 6.17. This model has been discretised using 8-node quadrilateral elements and consists of 1153 elements and 3530 nodes. The mesh has been refined in and around the bentonite layer, and a coarser mesh discretisation is used in the far-field rock. Size of the model has been reduced by 50% via the introduction of a vertical symmetry line along the centre of the tunnel. In the analysis, water pressure is assumed to be applied at the bottom; meanwhile, other boundaries are set to be impermeable. The boundary conditions include a roller which allows only vertical movement along the right-hand side boundary, the other three boundaries are fixed.

This model in total includes 6 kinds of materials, which are surrounding rock, EDZ (Excavation Disturbed Zone), backfill concrete, bentonite, concrete, and waste. In this analysis, only the bentonite is assumed to follow the swelling elasto-viscoplastic constitutive model, which is mentioned in Chapter 5, the other materials are assumed to be elastic material. All the materials are assumed to be initially unsaturated. The multiphase simulation is carried out using the formulations mentioned in Chapter 2. The material parameters for bentonite are listed in Table 6.1. The permeability of bentonite layer is adopted as 2×10^{-11}m/s, and the other parameters for other materials are listed in Table 6.4. It can be seen that the permeability used in this analysis are a larger than the measured case to save the calculation time. Furthermore, the calculation still need a long time. We stop the calculation after the bentonite in corner elements started to swelling.

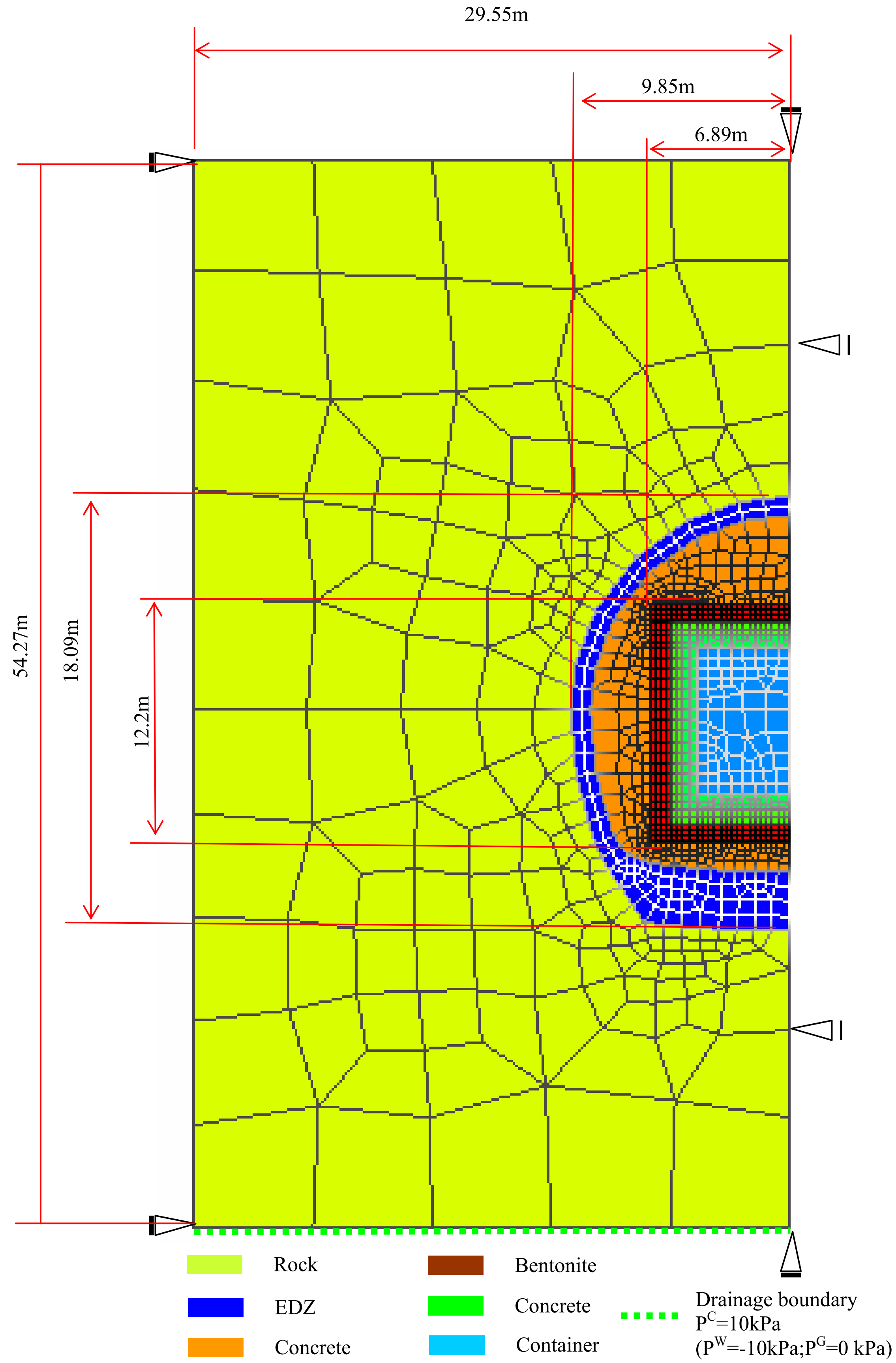
29.55m
9.85m
6.89m
54.27m
18.09m
12.2m
Rock
EDZ
Concrete
Bentonite
Concrete
Container
Drainage boundary
P^C=10kPa
(P^W=-10kPa;P^G=0 kPa)

Figure 6.17 Finite element mesh and the boundary conditions for the problem (Horikoshi et al. 2007)

Table 6.4 The material parameters for elastic materials

Material	Rock	EDZ	Backfill concrete	Concrete	Waste container
E_0 (kPa)	780×10^3	78×10^3	4660×10^3	88×10^6	88×10^6
ν	0.47	0.49	0.2	0.2	0.2
k (m/s)	1.03×10^{-6}	1.0×10^{-6}	1.03×10^{-6}	1.03×10^{-6}	1.03×10^{-8}

Figure 6.18 shows the distribution of the pore water pressure with wetting. the wetting process starts from the bottom, then the surrounding rock is saturated. Due to the higher permeability is adopted in this analysis, the bentonite layer starts to swell after 1.6 days.

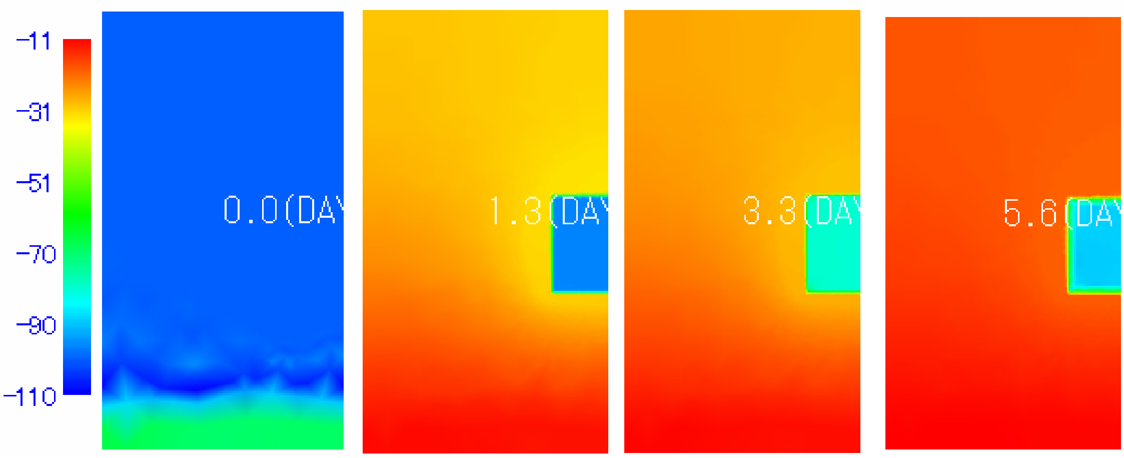

Figure 6.18 Distribution of pore water pressure with wetting (kPa)

The distribution of mean skeleton stress with wetting is shown in Figure 6.19. It can be seen that the swelling appears significantly around two corners. Figure 6.20 presents the distribution of mean skeleton stress at two corners. Fig. 6.21 shows the distribution of second invariant of deviatoric stress tensor with wetting. Due to the swelling pressure, the maximum value of deviatoric stress concentrates in the parts of EDZ, that is close to the corner of bentonite layer. Fig. 6.22 shows the accumulated displacements vectors around the buffer layer after 1.6 and 3.6 days, respectively.

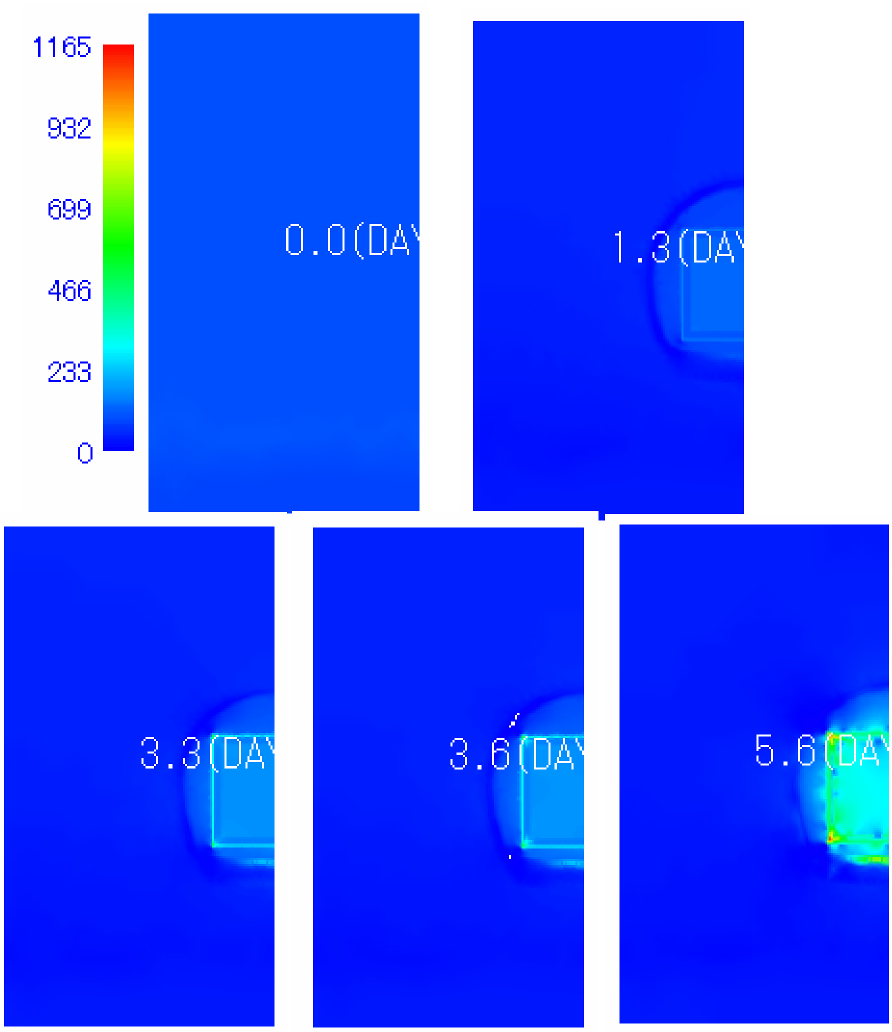

Figure 6.19 Distribution of the mean skeleton stress (kPa)

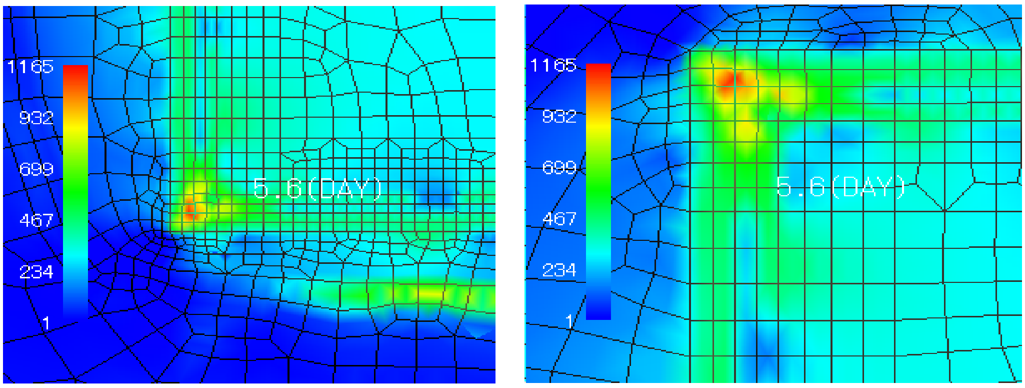

Bottom Upper

Figure 6.20 Distribution of mean skeleton stress at corner (kPa)

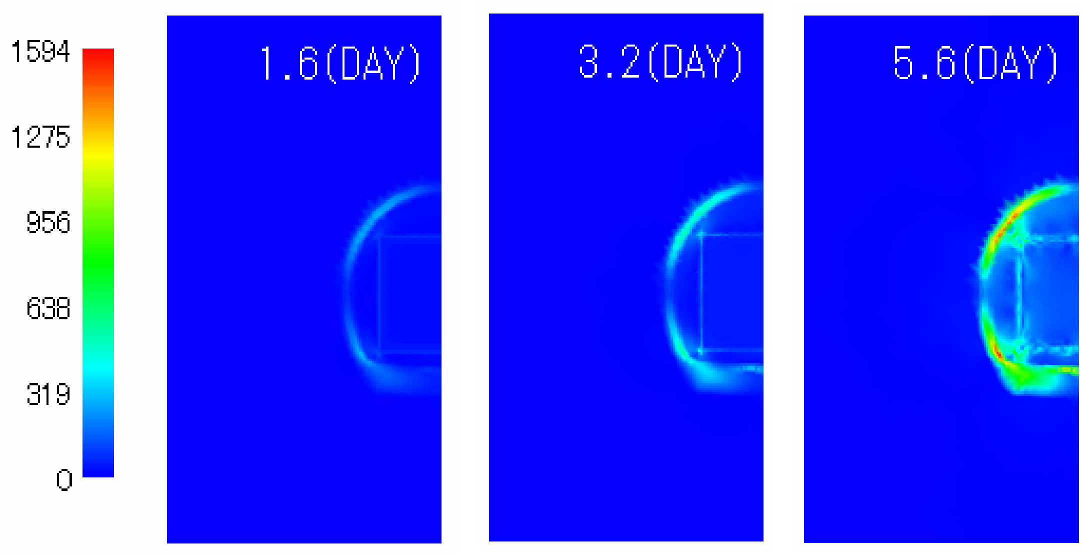

Figure 6.21 Distribution of the second invariant of deviatoric stress tensor (kPa)

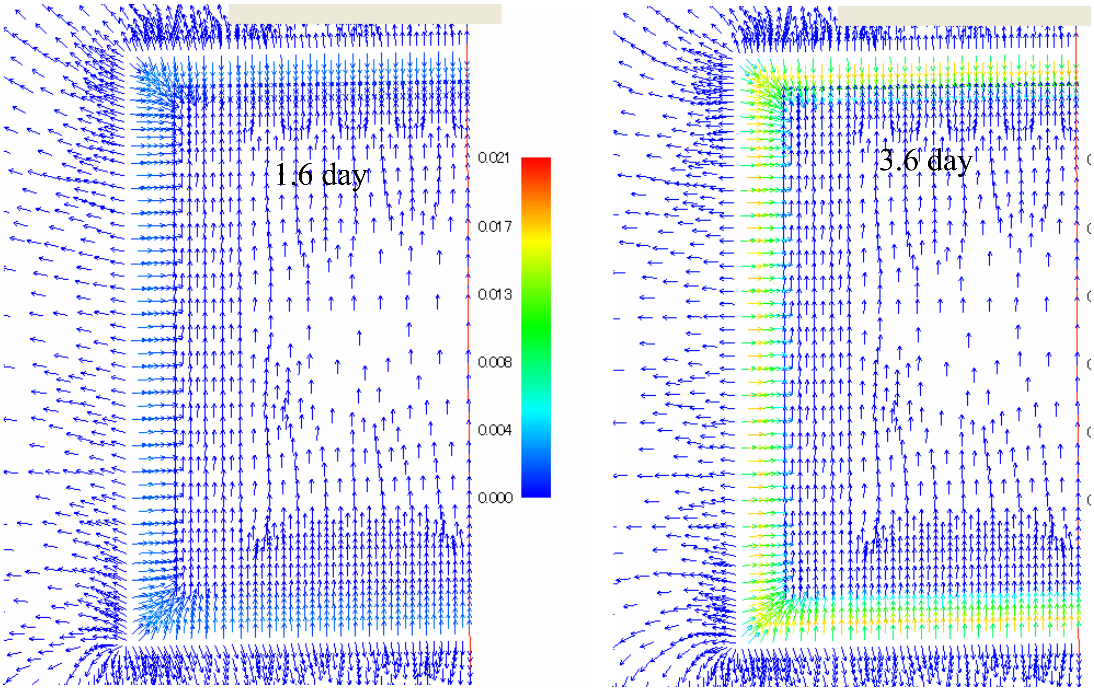

Figure 6.22 The accumulated displacement vector (around the buffer)

6.3 Summary

In this chapter, two-dimensional numerical analyses of the waste barrier projects were conducted out using the elasto-viscoplastic swelling model. The pattern of the wetting process and the development of the swelling pressure in two-dimensional condition were studied. A range of simulation results have been presented detailing the hydraulic and swelling behavior of the waste barrier. Particular attention has been given to the swelling within bentonite buffer as the material becomes saturated and swell. Simulation results show the proposed model is appropriate tool to investigate the stress distribution in surrounding rock and containers due to the seepage of groundwater.

Chapter 7

CONCLUSIONS AND FUTURE WORK

7.1 Summary and Conclusions

In the present study, the mechanics for unsaturated soil are studied. In this study based on the elasto-viscoplastic theory, three constitutive models were presented, which are elasto-viscoplastic model for normal unsaturated soil, unsaturated cyclic model, and the swelling model. In addition, from the view point of Theory of Porous Media, an air-water-soil coupled finite element method was constructed based on the nonlinear finite deformation theory.

Three-dimensional multiphase simulations under monotonic and cyclic loading were carried out. The simulation methods were verified with triaxial tests on the unsaturated silty clay. Furthermore, using the proposed swelling model, one-dimensional and two-dimensional simulations were conducted to predict the swelling pressure of bentonite. The following conclusions are drawn from this study.

In Chapter 2, the elasto-viscoplastic model for unsaturated soil was extended from the elasto-viscoplastic model for saturated soil, by adopting the skeleton stress and suction as basic stress variables. The suction effect is incorporated through the parameters of the model. The multiphase finite element method is developed using the governing equations for unsaturated soil.

In Chapter 3, three-dimensional multiphase simulations of the triaxial compression tests have been carried out, and the behaviors of unsaturated soil during triaxial compression test under drained and undrained conditions for water and air were reproduced. It can be seen that predicted results are in good agreement with the experimental results. It shows that the proposed multiphase formulation is appropriate to describe the mechanical behaviors of unsaturated soil during shearing tests, such as changes of pore-air pressure, pore-water pressure, degree of saturation and volumetric strain. Meanwhile, the proposed method can be used to predict the saturated behaivour when suction is assumed to be zero. Simulational results also show that by incorporating the suction into the constitutive model, the effect of suction on unsaturated soil can be well described. It shows that the decreace of suction leads to the increase of viscoplastic strain and the acceleration of strain localization. The proposed model can also be used to predict the effect of confining stress and strain rate on unsaturated soil.

In Chapter 4, using the unsaturated elaso-viscoplastic cyclic model, the behavior of unsaturated soil under cyclic loading with undrained conditions for water and air (constant water and constant air content) were reproduced. Comparation with experimetal results shows the proposed multiphase analysis method can be applicable to analyze the cyclic behavior of unsaturated soil, such as stress, strain, changing of pore-air pressure, pore-water pressure, degree of saturation and volumetric strain. It is shown that unsaturated sample exhibites a stiffer response and higher strength than that with low degree of suction. As the stress amplitude increase, the number of cycles needed to reach failure decrease. The prediction indictes, however, that the further parameter research is necessay from the quantitive point of view.

In Chapter 5, an evolutional equation for the absorption of water is incorporated into the unsaturated elasto-viscoplasitic model, and an elasto-viscoplastic model for unsaturated expansive soil has been developed. In the proposed model, the internal compaction effect caused by swelling of montmorillanite particles is expressed with expansion of boundary surface. In addition, effects of parameters on the predicted swelling pressure are investigated. The proposed model has been applied to swelling pressure tests for bentonite (Kunigel GX). Compared with experimental results, it is found that the proposed model can reproduce the dry density effect on swelling behavior and parameter γ controls the time-softening behavior of swelling pressure, which depends on initial water contents

In Chapter 6, two-dimensional numerical analyses of the waste barrier problems were carried out using the proposed elasto-viscoplastic swelling model. Simulation results show that the proposed model is appropriate to investigate the stress distribution in surrounding rock and containers due to the seepage of groundwater.

7.2 Recommendation for Future work

Topics for the future research are suggested based on the findings of the present work. The following recommendations are made for future research.

In the multiphase governing equations, the van Genuchten type of SWCC is adopted. In the analysis, we assume that the SWCC is fixed during compression. Several researchers (Ho, K. M. Y. et al. 2006; Sun, D. A. et al. 2006), however, show that the SWCC also depends on the stress states, the void ratio etc. To carry out multiphase deformation analysis, the SWCC which takes the void ratio into account should be employed in the future.

The applicability of the proposed multiphase analysis method has been confirmed by the trixial tests. The proposed method will be validated by the application to the practical problems of unsaturated soil structures, such as the slope failure due to the water table change etc.

In the analysis, cyclic behavior of unsaturated soil has been simulated under quasi-static loading conditions because of the pore pressure measurement. For the more high loading rate problem, such as earthquakes, the model needs to be verified based on the experimental results in the more wide range of loading rates.

The elasto-viscoplastic swelling model has been proposed. Two new parameters are introduced in the model, which describe the swelling potential and the internal compaction phenomena, respectively. The determination of these parameters needs to be investigated in the future.

References

Adachi, T. and Oka, F. (1982) Constitutive equations for normally consolidated clay based on elasto-viscoplasticity, *Soils and Foundations*, **22**(4), pp. 57-70.

Adachi, T. and Okano, M. (1974) A constitutive equation for normally consolidated clay, *Soils and Foundations*, **14**, pp. 55-73.

Adachi, T. and Oka, F. (1984) Constitutive equations for sands and overconsolidated clays and assigned works for sand, *Proc. Int. Workshop on Constitutive Relations for Soils*, Grennole, Gudehus, G., Darve, F. and Vardoulakis, I. eds., Balkema, pp. 141-157.

Adachi, T., Oka, F. and Mimura, M. (1984) Study on secondary compression of clays, *Proceedings of Symposium on Sedimentation Consolidation Model-Prediction and Validation,* San Francisco, ASCE, pp. 69-83.

Alonso, E. E., Gens, A. and Josas, A. (1990) A constitutive model for partially saturated soils, *Geotechnique*, **40** (3), pp.405-430.

Alonso, E.E., Gens, A., and Lloret, A. (1991) Double structure model for the prediction of long-term movements in expansive materials, *Proceedings of the 7th International Conference on Comp. Meth. and Adv. in Geomech*, Cairns, pp. 54-548.

Alonso, E.E., Lloret, A., Gens, A. and Yong, D.Q. (1995) Experimental behaviour of highly expansive double-structure clay, *Proc. 1st Int. Conference on Unsaturated Soils*, UNSAT'95, Paris, France, Alonso, E.E. and Delage, P. eds., Balekema, pp. 11-16.

Alonso, E.E., Vaunat, J. and Gens, A. (1999) Modeling the mechanical behaviour of expansive clays, *Engineering Geology*, **54**, pp. 173-183.

Alonso, E.E., Romero, E., Hoffmann, C. and Garcia-Escudero, E. (2005) Expansive bentonite-sand mixtures in cyclic controlled-suction drying and wetting, *Engineering Geology*, **81**, pp. 213-226.

Biot, M.A. (1962) Mechanics of deformation and acoustic propagation in porous media, *Journal of Applied Physics*, **33**(4), pp. 1482-1498.

Bishop, A.W. (1960) The measurement of pore pressure in triaxial test, Proc. *Conf. Pore Pressure and Suction in Soils*, Butterworths, London, pp. 38-46.

Bishop, A.W. and Donald, I.B. (1961) The experimental study of partly saturated soil in the triaxial apparatus, *Proc. 5th Int. Conference on Soil Mechanics and Foundation Engineering*, Paris, France, **1**, pp. 13-21

Bishop, A.W. and Henkel, D.J. (1962) *The Measurements of Soil Properties in the Triaxial Tests*, Edward Arnold Publisher, 2nd edition, London.

Blatz, J.A., Graham, J. (2003) Elastic-plastic modelling of unsaturated soil using results from a new triaxial test with controlled suction, *Geotechnique*, 53 (1), pp. 113-122.

Bolt, G.H. (1956) Physico-chemical analysis of the compressibility of pure clays, *Geotechnique*, **6**(2), pp. 86-93.

Bolzon, G., Schrefler, B.A. and Zienkiewicz, O.C. (1996) Elastoplastic soil constitutive laws generalized to partially saturated states, *Geotechnique*, **46** (2), pp. 279-734.

Chapman, D.L. (1913) A contribution to the theory of electrocapillarity. *Philosophical Magazine*, **25**, pp. 475–481.

Coleman, J.D. (1962) Stress/strain relations for partly saturated soil, Correspondence, *Geotechnique*, **12**(4), pp. 348-350.

Cui, Y.J. and Delage, P. (1996) Yielding and plastic behavior of an unsaturated compacted silt, *Geotechnique*, **46** (2), pp.291-311.

De Boer, R. (1998) Theory of porous media-past and present, *ZAMM Zeitschriftfur Angewandte Mathematik und Mechanik*, **78**(7), pp. 441-466 .

Dregne, I.B. (1976) *Soils in Arid Regions*, American Elsevier, New York.

Ehlers, W. (2003) Continuum and numerical simulation of porous materials in science and technology, *Modeling and Mechanics of Granular and Porous Materials*, Chapter 9, Capriz, G., Ghionna, V. N. and Giovine, P. eds., Birkhauser, pp. 245-291.

Ehlers, W., Graf, T. and Ammann, M. (2004) Deformation and localization analysis of partially saturated soil, *Compt. Methods Appl. Mech. Engrg,* **193**, pp. 2885-2910.

Feng, H., Kimoto, S., Oka, F., Kodaka, T. and Suzuki, H. (2006) Three dimensional multiphase analysis of elasto-viscoplastic unsaturated soil, *Proc. 19th KKCNN Symp. on civil Engng.*, pp. 449-452.

Fredlund, D.G. and Morgenstern、N.R.(1976) Constitutive relation for volume change in unsaturated soil, *Can. Geotech. J.* **13**, pp.261-276.

Fredlund, D.G. and Morgenstern, N.R. (1977) Stress state variables for unsaturated soils. *J. Geotech. Engng Div.* ASCE, **103**(GT5), pp. 313-321.

Fredlund, D.G. and Rohardjo, H. (1993) *Soil mechanics for unsaturated soils*, John Wiley & Sons, New York.

Gallipoli, D., Gens, A. Sharama, R. and Vaunat, J. (2003) An elasto-plastic model for unsaturated soil incorporating the effects of suction and degree of saturation on mechanical behaviour, *Geotechnique*, **53**(1), pp. 123-135.

Gens, A., Alonso, E.E. (1992) A framework for the behaviour of unsaturated expansive clays, *Canadian Geotechnical Journal*, **29,** pp.1013-1032.

Gens, A. (1995) Constitutive laws, *Modern Issue in Non-Saturated Soils*, Vienna, Austria, Gens, A., Jouanna, P. and Schrefler, B. A. eds., Springer, pp. 129-158.

Gouy, G. (1910) Electric charge on the surface of an electrolyte, *Journal of Physics*, **4** (9), pp. 457.

Higo. Y. (2003) *Instability and Strain Localization Analysis of Water-saturated Clay by Elasto-viscoplastic Constitutive Models*, Doctoral thesis, Kyoto University.

Higo, Y., Oka, F., Kodaka, T. and Kimoto, S. (2006) Three-dimensional strain localization of water-saturated clay and numerical simulation using an elasto-viscoplastic model, *Philosophical Magazine*, **86**, Nos.21-22, pp. 3205-3240.

Horikoshi, K., Imamura, S., Horie, M., Tani, T., Oka, F. and Higo, Y. (2007) Investigation of the long-term stability of low permeable bentonite at the disposal facility below generally used depth, *Proc. 62st Annual Meeting of JSCE*, Hiroshima, pp. 201-202. (in Japanese)

Houlsby, G.T. (1997) The word input to an unsaturated granular material, *Geotechnique*, **47**(1), pp. 193-161.

Jennings, J. E. B. and Burland, J. B. (1962) Limitations to the use of effective stresses in partly saturated soils, *Geotechnique*, **12**(2), pp. 125-144.

Jommi, C. (2000) Remarks on the constitutive modeling of unsaturated soils, *Experimental Evidence and Theoretical Approaches in Unsaturated Soils*, Tarantino, A. and Mancuso, C. eds., Balkema, pp.139-153.

Kanno, T. and Wakamatsu, H. (1992) Water-uptake and swelling properties of unsaturated bentonite buffer materials, *Canadian Geotechnical Journal*, 29 (6), pp.1102-1107.

Kim, Y.T. and Leroueil, S. (2001) Modeling the viscoplastic behavior of clays during the consolidation: application to Berthierville clay in both laboratory and field conditions, *Canadian Geotechnical Journal*, **38**(3), pp. 484-497.

Kim, Y.S. (2004) *Elasto-viscoplastic Modeling and Analysis for Cohesive Soil Considering Suction and Temperature Effects*, Doctoral Thesis, Kyoto University, Japan.

Kimoto, S. (2002) *Constitutive models for geomaterials considering structural changes and anisotropy*, Doctoral Thesis, Kyoto University, Japan.

Kimoto, S., Oka, F., Higo, Y. (2004) Strain localization analysis of elasto-viscoplastic soil considering structural degradation, In *Computer Methods in Applied Mechanics and Engineering*,**193**, pp.2845-2866.

Kimoto, S. and Oka, F. (2005) An elasto-viscoplastic model for clay considering destructuralization and consolidation analysis of unstable behavior, *Soils and Foundations*, **45**(2), pp. 29-42.

Kimoto, S., Oka, F., Fushita, T., Fujiwaki, M. (2007) A chemo-thermo-mechanically coupled numerical simulation of the subsurface ground deformations due to methane hydrate dissociation, *Computers and Geotechnics*, **34**, pp. 216-228.

Komine, H. and Ogata, N. (1996) Prediction for swelling characteristics of compacted bentonite, *Canadian Geotechnical Journal*, **33**, pp. 11-22.

Komine, H. and Ogata, N. (2003) New equations for swelling characteristics of bentonite-based buffer materials, *Canadian Geotechnical Journal*, **40**(2), pp. 460-475.

Komine, H. and Ogata, N. (2004) Predicting swelling characteristics of bentonites, *Journal of Geotechnical and Geoenvironmental Engineering*, **130** (8), pp.818-829.

Kogho, Y., Nakano, M. and Miyazaki, T. (1993) Theoretical aspects of constitutive modeling for unsaturated soils, *Soils and Foundations*, **33** (4), pp.49-63.

Kogho, Y., Asano, I. and Hayashida, Y. (2001) An elastoplasitc model for unsaturated soils based on cyclic plasticity, *Proc, Int. Workshop on Deformation of Earth Materials*, Sendai, Japan, Oka, F. ed., TC34 of ISSMGE, pp. 129-140.

Kurahayashi, S. (1980) *Clay and Life*, Tokai University, Kyoto. (in Japanese)

Ladd, C.C., Foott, R., Ishihara, K., Schlosser, F. and Poulos, H.G. (1977) Stress-deformation and strength characteristics, *Proceedings of 9th International Conference on Soil Mechanics and Foundation Engineering*, Tokyo, **2**, pp. 421-494.

Lade, P. and De Boer, R. (1997) The concept of effective stress of soil, concrete, and rock, *Geotechnique*, **47**(1), pp. 61-78.

Loret, B. and Khalili, N. (2000) A three phase model for unsaturated soils, *Int. J. Numerical and Analytical Methods in Geomechanics*, **24**(11), pp. 893-927.

Loret, B. and Khalili, N. (2002) An effective stress elastic-plastic model for unsaturated porous media, *Mechanics of Materials*, **34**, pp. 97-116.

Lloret, A., Villar, M.V., Sanchez, M., Gens, A., Pintado, X. and Alonso, E.E. (2003), Mechanical behaviour of heavily compacted bentonite under high suction changes. *Geotechnique*, **53**(1), pp. 27-40.

Lu, N. and Likos, W.J. (2004) *Unsaturated Soil Mechanics*, Wily John Wiley and Sons, Inc., pp. 494-526.

Marcail, D., Delage, P., and Cui, Y.J. (2002) On the high stress compression of bentonites, *Canadian Geotechnical Journal*, **39**, pp. 812-820.

Mata, C., Guimaraes, L., Ledesma, A., Gens, A. and Olivella, S. (2005), A hydro-geochemical analysis of the saturation process with salt water of a bentonite crushed granite rock mixture in an engineered nuclear barrier, *Engineering Geology*. **81**, pp. 227-245.

Matyas, E.l. and Radhakrishna, H.S. (1968) Volume change characteristics of partially saturated soils, *Geotechnique*, **18** (4), pp. 432-448.

Mesri, G. and Olson, R.E. (1971) Consolidation characteristics of montomorillonite, *Geotechnique*, **21**(4) pp. 341-352.

Mesri, G. and Godlewski, P. M. (1977) Time and stress compressibility relationships, *J. Geotechnical Engineering Division*, ASCE, **103** (GT5), pp. 447-430.

Mitchell, J.K. (1993) *Fundamentals of soil behaviour*. 2nd ed. John Wiley and Sons, New York.

Muraleetharan, K.K., and Nedunuri P.R. (1998) A boundary surface elastoplastic constitutive model for monotonic and cyclic behavior of unsaturated soils, *Proceedings (in CD ROM), 12th Engineering Mechanics Conference*, ASCE, La Jolla, CA, pp. 1331-1334.

Muraleetharan, K.K. and Wei, C. (1999) Dynamic behaviour of unsaturated porous medial: governing equations using the theory of mixtures with interfaces (TMI), *Int. J. Numer. Anal. Meth. Geomech.* **23**, pp. 1579–1608.

Mureleetharan, K.K., and Wei, C.F. (2000) A fully coupled analysis procedure for dynamic behaviour of unsaturated soils, *Advances in Unsaturated Geotechnics, Proceedings, GeoDenver 2000 Conference*, Geo-Institute, ASCE, Denver, Colordo, pp. 165-179.

Navarro, V., and Alonso, E.E. (2000) Modeling swelling soils for disposal barriers, *Computers and Geotechnics*, **27**, pp.19-43.

Oka, F. (1981) Prediction of time dependent behavior of clay, *Proceedings of 10th International Conference on Soil Mechanics and Foundation Engineering,* Stockholm, **1**, pp. 215-218.

Oka, F. (1982) Elasto-viscoplastic constitutive equation for overconsolidated clay, *Proc. 1st Int. Symposium on Numerical Models in Geomechanics*, Zurich, Dungar, R., Pande, G. N. and Studer, J. A. eds., Balkema, pp. 147-156.

Oka, F., Adachi, T., Okano, Y. (1986) Two-dimensional consolidation analysis using an elasto-viscoplastic constitutive equation, *International Journal for Numerical and Analytical Methods in Geomechanics*, **10**, pp,1-16.

Oka, F. (1988) The validity of the effective stress concept in soil mechanics, *Micromechanics of Granular Materials*, M. Satake and J.T. Jenkins eds., Elsevier Science Publishers B.V., Amsterdam, pp. 207-214.

Oka, F. (1992) A cyclic elasto-viscoplastic constitutive model for clay based on the non linear kinematic hardening rule, *Proc. 4th Int. Symposium on Numerical Model in Geomechanics*, Swansea, Pande, G.N. and Pietruszczak, S. eds., Balkema, **1**, pp. 105-114.

Oka, F. (1996) Validity and limits of the effective stress concept in geomechanics, *Mechanics of Cohesive-Frictional Materials*, **1**, pp. 219-234.

Oka, F., Yashima, A., Tateishi, A., Taguchi, Y. and Yamashita, S. (1999) A cyclic elasto-plastic constitutive model for sand considering a plastic-strain dependence of the shear modulus, *Geotechnique*, **49**(5), pp. 661-680.

Oka, F., Yashima, A., Sawada, K., Aifantis, E.C. (2000) Instability of gradient-dependent elastoviscoplastic model for clay and strain localization, *Computer Methods in Applied Mechanics and Engineering*, **183**, pp. 67-86.

Oka, F., Higo, Y., Kimoto, S. (2002) Effect of dilatancy on the strain localization of water-saturated elasto-viscoplastic soil, *International Journal of Solids and Structures*, **39**, pp. 3625-3647.

Oka, F., Kodaka, T. and Kim, Y.-S. (2004) A cyclic viscoelastic-viscoplastic constitutive model for clay and liquefaction analysis of multi-layered ground, *Int. J. Numerical and Analytical Methods in Geomechanics*, **28**, pp. 131-179.

Oka, F., Furuya, K. and Uzuoka, R. (2004) Numerical simulation of cyclic behavior of dense sand using a cyclic elasto-plastic model, *Proceedings of cyclic behavior of soils and liquefaction phenomena*, Triantafylidis, eds, Bochum, pp. 85-90.

Oka, F. (2005) Computational modeling of large deformations and the failure of geomaterials, Theme lecture, In *Proceedings of 16th International Conference on Soil Mechanics and Geotechnical Engineering*, Osaka, **1**, 47-95.

Oka, F., Kodaka, T., Kimoto, S., Kim, Y.-S. and Yamasaki, N. (2006) A multi-phase coupled FE analysis using an elasto-viscoplastic model for unsaturated soil, *Proc.*

2nd US-Japan workshop on Geomechanics, Geomechanics II, Geotechnical Special Publication, ASCE, pp.124-131.

Olson, R.E., and Mesri, G. (1970) Mechanisms controlling the compressibility of clay, *Journal of the Soil Mechanics and Foundations Division*, ASCE, **96**(SM6), pp. 1860-1878.

Ono, F., Niwase, K., Tani, T., Nakgoe, A., Chidimatsu,M.(2006), Results of permeability tests for bentonite with two-phase compaction by field compaction method, *Proc. 61st Annual Meeting of JSCE*, Kyoto, pp.323-324(in Japanese)

Perzyna, P. (1963) The constitutive equations for work-hardening and rate sensitive plastic materials, *Proceedings of Vibrational Problems,* Warsaw*,* **4**(3), pp. 281-290.

Pusch, R. (1982) Mineral-water interactions and their influence on the physical behaviour of highly compacted Na bentonite, *Can. Geotech. J.* **19**, pp. 289-299.

Roscoe, K.H. and Burland , J.B. (1968) On the generalized stress-strain behavior of 'wet' clay, *Engineering plasticity* (Cambridge University Press), eds. Heyman, J. and Leckie, F.A., pp. 535-609.

Roscoe, K.H., Schofield, A.N. and Thurairajah, A. (1963), Yielding of clays in states wetter than critical, *Geotechnique*, **13**(3), pp. 211-240.

Roscoe, K.H. and Schofield, A.N. (1963) Mechanical behavior of an idealized 'wet' clay, *Proceedings of the European Conference on Soil Mechanics and Foundation Engineering,* Wiesbaden*,* **1**, pp.47-54.

Schrefler, B. A. and Gavin, D. (1996) The effective stress principle: incremental or finite form?, *Int. J. for Numerical and Analytical Methods on Geomechanics*, **20** (11), pp. 785-814.

Sheng, D., Sloan, W., Gens, A. and Smith, D.W., (2003) Finite element formulation and algorithms for unsaturated soils Part I: Theory, *Int. J. Numer. Anal. Meth. Geomech*, **27**, pp. 745-765.

Sridharan, A., and Choudhury, D. (2002) Swelling pressure of sodium montmorillonites, *Geotechnique*, **52**(6), pp. 459–462.

Suzuki, H., Kodaka, T., Oka, F., (2006) Mechanical Properties of Unsaturated Silt under Unexhausted and pore air pressure controlled conditions. *Proc. 41st Annual Meeting of JGS*, Kagoshima, pp. 323-324. (in Japanese)

Taylor, D.W. (1948) *Fundamentals of Soil Mechanics*, Wiley, New York.

Thomas, H.R. and He, Y. (1998) Modeling the behaviour of unsaturated soil using an elastoplastic constitutive model. *Geotechnique*, **48**(5), pp. 589-603.

Tripathy, S., Sridharan, A., Schanz, T. (2004) Swelling pressures of compacted bentonites from diffuse double layer theory, *Canadian Geotechnical Journal*, **41**, pp. 437-450.

Truesdell, C. (1984) *Thermodynamics of diffusion*, Truesdell, C. eds., Rational Thermodynamics, second ed., Springer-Verlag, NewYork, pp. 219–236.

van Genuchten, M. Th. (1980) A closed-form equation for predicting the hydraulic conductivity of unsaturated soils, *Soil Sci. Soc. Am. J.*, **44**, pp. 892-899.

Wang, T.T., Fredlund, D.G., and Krahn, J. (1998) A numerical study of coupled consolidation in unsaturated soils, *Canadian Geotechnical Journal*, **35**, pp. 926-937.

Watanabe, T., Oka, F., Kimoto, S., Higo, Y., and Yabuki, T. (2007) Simulation of cyclic triaxial tests of unsaturated silt by elasto-viscoplastic model, *Proc. 62st Annual Meeting of JSCE*, Hiroshima, pp. 211-212. (in Japanese)

Wheeler, S. J. (1996) Inclusion of specific water volume within an elasto-plastic model for unsaturated soil, *Canadian Geotechnical Journal*, **33**, pp. 42-57.

Wheeler, S. J. and Karube, D. (1996) State of the art report-constitutive modeling, *Proc. 1st Int. Conference on Unsaturated Soils*, Paris, **3**, pp. 1323-1356.

Wheeler, S. J. and Sivakumar, V. (1995) An elasto-plastic critical state framework for unsaturated soil, *Geotechnique*, **45**(1), pp. 1323-1356.

Wulfsohn, D., Adams, B. A. and Fredlund, D.G. (1998) Triaxial testing of unsaturated agricultural soils, *J. agric. Engng Res.*, **69**, pp. 317-330.

Yabuki, T., Oka, F., Kimoto, S., Higo, Y., and Watanabe, T. (2007) Mechanical behavior of unsaturated silt under cyclic loading, *Proc. 42st Annual Meeting of JGS*, Nagoya, pp. 771-772. (in Japanese)

Yamamura, K. (1971) *Soil Engineering Research of River Embankment*. Doctoral Thesis, Kyoto University, Japan. (in Japanese)

Yin, J.-H. and Graham, J. (1989) Viscous-elastic-plastic modeling of one-dimensional time-dependent behavior of clays. *Canadian Geotechnical Journal*, **26**, pp. 199-209.

Yong, R.N. (1999) Overview of modeling of clay microstructure and interactions for prediction of waste isolation barrier performance. *Engineering Geology*. **54**, pp. 83-91.

Yong, R.N. (1999) Soil suction and soil-water potentials in swelling clays in engineered clay barriers. *Engineering Geology*. **54**, pp. 3-13.